UC Davis
UC Davis Electronic Theses and Dissertations

Title
SIMULATION, FABRICATION, AND TESTING OF EPITAXIAL GERMANIUM X-RAY PHOTODIODES

Permalink
https://escholarship.org/uc/item/7gm1520q

Author
Mistyuk, Sergei

Publication Date
2024

Peer reviewed|Thesis/dissertation

eScholarship.org Powered by the California Digital Library
University of California

Simulation, Fabrication, and Testing of Epitaxial Germanium X-ray Photodiodes

By

SERGEI MISTYUK

DISSERTATION

Submitted in partial satisfaction of the requirements for the degree of

DOCTOR OF PHILOSOPHY

in

Electrical and Computer Engineering

in the

OFFICE OF GRADUATE STUDIES

of the

UNIVERSITY OF CALIFORNIA

DAVIS

Approved:

Charles E. Hunt, Chair

Erkin Şeker

Diego R. Yankelevich

Committee in Charge

2024

Table of Contents

Abstract v

List of Figures vi

List of Tables x

Acknowledgements xi

Chapter 1 – Introduction 1

1.1. Motivation 1

1.2. Radiographic Imaging and NIF Imaging Requirements 3

1.3. Imaging Array High Level Specifications 5

1.4. Dissertation Overview 6

Chapter 2 – X-Ray Photodiodes 8

2.1. Electromagnetic Radiation and its Interaction with Matter 8

2.2. Germanium Material Properties 11

2.2.1. Energy Bands and the Fermi Function 11

2.2.2. Electrically Active Impurities 14

2.2.3. Carrier Transport Phenomena 16

2.2.4. Generation, Recombination, and Carrier Lifetimes 18

2.2.5. Material Responsivity and Photocurrent 26

2.2.6. Internal and External Quantum Efficiency 28

2.3. Semiconductor Photodiodes 28

2.3.1. The PN Junction and Ideal Diode Equation 28

2.3.2. The Depletion Region, Impact Ionization, and Reverse Breakdown 30

2.3.3. Photocurrent in a Diode 32

2.3.4. Common Photodiode Architectures 33

2.3.5. A Brief Justification of Germanium 36

2.4.3. Competing X-Ray Detection Technologies 41

Chapter 3 – Device Simulation and Design 43

3.1. Silvaco Model Setup 43

3.1.1. Mobility 43

3.1.2. Saturation Velocity 45

3.1.3. Electrically Active Impurities 46

3.1.4. Generation-Recombination 47

3.1.5. Tunneling Effects 47

3.1.6. Generation-Recombination – The Complete Model 49
3.1.7. Defect Analysis 49
3.1.8. Metal Contact Properties 49
3.2. Comparison between Simulated and Fabricated Devices 50
3.3. Wafer Development Simulations 50
3.3.1. Internal Electric Field Simulations 52
3.3.2. Epitaxial Process Simulation 53
3.3.3. Heterojunctions 54
3.4. Device Simulations 56
3.4.1. Planar Photodiode 57
3.4.2. Superjunction Photodiode 60
3.4.3. Pitted Anode Devices 61
3.4.4. Hybrid Structures 69
3.5. Conclusions 72
Chapter 4 – Fabrication Challenges 74
4.1. Surface Passivation 74
4.1.1. Experimental Procedure 76
4.1.2. Results 77
4.2. Cathode Ohmic Contact Formation 80
4.2.1. Experimental Procedure 82
4.2.2. Results 84
4.3. Metallization Adhesion and Stability over Time 85
4.4. Backside Etch 87
4.5. Post-Dicing and Packaging Voltage-Current Characteristics 88
Chapter 5 – Optoelectronic Measurements 90
5.1. X-Ray Quantum Efficiency Measurements 90
5.1.1. Methodology 90
5.1.2. Experimental Setup 93
5.1.3. Manson X-Ray Source 100
5.1.4. Results 107
5.2. Temporal Measurements 108
5.2.1. Methodology 108
5.2.2. Experimental Setup 111
5.2.3. Results 112
Chapter 6 – Conclusions 113

6.1. Summary and Significance of Work 113
6.2. Future Work 118
References 120

Abstract

A novel method was used to epitaxially grow P-i-N germanium photodiode structures for next-generation imaging at the National Ignition Facility (NIF) at the Lawrence Livermore National Laboratory (LLNL). Semiconductor device simulations in Silvaco Atlas were used to find the minimum impurity concentration within the intrinsic region. Following this the photodiode structure was optimized to minimize the depletion bias without sacrificing temporal performance. The epitaxial wafers meanwhile were used to fabricate photodiodes of various intrinsic thicknesses to test the mass-attenuation coefficients of epitaxial germanium to ensure the external quantum efficiency of the fabricated devices matches those predicted by the mass-attenuation coefficients of germanium as measured by the National Institute of Standards and Technology (NIST) organization. Tests were performed at the Manson laboratory at LLNL from 1keV to 8keV energy x-rays, and at the Advanced Light Source (ALS) at the Lawrence Berkeley National Laboratory (LBNL) from 6keV to 28keV energy x-rays. Following this, temporal response tests were performed by evacuating 60ps x-rays from germanium photodiodes at the ALS. Quantum efficiency was found to match those predicted by NIST. Evacuation times were found to be under two nanoseconds of both fabricated germanium photodiodes and reference silicon photodiodes, predicting excellent evacuation time.

List of Figures

Figure 1.1: NIF Process Overview ... 1
Figure 1.2: MIRANDA Code Simulation ... 2
Figure 1.3: NIF Imaging Requirements ... 3
Figure 1.4: NIF Imaging Experimental Setup ... 4
Figure 2.1: Germanium Mass-Attenuation Coefficients ... 10
Figure 2.2: Elemental Mass-Attenuation Coefficients at 30keV ... 10
Figure 2.3: Band Structure of Silicon, Germanium, and Gallium Arsenide ... 11
Figure 2.4: Fermi Function of Germanium ... 13
Figure 2.5: Fermi Energy of Various Media ... 13
Figure 2.6: Impurity Ionization Energy in Germanium ... 14
Figure 2.7: Carrier Mobility vs Temperature in Germanium ... 16
Figure 2.8: Carrier Drift Velocity vs Temperature in Germanium ... 17
Figure 2.9: Minority Carrier Lifetime Measurement in Germanium ... 20
Figure 2.10: Carrier Recombination Mechanisms in Semiconductors ... 21
Figure 2.11: Crystal Defect Types ... 22
Figure 2.12: PN Diode Structure ... 28
Figure 2.13: Current-Voltage Characteristics of Diodes ... 29
Figure 2.14: Depletion Region in Diode ... 29
Figure 2.15: Impact Ionization Rate vs Electric Field Strength of Various Semiconductors ... 31
Figure 2.16: Photocurrent in a Diode ... 33
Figure 2.17: Diode Depletion Region, Electric Field, Potential, and Photogeneration Rate ... 33
Figure 2.18: Common Photodiode Architectures ... 35
Figure 2.19: Common Schottky Diode Architectures ... 35
Figure 2.20: GaAs Photodiode ... 38
Figure 2.21: 40µm Thick GaAs Internal Quantum Efficiency ... 38
Figure 2.22: Direct and Indirect Band Gap Structures ... 38
Figure 2.23: CdTe Schottky Diode Structure ... 38
Figure 2.24: Scintillator-Diode Bonded Structure ... 41
Figure 3.1: Mobility vs Impurity Concentration Modeling and Data ... 45
Figure 3.2: Carrier Velocity vs Electric Field Strength Modeling and Data ... 45
Figure 3.3: Impurity Ionization Energy in Germanium ... 46
Figure 3.4: A Complete Leakage Current Model in Germanium ... 49
Figure 3.5: Fabricated Germanium Devices for Modeling Comparison ... 49

Figure 3.6: Real vs Simulated Germanium Current Voltage Characteristic 51
Figure 3.7: Impurity Cocentration in First Generation Epitxial Germanium Wafers 52
Figure 3.8: Diode Depletion Depth vs Intrinsic Impurity Concentration 52
Figure 3.9: Impurity Concentration in Third Generation Epitaxial Germanium Wafers 52
Figure 3.10: Simualted Epitaxial Wafer Growth 53
Figure 3.11: Types of Heterojunctions 55
Figure 3.12: Epitaxial Heterojunction Growth Results 55
Figure 3.13: Simulated Current-Voltage Characteristics of Heterojunctions 55
Figure 3.14: Photodiode Structures Simulated 57
Figure 3.15: Simulated PiN Photodiode Structure 58
Figure 3.16: Predicted PiN Photodiode Electric Field 58
Figure 3.17: Predicted PiN Photodiode Carrier Concentrations 58
Figure 3.18: X-Ray Simulation Setup 59
Figure 3.19: Predicted PiN Photodiode X-Ray Pulse Resposne 59
Figure 3.21: Two Types of Superjunction Structures 61
Figure 3.22: Doping Structure of 12-Layer GPSJ 62
Figure 3.23: Predicted Depletion Bais of Superjunction Devices 62
Figure 3.24: Predicted Internal Electric Field of GPSJ Structures 63
Figure 3.25: Predicted Carrier Concentration in 6-Layer GPSJ Structure 63
Figure 3.26: Predicted X-Ray Pulse Response 64
Figure 3.27: Predicted Impact Generation Rates 65
Figure 3.28: Predicted Impact Generation Rate Modulation 65
Figure 3.29: Deep Pit Structure 66
Figure 3.30: Simulated Deep Pit Structure 66
Figure 3.31: Predicted Deep Pit Structure Internal Electric Field 66
Figure 3.32: Predicted X-Ray Pulse Response 67
Figure 3.33: Predicted X-Ray Pulse Response Comparison 67
Figure 3.34: Predicted Deep Pit Impact Generation Rate 67
Figure 3.35: Scintillating Deep Pit Structure 68
Figure 3.36: Ideal Quantum Efficiency of Deep Pit Structure 68
Figure 3.37: Hybrid Structure Doping Profile 71
Figure 3.38: Predicted Hybrid Structure Internal Electric Field 70
Figure 3.39: Predicted Hybrid Structure X-Ray Pulse Response 71
Figure 3.40: Predicted Hybrid Structure Impact Ionization Rate 71
Figure 3.41: Predicted Hybrid Structure Electric Field vs Bias 72

Figure 3.42: Comparison of Predicted X-Ray Pulse Responses 72
Figure 4.1: Unpassivated Germanium Surface 75
Figure 4.2: Types of Passivation 75
Figure 4.3: Unsuccesful Passivation Techniques 78
Figure 4.4: Successful Passivation Techniques 79
Figure 4.5: Types of Contacts 81
Figure 4.6: Fermi Pinning in Germanium Measurement 81
Figure 4.7: Fermi De-Pinning Structure 57
Figure 4.8: XPS Results for De-Pinning Experiment 82
Figure 4.9: Metal Delamination 85
Figure 4.10: Anode Metalization Structure 85
Figure 4.11: Cathode Metalization 86
Figure 4.12: SMA Packaing Prodecure 86
Figure 4.13: Surface Scratching after CMP 87
Figure 4.14: Types of Cracks 88
Figure 4.15: Current Voltage Characterisitcs Post Dicing and Bonding 88
Figure 5.1: Mass-Attenuation Coefficients of Germanium 92
Figure 5.2: Medium and Large Diode Photographs 93
Figure 5.3: Device Mask and Diced Chip 93
Figure 5.4: ALS Laboratory Layout 94
Figure 5.5: Beamline Insertion Device Diagram 95
Figure 5.6: Beamline Brightness 95
Figure 5.7: Beamline 12.2.1 Monochromator 97
Figure 5.8: Beamline 12.2.1 X-Ray Beam 99
Figure 5.9: ALS Experimental Setup Block Diagram 100
Figure 5.10: ALS Experimental Setup Photograph 100
Figure 5.11: Sample External Quantum Efficiency Data 100
Figure 5.12: Manson Source Schematic 101
Figure 5.13: Characteristic X-Ray Diagram 101
Figure 5.14: Solid Angle Demonstration 103
Figure 5.15: Experimental Enclousre for Manson Lab 103
Figure 5.16: Photodiode Mount for Manson Lab 103
Figure 5.17: Manson Experimental Setup Block Diagram 105
Figure 5.18: Manson Experimental Setup Photographs 107
Figure 5.19: ALS External Quantum Efficiency Results 106

Figure 5.20: Manson External Quantum Efficiency Results 108
Figure 5.21: ALS Temporal Experimental Setup Block Diagram 109
Figure 5.22: ALS Sample Temporal Data 110
Figure 5.23: ALS Averaged Temporal Data 111
Figure 6.1: Comparison of IV Curves of Real and Simulated Devices 111
Figure 6.2: Increased Capacitance of Multi-Layered Devices 113
Figure 6.3: X-Ray Pulse Response of Various Diode Designss 114
Figure 6.4: Simulated Diode Current of Various Heterojunction Structures 115
Figure 6.5: XPS Data of Sulfur Terminated Germanium 116
Figure 6.6: ALS Quantum Efficiency Data 117
Figure 6.7: ALS Averaged Pulses 118
Figure 6.8: Full Array Mask 119
Figure 6.9: hCMOS Camera Test Setup 119

List of Tables

Table 2.1: Optical Properties of Silicon, Germanium, and Gallium Arsenide.......... 26
Table 2.2: Properties of Various Semiconductors.......... 39
Table 3.1: Parameters of Equatrion 3.1.......... 44
Table 3.2: Masetti Model Parameters 44
Table 3.3: Caughey-Thomas Expression Parameters.......... 45
Table 3.4: Germanium Impurity Ionization Energies 46
Table 3.5: SHR Model Parameters 47
Table 3.6: TAT Parameters.......... 47
Table 3.7: BTBT Parameters 47
Table 3.8: Barrier Structures.......... 55
Table 3.9: Heterojunction Simulations Tabulated 56
Table 3.10: Scintillator Decay Times 68
Table 4.1: Passivation Experimental Steps Combinations.......... 76
Table 4.2: Ohmic Contact Combination List.......... 83
Table 5.1: Devices Fabricated for X-Ray Testing 92
Table 5.2: ALS Operational Parameters 95

Acknowledgements

This work would not have been possible without the help of very many people along my path. First, I would like to thank all my lab mates, Anne Garafalo, Ankit Kumar, Jose Andres Orozco, Mary Ann Mort, Jordan Ricci for their amicable camaraderie during graduate studies as well as encouragement and moral support, and for their willingness to help when I asked for it. Most of all I would like to thank Ziang "Miles" Guo for his tireless work during the many long hours in the clean room together, fabricating photodiodes and learning how to use the equipment together, and for his friendship.

I would like to thank the staff of CNM2 in UC Davis, including Ryan Anderson, Vishal Narang, Paula Lee, Chan Ho Kim, Yusha Bey, and most of all Siwei Li for showing up at all hours of the night to help me troubleshoot issues with fabrication technology. Next, I would like to thank all the staff of LLNL who helped me, including Qinghui Shao for his technical expertise, Lars Voss for his direction, and especially Arthur Carpenter for his advice and believing in me and in this project. Next, I would like to thank Professor Charles E. Hunt from the bottom of my heart for his kind and wise support and guidance, and for being patient with my many flaws and my often-slow work. Without Professor Hunt this dissertation would not have happened.

Finally, I would like to thank my fiancé, Katie Oleynichenko, and family, my parents Galina and Vladimir and my dear brother Alex, who have been endlessly supportive of my dreams. I love you all from the bottom of my heart.

Chapter 1 – Introduction

1.1. Motivation

Radiographic imaging has a wide range of uses in scientific research, industry, medical imaging, and security applications. At the National Ignition Facility (NIF) at Lawrence Livermore National Laboratory (LLNL), hard x-rays are used to image the experimental laser-driven internal confinement fusion reactor. Completed in September of 2001 and aimed at developing next generation safe commercial nuclear power generation, materials research, and nuclear weapon stockpile support, the reactor focuses 192 ultraviolet (UV) lasers at a hohlraum containing a deuterium-tritium (DT) target. The laser heating of the gold hohlraum triggers the release of M-band x-rays, which bathe the target and triggers a fusion reaction [1-3]. A critical milestone in achieving its power and stockpile support goals lies in driving the plasma during the experiment to a burning plasma regime, in which the thermonuclear fusion reaction is self-sustaining. Each fusion event releases a 14.1 MeV neutron and a 3.5 MeV alpha particle, and if the target pressure is high enough, alpha particles deposit

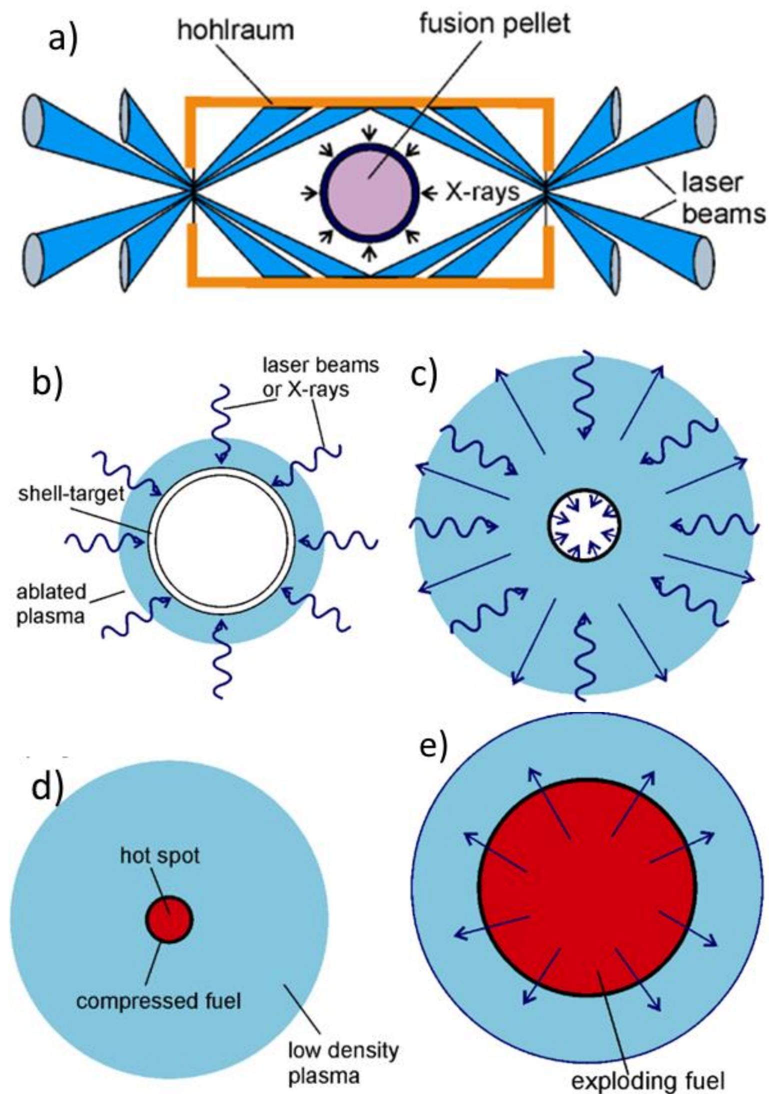

Figure 1.1 – High level overview of NIF process. A) lasers bombard hohlraum with 325nm UV lasers, stimulating the production of x-rays. B) x-ray bath of target begins ablation of outer shell triggers compression of DT interior. C) inner DT core continues compression as outer shell fully ablates. D) target reaches peak compression in with self-heating thermonuclear reaction is activated. E) Target explodes. Images reproduced from [2].

their energy into surrounding ions, leading to a cycle of self-heating in the hot spot, a process called alpha heating [1]. A very high-level overview of this process is demonstrated in Fig. 1.1.

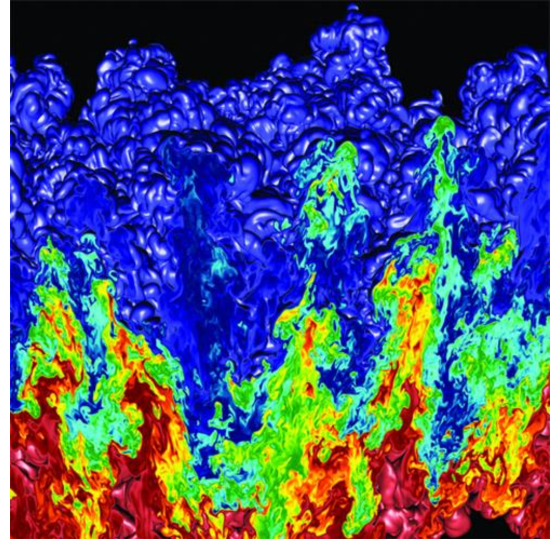

Figure 1.2 – MIRANDA code simulation of DT target during implosion. Plasma turbulence can be seen between the three layers, the diamond outer shell (blue), DT ice (green), and DT body. Image courtesy of LLNL.

In the decades since its construction, however, NIF has faced difficulty in reaching the burning plasma regime, and thus the energy yield of the reactor remains less than needed to initiate the process. Even when ignition has been reached, repeatability has been difficult. This is known to be due to hydrodynamic plasma instability, including Rayleigh–Taylor and Richtmyer–Meshkov instabilities, and intermixing during the ablation and compression phases of the experiment, which cause an unstable interface of the DT and outer ablator layer [1]. This disrupts the extremely high degree of symmetry needed for the experiment. The causes of instability include capsule surface roughness, impurities in the target and hohlraum, temperature differentials throughout the target, and driving laser non-uniformities [1, 2]. MIRANDA code simulations, a toolkit developed at LLNL for understanding and optimizing target behavior during the NIF experiment cycle, supports this claim. As seen in Fig. 1.2, significant intermixing can be seen between the various layers, suggesting the presence of strong turbulence in the capsule.

The purpose of this project is to construct a prototype high-speed germanium photodiode array to be used as a diagnostic in NIF that will, ultimately, introduce real-time, 4-frame plasma turbulence monitoring capabilities at higher x-ray energies than could previously be managed with silicon imaging arrays currently being used. The material of choice for the project is germanium that, due to its superior stopping power of x-rays as well as higher electron and hole mobilities than that of silicon, can provide superior x-ray imaging capabilities at lower material thicknesses, improving both image clarity and speed. As can be seen in Fig. 1.3, a 60µm thick germanium photodiode can achieve the same internal quantum efficiency as a 1000µm silicon photodiode due to the higher mass-attenuation coefficients of germanium in the x-ray energies of interest [4]. The emergence of high-quality epitaxial growth of germanium has made this project is ripe for engineering and is an ongoing attempt at LLNL [5].

1.2. Radiographic Imaging and NIF Imaging Requirements

Radiographic imaging is a tomography technique, a transmission imaging technique, in which hard x-rays are passed through a solid body and the outgoing intensities are recorded onto a recording medium, typically a film or detector array. Contrasts in the subject's localized mass density yields a map of differing exposures on the recording medium, producing a negative image. Applications of tomography are broad. Perhaps the best-known example is x-ray radiography used for medical imaging. Other applications include, but are not limited to, transmission electron microscopy (TEM) uses electrons to image material atomic structures, seismic waves are used for subterranean imaging of the Earth, optical

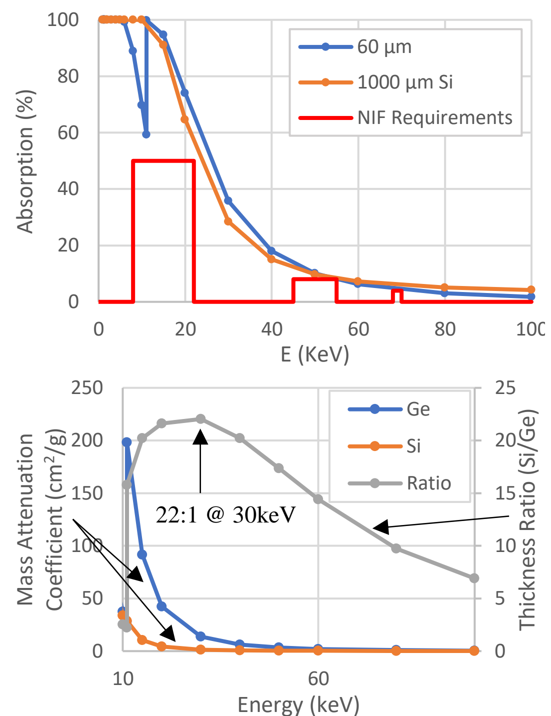

Figure 1.3 – (top) NIF QE requirements as well as the required thicknesses of germanium and silicon, and (bottom) thickness ratio of Ge and Si to achieve an equal quantum efficiency for the energy of interest. At its peak, the ratio curve has a value of 22:1. Data obtained from [4].

tomography is used in very many aerial, biological, and interferometry applications, ultrasound tomography is used in various biological applications.

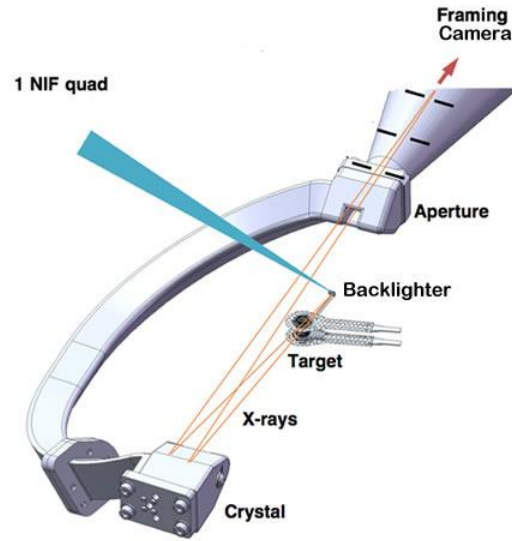

Figure 1.4 – Schematic setup of target, backlighter, and imaging sensor positions. Image courtesy of LLNL.

The imaging system for which this sensor is being developed operates on the same principle as other tomographic systems. During peak compression, a backlighter, a metal foil with one of the NIF lasers pointed at it, is used to generate x-rays that penetrate through the DT target at peak compression. These x-rays then propagate several meters to where the imaging array is mounted and collide in the form of plane waves. Processes internal to the semiconductor imaging sensor then convert the photon flux to current, read out locally in a 1024x512 array by the readout integrated circuit (ROIC). Fig. 1.4 demonstrates a conceptual drawing of the setup. What makes germanium so much more adept at imaging in this application than silicon is the interaction between the x-ray stopping power and short exposure time, leading to more charge being generated in the germanium imager per nanosecond than in an equally thick silicon imaging array.

Care must be taken when selecting the x-ray imaging energy. If the energy is too low, none of the x-rays will penetrate the subject, yielding in no exposure of the recording medium. If the energy is too high, the x-rays penetrate all material too well, leading to an overexposed image. Fortunately, x-ray energies that produce well-exposed images of the DT target at peak compression, which at peak compression has roughly 1GBarr of pressure, have already been determined and are seen in Fig. 1.3 (labelled “NIF Requirements”), simplifying the project significantly.

While there are significant x-rays emanating from the hohlraum, as can be seen in Fig. 1.1, most x-ray generation occurs before the compression phase of the experiment, which reduces the noise in the imaging process. Furthermore, the fluence of any other particles emitted during the process decreases with the

distance between the imaging array, over the area of the imaging array. This significantly reduces the direct x-ray impact by a factor of 6×10^{-11} due to the small solid angle, calculated using equation 1.1 (given the distance stated above and an imaging array size of 1.0”x0.5” and 5 meters between the imaging array and the center of the NIF target chamber [6]). This simplifies the considerations of device design significantly.

$$\Omega = \frac{3\left(d^2 + \frac{s_{Det}^2}{2}\right)\int_0^{\pi/4}\left[tan^{-1}\left(\frac{s_{Det}}{2dcos\ \theta}\right)\right]^2 d\theta}{\pi\sqrt{d^2 + 2s_{Det}^2}} \tag{1.1}$$

Where Ω is the solid angle, d is the distance of the detector from the spherical center, s_{Det} is the length of a side of a square detector, and $d\Theta$ is infinitesimal angle over which the area integral is being calculated. This equation will be revisited and given a more careful examination in Chapter 5, where it is relevant in calculating expected currents generated by an x-ray source.

1.3. Imaging Array High Level Specifications

The design goals of the array are thus:

1. Device must have an external quantum efficiency of at least 4% at 70 keV.
2. Device must have a temporal response of less than 1ns at all energies of interest.
3. Device must be able to interface with the Icarus and Daedalus series of readout integrated circuits (ROICs) [7, 8, 9].
4. Device must not cause dielectric breakdown during duplex imaging operations.
5. Device must be suitable for photon counting applications.
6. Signal to noise ratio must be at least 10:1.

As can be seen in Fig. 1.2, a thickness of 60μm produces the sufficient stopping power necessary to meet NIF requirements. A thickness of 60μm is also sufficiently thin to produce a temporal response of 1ns, assuming capacitive effects produced by the fabrication process do not significantly slow down the device. Given this assumption, this calculation can be done with equation 1.2.

$$t = \sqrt{{t_{v,sat}}^2 + {t_{cap}}^2} \approx \sqrt{\left(\frac{d}{v_{sat}}\right)^2 + \left(\frac{R\varepsilon A}{d}\right)^2} \approx \sqrt{\left(\frac{d}{v_{sat}}\right)^2} \tag{1.2}$$

Where t is the maximum time it takes to evacuate a hole from the photodiode, $t_{v,sat}$ is the transit time of the charge carrier of the thickness of the photodiode, t_{cap} is the time it takes to evacuate the capacitor of charge, d is the thickness of the photodetector, v_{sat} is the saturation velocity of holes in the detector, R is the series resistance of the read out circuit, ε is the dielectric constant of the material, and A is the area of the detector. Given values found in [10] and disregarding the effects of capacitance, we get:

$$t = \sqrt{\left(\frac{60 \times 10^{-4} cm}{1.9 \times 10^{7}\, {}^{cm}/_{s}}\right)^2} = 320ps$$

The central problem of this dissertation is thus to find an epitaxial photodiode design with an intrinsic thickness of at least 60µm that can be fully depleted, and in which fabrication and material choice of the device does not significantly capacitively load the photodiode array.

Requirement 3 design goal is achievable by considering the pixel pitch of the Daedalus ROIC: 25µm x 25µm in a 1024x512 array, having a common cathode architecture [7]. Duplex mode is the act of biasing only half of the imaging array, while the other half of the array anodes will be at 0V. The risk of dielectric breakdown during high voltage operations is clear: contiguous pixels along the bias differences must not arc and destroy the sensor. Requirement 5 necessitates multiplicative processes of charge carriers, specifically impact ionization, must not be present in the photodiode, or at least be as small as possible. While a multiplicative process can be beneficial in a system used strictly for imaging, imaging and photon counting are different enough that this impacts design requirements. Finally, the imaging systems must have a signal to noise ratio must be at least 10:1 for it to be usable in practice.

1.4. Dissertation Overview

This chapter introduced the basic problem to be overcome and provides a potential solution in the form of germanium photodiode arrays, which can image harder x-rays at thinner thicknesses than the silicon arrays

currenting being used at NIF. Chapter 2 provides a basic introduction to x-ray interaction with matter, semiconductor photodiodes, a comparison of germanium x-ray absorption performance with other semiconductor materials, and a few basic x-ray photodiode designs. Chapter 3 provides a model for simulating germanium devices in Silvaco Atlas, an industry standard modeling tool, and explores solutions to the various design problems. Chapter 4 provides an overview of various fabrication challenges encountered, including surface passivation and cathode ohmic metallization. Chapter 5 provides optoelectronic testing results of fabricated photodiodes. Chapter 6 provides a brief overall conclusion of this work.

Chapter 2 – X-Ray Photodiodes

Radiation detector systems are designed to yield some information about incident radiation, which may include photons, electrons, neutrinos, ions, or other energetic particles. Key measurements include fluence, energy, direction, and position of interaction. Many different detectors exist which rely on different physics for detection, but they all rely on particles to interact with the absorbing material.

The most common semiconductor x-ray detectors are called photodiodes. To effective design an x-ray photodiode, we must first understand how x-rays interact with semiconductors. This chapter will do just that, describe how photons interact with matter, describes semiconductor photodiode device basics, as well as key device performance parameters. At the end of the chapter there will be a mention on other radiation detection systems at the. Though this is done less to explore radiation detection systems in general and more to justify germanium PiN structures and explore concepts that might be beneficial to incorporate when simulating devices.

2.1. Electromagnetic Radiation and its Interaction with Matter

X-rays begin at roughly 150 eV and increasing to infinite energy (so long as the photon does not originate from nuclear state changes, in which case it is classified as gamma radiation). When interacting with semiconductor detectors, x-rays ionize the absorber by the photoelectric effect to produce a signal. Specifically, photoabsorption occurs when a photon promotes an electron in a lower energy orbital to one in a higher energy level, and the difference in orbital energy levels is equal to the photon energy. As the energy of a photon increases, however, its wavelength decreases, also decreasing the likeliness of interaction with an electron in the material, and thus the probability of a photoabsorption. This probability can be calculated with Fermi's Golden Rule (equation 2.1a), and is known commonly as the absorption cross section, σ_ε (equation 2.1b), found on pages 8 and 10, respectively, of [11].

$$p = \frac{2\pi}{\hbar} \left| \langle \psi_f | H | \psi_i \rangle \right|^2 \rho_f \tag{2.1a}$$

$$\sigma_\varepsilon = \frac{4\pi\hbar^2\alpha}{{m_e}^2\varepsilon}\left|\langle\psi_f|\vec{e}\cdot\vec{p}|\psi_i\rangle\right|^2\rho_f \tag{2.1b}$$

Where ε is the energy of the x-ray, $\psi_i$and $\psi_f$are the initial and final states of the electron wave function, ρ_f is the density of final states, α is the fine structure constant, m_e is the rest mass of an electron, $\vec{e}$ is the x-ray polarization vector, $\vec{p}$ is the momentum operator, and ρ_f is the density of final states. The absorption cross section can be solved computationally using a density functional theory (DFT) solver, as noted on page 10-1 of [12]. Once found, it can be used to calculate the mass-attenuation coefficient of a material, Equation 2.2 [4]:

$$\mu_\varepsilon/\rho = \frac{N_A}{A}\sigma_\varepsilon \tag{2.2}$$

Where μ_ε/ρ is the mass-attenuation coefficient for energy ε, N_A is Avogadro's number, and A is the atomic weight. Using the mass-attenuation coefficient, we then calculate the material linear attenuation coefficient for energy ε [4]:

$$\mu_\varepsilon = (\mu_\varepsilon/\rho)\rho \tag{2.3}$$

Where ρ is the material density. Finally, this equation can be used to calculate the attenuation of photons in matter, which is governed by the Beer-Lambert law, equation 2.4a. If we modify this equation slightly, we obtain the equation for the internal quantum efficiency, that is, the absorption efficiency, of the material, as seen in equation 2.4b, also called the Beer-Lambert Law, found on pages 755 and 749, respectively of [13].

$$I(x) = I_0 exp(-\mu_\varepsilon x) \tag{2.4a}$$

$$\eta = 1 - exp(-\mu_{\varepsilon} x) \qquad (2.4b)$$

Where I_0 is the electromagnetic radiation intensity at the surface of the material in watts per unit area, x is the thickness of the material, I is the intensity of the electromagnetic radiation after propagating through thickness x of the material, and η is the internal quantum efficiency of the material. Equation 2.4b is of central importance in this dissertation because the internal quantum efficiency determines, theoretically, how much of the x-ray can be stopped by the material, and as will be seen in Section 2.2.5., how much current can be drawn from an incident x-ray.

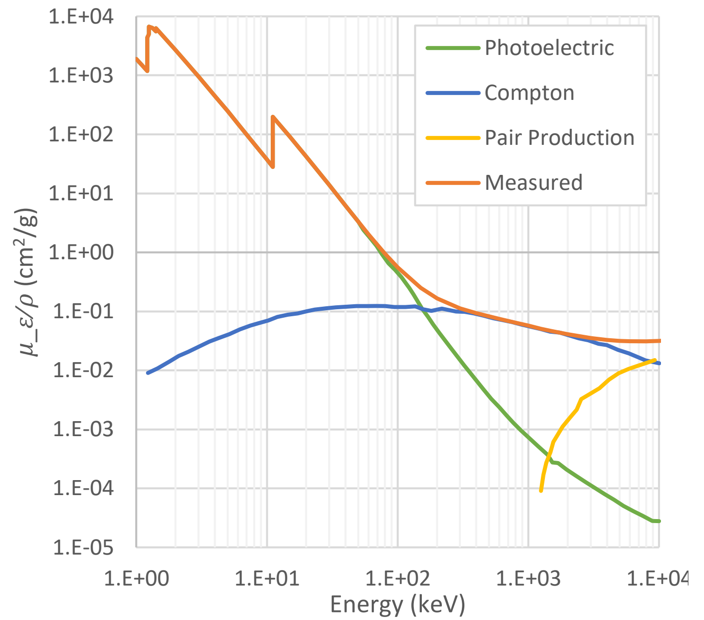

Figure 2.1 – Measured mass-attenuation coefficients for germanium (orange), as well as the contributions of the photoelectric affect (green), Compton scattering (blue) and pair production (yellow). Data obtained from [4].

This analysis however does not paint a complete picture of the interaction of radiation with matter. At energies lower than 100keV, the photoelectric effect dominates photon absorption, and so mass-attenuation coefficients can be calculated using equation 2.3, as stated. At energies higher than 100 keV, other effects dominate the absorption process, specifically Compton scattering and pair production. Figure 2.1 shows the mass attenuation coefficients for germanium from 1keV to 10MeV for all three effects as well as

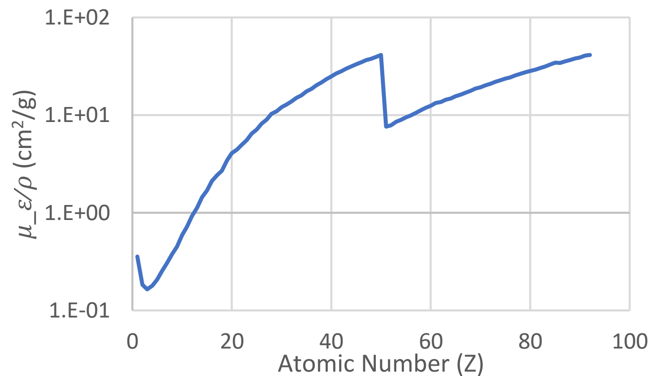

Figure 2.2 – Mass attenuation coefficients for elemental media for 30 keV x-rays. The dip in mass attenuation coefficient at Z=52 is due to the k-shell transition energy exceeding 30keV. Data obtained from [4].

the measured values. While solving these equations is a useful exercise, in this dissertation these coefficients are obtained from [4] when needed.

The implication of this figure however is clear: the higher the x-ray energy, the thicker the absorber must be to interact with and subsequently detect the x-ray. If for example the x-ray being investigated is 1keV, the germanium absorber must be on the order of a few micrometers for 99% absorption. If, however, the x-ray being investigated is 1MeV, the thickness must be in the hundreds of centimeters for the same absorption. This absorption percentage is called quantum efficiency. Because the energies that will be measured as lower than 100 keV, Compton scattering and pair production effects can be neglected in measurements, simplifying the project.

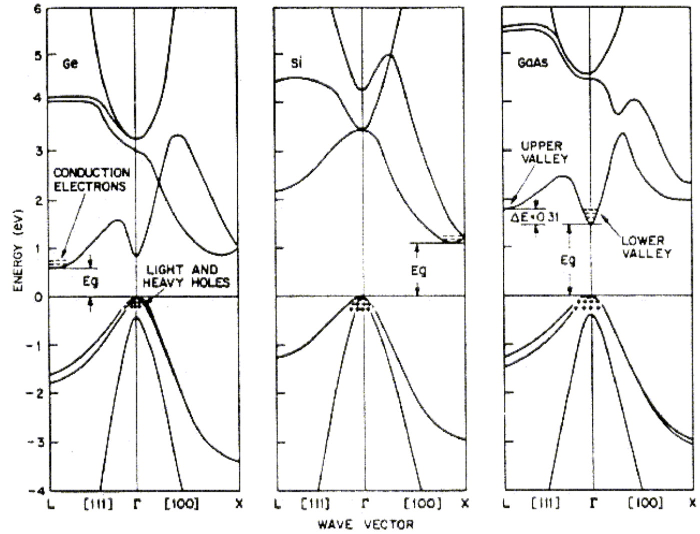

Figure 2.3 – Band structures of (left) germanium, (middle) germanium, and (right) gallium arsenide. Image reproduced from [13].

While it is not obvious from the equations above, the absorption cross section is roughly proportional to the atomic number of the material in elemental media, though because it is complicated by electron orbital structures, we cannot say that the two are directly proportional. This is illustrated in Figure 2.2 for 30 keV x-rays. It is for this reason that the usage of germanium is more advantageous than silicon for x-ray detectors. More x-rays can simply be stopped per unit length of material. Thus, the energy range of interest dictates the photodiode design.

2.2. Germanium Material Properties

2.2.1. Energy Bands and the Fermi Function

Semiconductors are a class of materials whose chemical structure produces forbidden energies in the electron orbitals of the crystal, page 116 of [15]. Due to the wave nature of subatomic particles, constructive

and destructive interference causes some energies to be allowed and others to be forbidden, as can be seen when using the Kronig-Penney potential when solving the Schrodinger equation, pages 29 and 16, respectively, of [15, 16]. This produces the band structure, in which some energies in the crystal are occupied, while others are completely empty. The energy difference between the most energetic valence orbital and the least energetic conduction orbital is called the band gap, an important parameter in semiconductors, page 12 of [17], 117 of [16], [17]. Figure 2.3 shows the band structures of silicon, germanium, and gallium arsenide (GaAs), three common semiconductor materials.

Electrons are fermions, and thus cannot occupy the same state with the same spin. This means electron behavior in semiconductors falls within the jurisdiction of Fermi-Dirac statistics (as opposed to Bose-Einstein statistics for bosons), pages 17 and 256 of [13, 16]. If we approximate the electrons in the material as a free gas in thermal equilibrium, known as the Sommerfeld model (page 278 of [16]), it can be shown that the distribution of electrons in energy states with energy E is given by the Fermi function, Equation 2.5, page 17 and 1067, respectively, of [13, 18].

$$F(E) = \frac{1}{exp\left(\frac{E - E_F}{kT}\right) + 1} \tag{2.5}$$

Where k is the Boltzmann constant, a constant that relates the temperature of a gas with the mean kinetic energy of particles in that gas, T is the temperature of the material, and E_F is the fermi energy of the material, the energy, the difference between the highest filled state at absolute zero. For intrinsic semiconductors, the Fermi energy is half of the bandgap energy. The bandgap energy for germanium at absolute zero is 0.74eV, and so the Fermi energy at absolute zero is 0.37eV, page 15 [13]. The Fermi function is plotted for germanium for several temperatures in Figure 2.4. There is a temperature dependence in the Fermi function because, as can be intuited from Equation 2.5, the higher the average kinetic energy of the electron gas, the higher the probability that particles exist in the system with enough energy to jump the band gap.

As noted, the occupation of an energy level in the forbidden band is not possible. Because the conduction bands are orbitals that are shared by the entire crystal, electrons in this band are free to move anywhere in the crystal. When an electric field is applied to the crystal, electrons in the conduction band thus contribute to the conductivity of the material. Likewise,

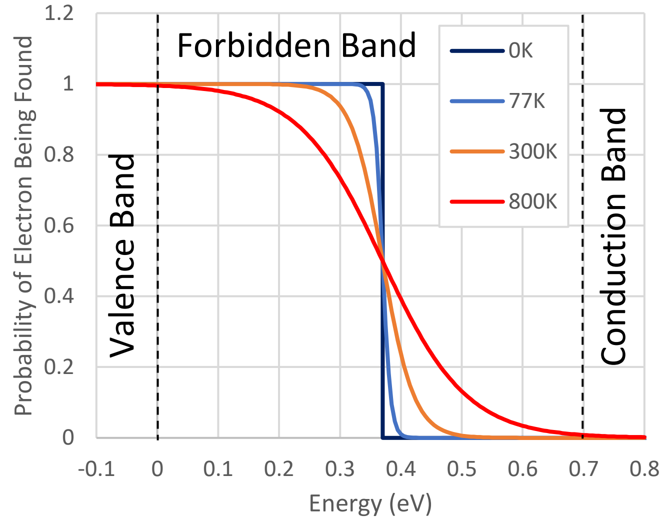

Figure 2.4 – The Fermi function plotted for germanium at various temperatures.

vacant states, called holes, move around the crystal and it is thus convenient to assign them a positive charge. They likewise contribute to the conductivity of the crystal in the event of an electric field being applied, only they move opposite to the direction of electrons. The total number of shared charge carriers in a crystal at thermal equilibrium per unit area is called the intrinsic charge carrier concentration and is denoted n_i. Energy bands cannot be understated in their importance, as it determines the class that the material falls into. Figure 2.5 the band structure of semiconductors, and for reference includes metals.

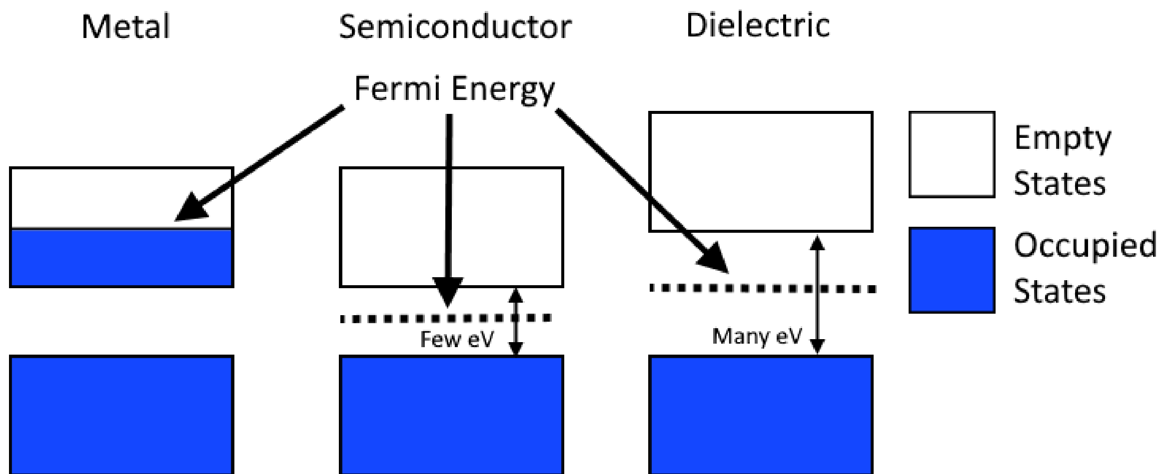

Figure 2.5 – Fermi energies for three common materials: (left) metals, (center) semiconductors, and (right) dielectric crystals.

2.2.2. Electrically Active Impurities

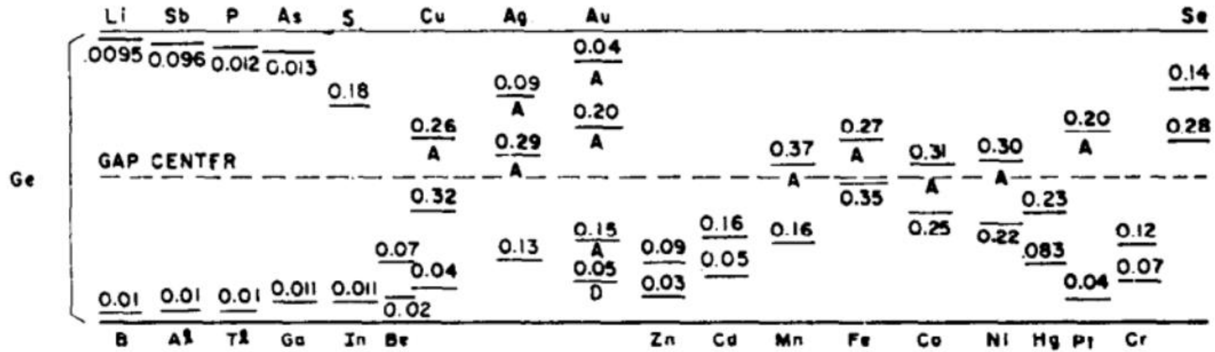

Figure 2.6 – Impurity ionization levels of important impurities for germanium. Distance from top bar to demarked line is the ionization energy for donors, and distance from bottom bar to demarked line is ionization energy for acceptors. Reproduced from [13].

If temperature were the only way to modulate the conductivity of semiconductors, they would be curious but ultimately not very useful materials. However, by adding impurities into the material that replace semiconductor atoms in the lattice, which are called electrically active impurities, we can modulate the number of charge carriers that are present in the material at a given temperature, as well as which is more numerous in the body, holes or electrons, page 20 of [13], [18, 19, 20]. The number of electrically active impurities per unit volume is called the impurity concentration, and is denoted N_D for donors, electron sources, and N_A for acceptors, hole sources, pages 20-24 of [13].

When a semiconductor has no impurities, it is called intrinsic. When it contains impurities, it is called extrinsic. When the impurity concentration approaches a sizeable portion of semiconductor atoms in the lattice, the semiconductor is called degenerate, and the behavior of the semiconductor at room temperature becomes quasi-metallic. Figure 2.6 contains common impurities for germanium and their ionization energies, the energy impurities in the lattice must absorb to donate a hole or electron to the lattice.

Given the temperature, impurity concentration, and bulk semiconductor material, and impurity type, we can calculate the carrier concentration per unit volume using Equations 2.6, Equation 2.7 a and b, and Equation 2.8. At relatively high temperatures, when impurities are nearly fully ionized, Equation 2.6 demonstrates the relationship between holes, electrons, and impurity concentrations. Equation 2.7a is used to calculate the Fermi level for an n-type majority doping, and 2.7b for p-type majority doping. Equation

2.8, known as the mass-action law under equilibrium, demonstrates the relationship between the number of holes, electrons, and intrinsic carrier concentrations per unit volume under thermal equilibrium conditions, an important relationship for any semiconductor, page 25 of [13].

$$n + N_A = p + N_D \tag{2.6}$$

$$N_c exp\left(-\frac{E_c - E_F}{kT}\right) = \frac{N_D}{1 + 2exp\left(\frac{E_F - E_D}{kT}\right)} + N_V exp\left(\frac{E_V - E_F}{kT}\right) \tag{2.7a}$$

$$N_V exp\left(\frac{E_V - E_F}{kT}\right) = \frac{N_A}{1 + exp\left(\frac{E_A - E_F}{kT}\right)} + N_V exp\left(-\frac{E_C - E_F}{kT}\right) \tag{2.7b}$$

$${n_i}^2 = np \tag{2.8}$$

Where N_c is the effective density of states in the conduction band, E_c is the conduction band energy, E_F is the Fermi level (which unfortunately has the same denotation as the Fermi energy), k is the Boltzmann constant, N_D is the donor impurity concentration per cubic centimeter, and E_D is the donor impurity ionization energy. The Fermi level is the Fermi energy adjected for the crystal temperature and impurity concentration. Once the Fermi level is found, equations 2.9a and 2.9b can be used to calculate the number of electrons or holes in the material, page 17 of [13], [19].

$$n = n_i exp\left(\frac{E_F - E_i}{kT}\right) \tag{2.9a}$$

$$p = n_i exp\left(\frac{E_i - E_F}{kT}\right) \tag{2.9b}$$

2.2.3. Carrier Transport Phenomena

There are five primary transport mechanisms of charge carriers in semiconductors: diffusion, drift, the Hall effect, thermionic emissions, and tunneling, corresponding to movement in the absence of any fields, movement in an electric field, movement in a magnetic field, carriers overcoming potential barriers, and carriers tunneling through potential barriers, respectively, pages 27-38 of [13], [21]. Of the first three phenomena, only the second transport mechanism is of any interest in photodiodes, drift, which responsible for efficient collection of photogenerated charge carriers. The relationship between drift velocity of a charge carrier and electric field is given in equation 2.10a and 2.10b from page 27 of [13], for electrons and holes, respectively. A lack of an electric field or the presence of a magnetic field are undesirable. The last two phenomena have to do with contact formation in this dissertation. They will be examined more closely later in Chapter 4.

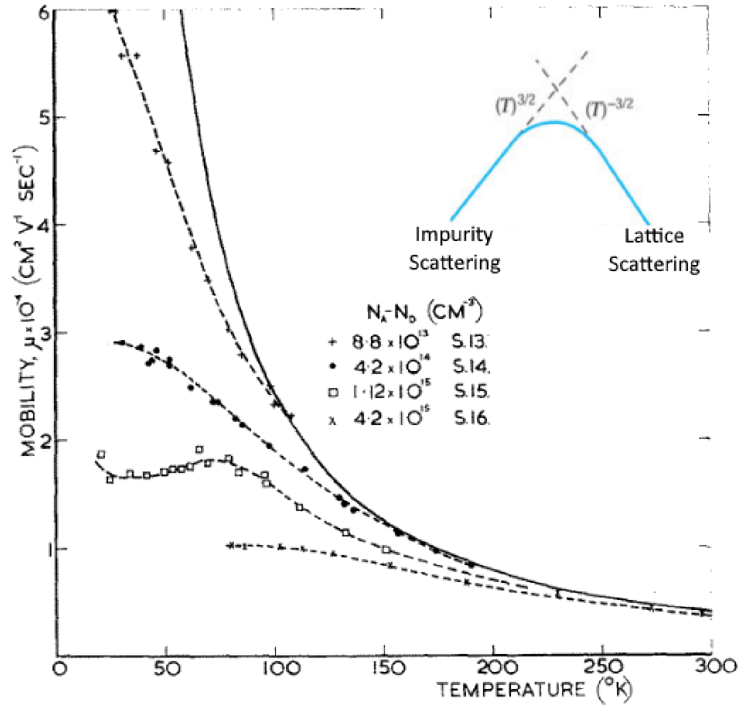

Figure 2.7 – Mobility of carriers in germanium as a function of temperature from [23].

$$\overrightarrow{v_n} = -\mu_e \vec{E} \quad (2.10a)$$

$$\overrightarrow{v_p} = \mu_h \vec{E} \quad (2.10b)$$

Where $\vec{E}$ is the electric field vector at a given position, and μ the carrier mobility, a proportionality factor between the electric field and velocity. It is important to note that holes and electrons both have separate mobilities. Various factors affect the carrier mobility, including crystal quality (defects), crystallographic orientation, impurity concentration, phonons, and so on. Each of these variables affects the mobility separately and are combined with Matthiessen's rule for the mobilities that dominate in the material, Equation 2.11 from page 28 of [13].

$$\frac{1}{\mu} = \frac{1}{\mu_{lattice}} + \frac{1}{\mu_{impurities}} + \cdots \tag{2.11}$$

Two important contributions to mobility for any semiconductor are lattice (phonon) scattering and impurity ionization scattering, which occur from carrier interaction with atoms in the crystal lattice and coulombic interaction from the ionized impurities, respectively, pages 27-30 of [13], [21, 22, 23, 24]. Figure 2.7 demonstrates experimentally measured mobility as a function of impurity concentration and temperature, as well as well as the theoretical relationship between mobility, impurity concentration, and temperature. Figure 2.8 demonstrates experimentally measured drift velocities of electrons for germanium as a function

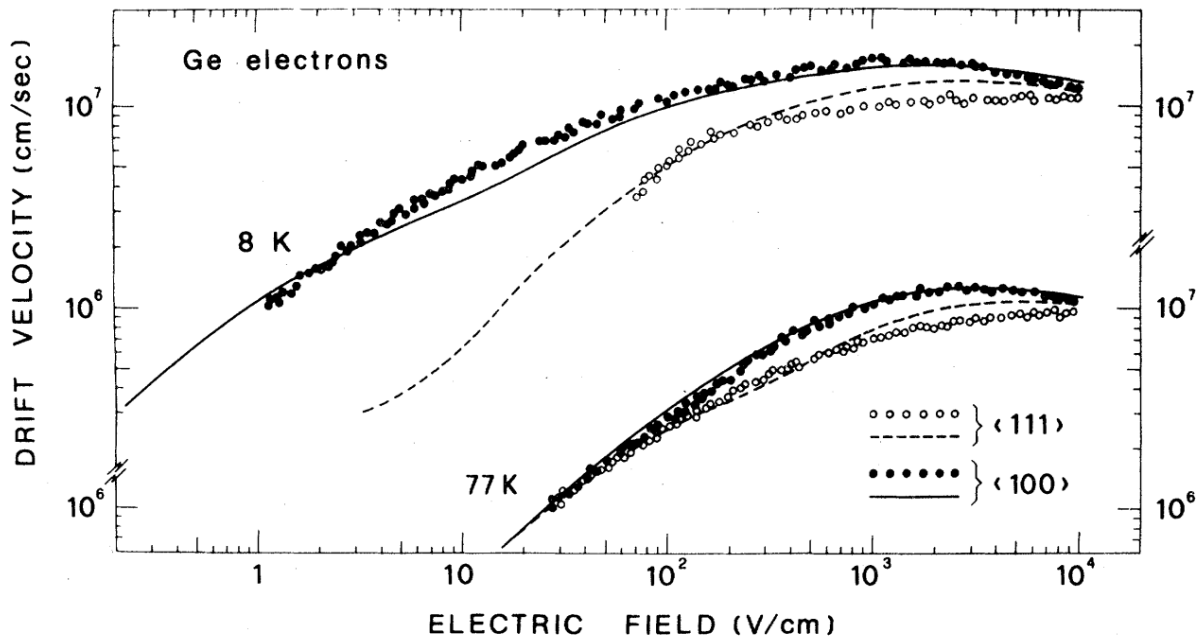

Figure 2.8 – drift velocity of germanium electrons at various temperatures. Figure reproduced from [21].

of temperature, electric field, and crystallographic orientation, denoted by Miller indices. As is suggested by Figure 2.8 (but by no means proven, other crystallographic orientations are possible), germanium orientation <100> is preferred for a higher mobility. Specific contributions to mobility and mathematic models will be examined in Chapter 3, where they are directly relevant to device modeling.

Observe from Fig. 2.8 that drift velocity peaks at an electric field strength of ~10^3 $V/_{cm}$. This maximum velocity is called the saturation velocity, and the field strength at which this occurs is called the critical field. Attaining saturation velocity is of central importance to fast detector design as transit speed of the carriers out of the semiconductor is minimized when velocities are at this value. It is for this reason that the critical field throughout the semiconductor is desired, and as will be seen later in this chapter, is determined by the bias applied to a photodetector as well as the ratio of impurities in the P-doped anode and the intrinsic region of a PiN photodiode.

2.2.4. Generation, Recombination, and Carrier Lifetimes

Just as bound electrons can be spontaneously stimulated to jump the bandgap and form an electron-hole pair, electron-hole pairs can come into contact and recombine, releasing a photon and acoustic phonon into the lattice, pages 35-36 of [13], pages 390-392 of [25], [26]. Whenever the equilibrium of the carrier relationship in a semiconductor is disturbed (Equation 2.8 does not hold), one of two phenomena will restore the crystal to equilibrium status.

If $pn > n_i{}^2$, recombination effects decrease excess carriers until equilibrium is reestablished. In general, holes and electrons do not have the same recombination rate, and so their lifetimes, τ_p and τ_n respectively, determines how long excess carriers will exist in the material, page 35 of [13], pages 389-390 of [25], [26, 27]. More precisely, τ is the average time an excited carrier exists in an excited state before recombining. If $pn < n_i{}^2$, generation effects increase the deficiency of carriers until equilibrium is established. This quantity is denoted by τ_g. Equations 2.12a and 2.12b demonstrates the relationship between excess carrier

recombination and a single generation pulse. Equations 2.13a and 2.13b demonstrate carrier generation but for a pulse in which carriers are depleted, page 398 in [25].

$$\Delta n(t) = \Delta n_0 exp\left(-\frac{t}{\tau_n}\right) \tag{2.12a}$$

$$\Delta p(t) = \Delta p_0 exp\left(-\frac{t}{\tau_p}\right) \tag{2.12b}$$

$$\Delta p(t) = -\Delta p_0 exp\left(-\frac{t}{\tau_g}\right) \tag{2.13a}$$

$$\Delta n(t) = -\Delta n_0 exp\left(-\frac{t}{\tau_g}\right) \tag{2.13b}$$

Where Δn and Δp are excess electrons and holes, Δn_0 and Δp_0 are the initial number of excess carriers. Figure 2.9 demonstrates minority carrier lifetimes of germanium samples of various purities and temperature. Like mobility, lifetimes likewise follow Matthiessen's rule, page 28 [13].

$$\frac{1}{\tau} = \frac{1}{\tau_{SRH}} + \frac{1}{\tau_{Rad}} + \frac{1}{\tau_{Auger}} \dots \tag{2.14}$$

There are several important phenomena that determine the generation and recombination rates of carriers in semiconductors that can be divided into two categories: bulk effects and surface effects, pages 389-390 [25], [26, 27]. Generation increases device leakage current, which will be discussed Section 2.2.5, and recombination decreases signal evacuation efficiency from the detector. Thus, generation and recombination effects decrease the overall signal to noise ratio of the detector, and understanding and addressing them is paramount to detector design. Due to the importance each, they will be treated separately in the sections that follow.

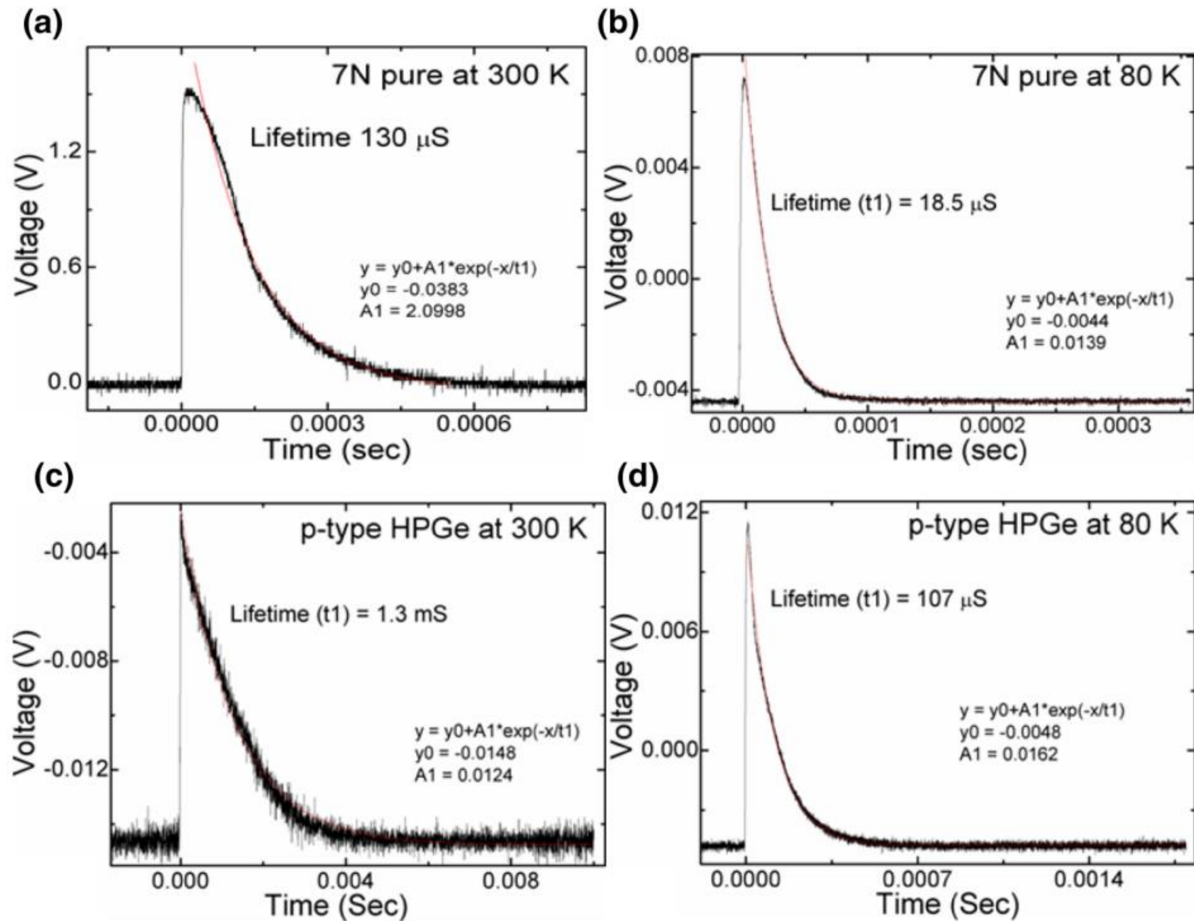

Figure 2.9 – Measured minority lifetime carrier lifetimes in various purities of germanium. Reproduced from [28].

2.2.4.1. Bulk Recombination Effects

In germanium, trap-assisted recombination dominates within the body of the material. To a much lesser extent, band-to-band recombination occurs in germanium as well, releasing energy in the form of a photon in the *radiative process*, or to another free electron or hole in the *Auger process*. Band-to-band recombination is a larger concern in direct bandgap materials, where depending on the material, the rate of the occurrence can be five orders of magnitude higher, page 42 of [14]. Figure 2.10 demonstrates these three recombination phenomena.

Bulk traps stem from defects in the crystal, page 42 of [14], page 391 of [25]. Defects come in many forms, including dislocations, interstitials, and vacancies, page 13 of [29]. Some common defects are shown in

Figure 2.11, though knowledge of the various types of defects is not necessary to understand how defects in general impact device performance. The net transition rate can be described by Shockley-Read-Hall (SRH) statistics, Equation 2.15, page 35 of [13], 393 of [25], [30].

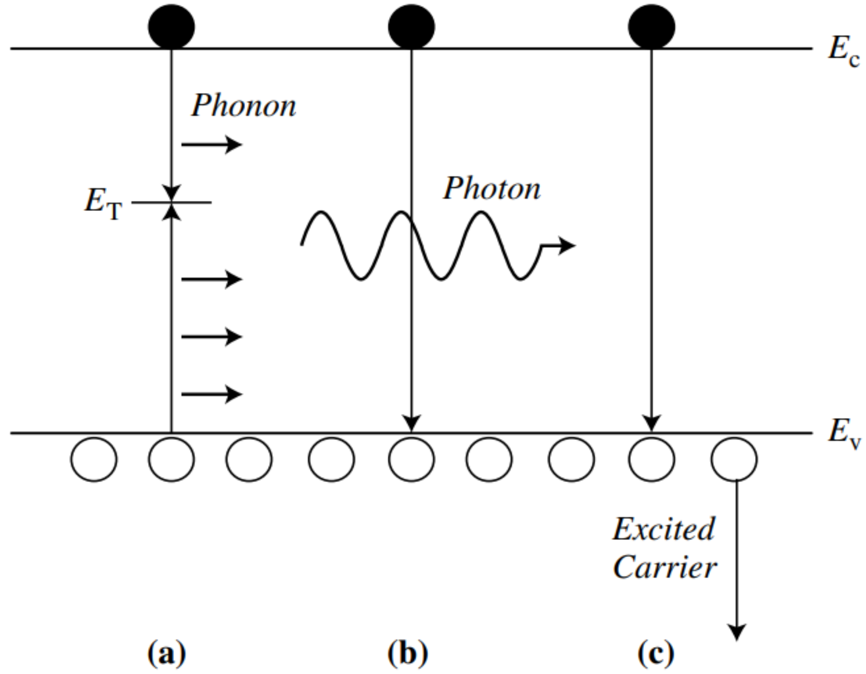

Figure 2.10 – (a) trap assisted recombination, (b) radiative recombination, and (c) Auger recombination. Image reproduced from [22].

$$U = \frac{\sigma_n \sigma_p v_{th} N_t (pn - n_i{}^2)}{\sigma_n \left[n + n_i exp\left(\frac{E_t - E_i}{kT}\right)\right] + \sigma_p \left[p + n_i exp\left(\frac{E_i - E_t}{kT}\right)\right]} \tag{2.15}$$

Where U is the net transition rate, σ_n and σ_p are electron and hole capture cross sections and depend on the specific defect type, $v_{th} = \sqrt{3kT/m_n}$ is the electron thermal velocity, m_n is the electron density-of-states effective mass, N_t is the bulk trap density, pn and pn are the hole and electron concentrations, n_i is the intrinsic carrier concentration, E_i is the Fermi energy of an intrinsic semiconductor, called the intrinsic energy, and E_t is the energy level of the trap, as seen in Figure 2.10(a). The net transition rate U is defined in Equation 2.16, page 42 of [14], 393 of [25], [30].

$$U = R_e - G_{th} \tag{2.16}$$

Where R_e is the recombination rate and G_{th} is the thermal generation rate. To calculate the carrier lifetimes using these relationships, a few simplifications must be made. Fist, observe in Equation 2.15 that U is maximized when $E_i = E_t$. Second, we must derive lifetimes under low-level injection and high-level injection conditions (discussed in Section 2.3). Using these, we find that equations 2.17a and 2.17b give the minority carrier lifetimes of holes and electrons under lower-level injection, and equation 2.17c gives the minority carrier lifetimes under high-level injection, page 43 of [14], 392 of [25, 30].

$$\tau_p = \frac{1}{\sigma_p v_{th} N_t} \tag{2.17a}$$

$$\tau_n = \frac{1}{\sigma_n v_{th} N_t} \tag{2.17b}$$

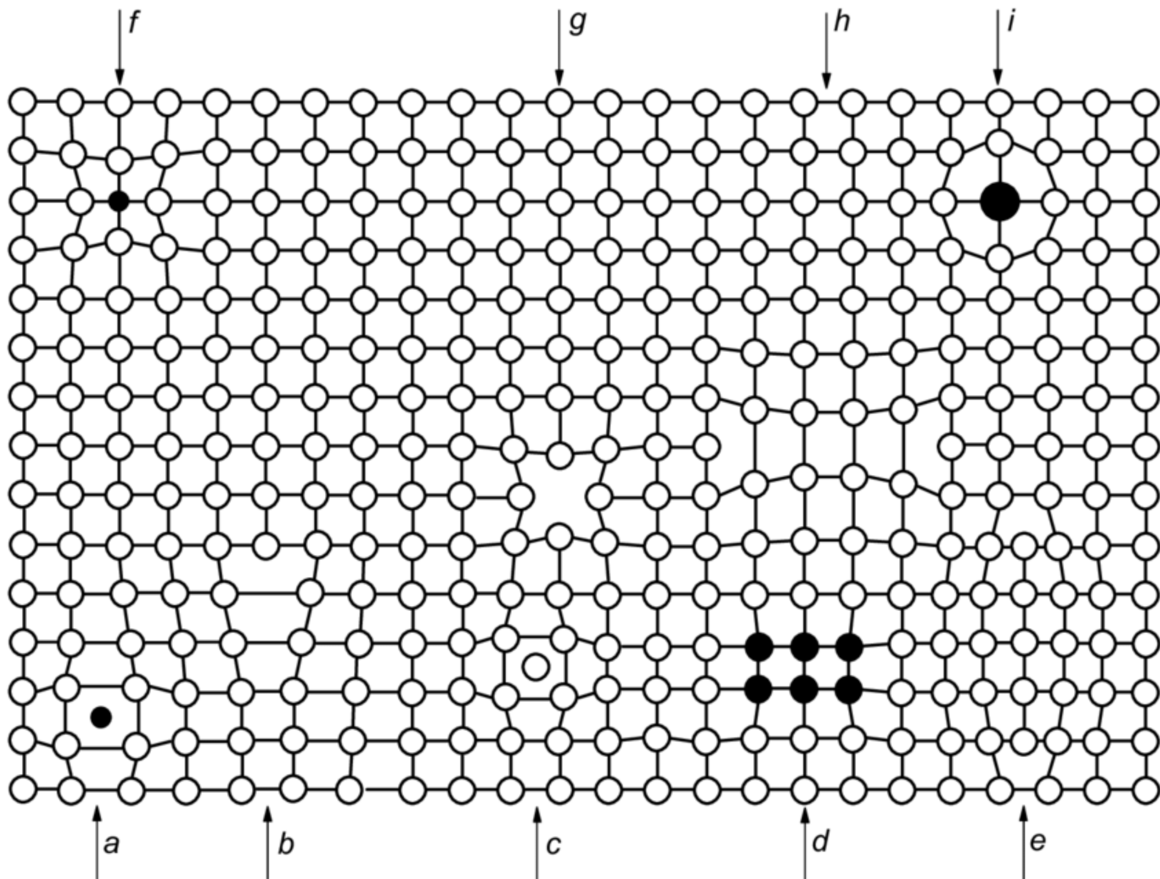

Figure 2.11 – a sampling of various crystal defects, including (a) impurity interstitial, (b) dislocation, (c) self-interstitial, (d) cluster of impurity atoms, (e) extrinsic dislocation loop, (f) small substitutional impurity, (g) vacancy, (h) intrinsic dislocation loop, and (i) large substitutional impurity.

$$\tau_p = \tau_n = \frac{\sigma_p + \sigma_n}{\sigma_n \sigma_p v_{th} N_t} \tag{2.17c}$$

In all three cases, the carrier lifetime is inversely proportional N_t, bulk trap density. Therefore, to maximize carrier lifetimes within the body of the semiconducting material, the crystal defect density must be minimized in the germanium photodiodes. This has a direct impact on external quantum efficiency, explored in Section 2.2.6. Defects in the crystal body will be explored further in Chapter 4.

As for band-to-band recombination, minority carrier life lifetimes are given by equations 2.18a and 2.18b under low-level injection conditions, and equation 2.18c under high level injection conditions, page 42 of [13], [30].

$$\tau_p = \frac{1}{R_{ec} N_D} \tag{2.18a}$$

$$\tau_n = \frac{1}{R_{ec} N_A} \tag{2.18b}$$

$$\tau_p = \tau_n = \frac{1}{R_{ec} \Delta n} \tag{2.18c}$$

The implications here are not as immediately obvious. In Chapter 3, it will be seen that the intrinsic region of epitaxially grown germanium has a relatively high impurity concentration of antimony, an n-type dopant in germanium. Because a common-cathode architecture collects holes to build an image, it is in the interest of image quality to maximize hole lifetimes in this region. We must therefore aim to decrease this impurity concentration for more efficient hole collection, although again this lifetime contribution is of secondary concern. Equation 2.14 lists lifetimes for radiative and Auger processes as separate contributions. In principle they are. However, because they both belong to band-to-band recombination processes and these are of only secondary importance here, further exploration of their individual contributions will not be discussed. The intrinsic region and PiN photodiode architecture will be discussed in Section 2.4.

2.2.4.2. Surface Recombination Effects

The same recombination phenomena that occur in the body of germanium occur in the body. Because of this, SRH statistics dominate along the surface as well, as seen in Equation 2.19. However, recombination on the surface occurs at a heightened rate caused by dangling bonds formed at the interface of the crystal body and the medium external to the semiconductor. To differentiate from bulk recombination lifetimes, surface phenomena are denoted by an s, page 394 of [25].

$$U_s = \frac{s_n s_p (p_s n_s - n_i{}^2)}{s_n \left[n_s + n_i exp\left(\frac{E_{it} - E_i}{kT}\right)\right] + s_p \left[p_s + n_i exp\left(\frac{E_i - E_{it}}{kT}\right)\right]} \tag{2.19}$$

Where N_{it} is the surface interface trap density, $s_n = \sigma_{ns} v_{th} N_{it}$, $s_p = \sigma_{ps} v_{th} N_{it}$, N_{it} is the surface interface trap density, and the subscript s signifies that the phenomenon is occurring on the surface. In times when the interface trap density N_{it} (cm^{-2}) is not constant, D_{it} $(cm^{-2}\ eV^{-1})$ must be used. The relationship between the two is in Equation 2.20, page 394 of [25].

$$N_{it} = \int D_{it} d\varepsilon \approx kT D_{it} \tag{2.20}$$

Once again, the goal is to use surface SRH statistics to solve for surface lifetimes. Before this can be done an additional concept must be introduced: surface recombination velocity, s_r, as the number of carriers recombining on the surface per unit area per unit time per unit volume of excess bulk carriers. Equation 2.21 demonstrates that mathematical definition of the surface recombination velocity, page 394 of [25].

$$s_r = \frac{R_s}{\Delta n_s} \tag{2.21}$$

Once again performing the simplifications from the bulk recombination section, and solving for low-level and high-level injection, we get Equations 2.22a and 2.22b respectively, page 394 of [25]. While lifetimes

from bulk defects are generally difficult to improve after the formation of the semiconductor crystal, lifetimes from surface defects can be substantially increased or decreased based on the surface passivation material, pages 400-401 of [25], [31]. This will be explored further in Chapter 4.

$$s_r = \frac{s_n s_p (p_s + n_s + \Delta n_s)}{s_n \frac{n_i}{p_s} + s_p \left(1 + \frac{n_i}{p_s}\right)} \tag{2.22a}$$

$$s_r = \frac{s_n s_p}{s_n + s_p} \tag{2.22b}$$

2.2.4.3. Bulk Generation Effects

There are three important carrier generation mechanisms in germanium: thermal generation, optical generation, and impact ionization. The first two have already been discussed. The last will be considered separately in Section 2.3. If $pn < {n_i}^2$, Equation 2.23 can be inferred from Equation 2.15, page 44 of [14].

$$G = -R = -\frac{\sigma_n \sigma_p v_{th} N_t n_i}{\sigma_n \left(1 + \frac{n}{n_i}\right) + \sigma_n \left(1 + \frac{p}{n_i}\right)} \equiv -\frac{n_i}{\tau_g} \tag{2.23}$$

Solving for τ_g we get Equation 2.24, utilizing the same simplification as in bulk recombination effects, page 44 of [14].

$$\tau_g = \left(1 + \frac{n}{n_i}\right)\tau_p + \left(1 + \frac{p}{n_i}\right)\tau_n \tag{2.24}$$

As can be seen, generation effects in the bulk crystal likewise depend on defect density within the crystal. It is therefore doubly important to minimize defects within the crystal.

2.2.4.4. Surface Generation Effects

As with bulk generation effects, surface recombination effects are also dominated by surface defect density. This is given by Equation 2.25, page 395 of [25].

$$s_g = \frac{s_n s_p}{s_n + s_p} \qquad (2.25)$$

2.2.4.5. Recombination-Generation Centers

As was seen in the previous sections, defects are responsible for both generation and recombination of carriers. These sites in the crystal lattice are called recombination-generation (R-G) centers. Because all these concepts are occurring simultaneously in the semiconductor crystal, and thus measurements thereof are difficult to separate. They are therefore all measured together as effective lifetimes. This will be revisited in Chapter 4, where methods of modulating lifetimes, specifically surface lifetimes, will be presented.

2.2.5. Material Responsivity and Photocurrent

As discussed in previous sections, the conductivity of a semiconductor thus changes vastly with temperature and density of electrically active impurities in the semiconductor. The photoelectric effect can likewise modulate the conductivity of the crystal. By imparting enough energy into electrons in valence band orbitals, they can be excited up to a conduction band. This energy is called the pair production energy, page 357 of [32], 146 of [33], [34].

Material	**Bandgap At 300K (eV)**	**Pair Production Energy (eV)**	**Responsivity (A/W)**	**Density (g/cm^3)**	**Mean Z**
Si	1.12	3.65	0.274	2.33	14
Ge	0.66	2.98	0.335	5.32	32
GaAs	1.42	4.2	0.238	5.32	32

Table 2.1 – optical material properties for silicon, germanium, and gallium arsenide from [13, 32, 34].

Using the electron-hole pair creation energy, we can calculate the responsivity of a semiconducting material using Equation 2.26, the expected number of charges generated per watt of irradiant power.

$$R = \frac{1W \times 6.24 \times 10^{18}\, {}^{eV}/_{J}}{1W} \frac{2q}{\varepsilon} \approx \frac{0.998}{\varepsilon} \frac{A \cdot eV}{W} \tag{2.26}$$

Where q is the charge of an electron and ε is the electron-hole pair creation energy in eV. Table 2.1 lists the bandgap, pair creation energy, and density of silicon, germanium, and gallium arsenide. In some literature the responsivity combines the equation derived above with the device quantum efficiency, thus making it a function of energy, such as equation 13 on page 749 of [13]. In this work they will be kept separate. This will make data processing in Chapter 5 more intuitive. Using this information, we arrive to an equation of central importance to this work, the relationship between the current from a semiconductor and the power being radiated on it, page 749 of [13], [34].

$$I_{x-ray} = PAR\eta \tag{2.27}$$

Where P is the power density being irradiated on the detector in ${}^{W}/_{cm^2}$, A is the area of the radiation beam, R is the responsivity of the material, and η is the quantum efficiency, the ability of the material to stop the incoming photons. The total current then, assuming no diffusion current, is given by Equation 2.28, pages 54-55, 755 of [13]:

$$I = I_{Dark} + I_{x-ray} \tag{2.28}$$

Where I_{Dark} is the inherent leakage current generated by the semiconductor internally. Leakage current will be discussed further in Section 2.3. This equation both illuminates the working of a semiconductor when detecting x-rays and paves a way for quantum efficiency measurements. All that is needed then is to measure the dark and bright current of a photodiode and the quantum efficiency can be calculated, assuming the x-ray source is characterized.

2.2.6. Internal and External Quantum Efficiency

Recall from Section 2.2.4. that charge carriers in a semiconductor have a finite lifespan. This phenomenon allows for photogenerated carriers to be reabsorbed by the semiconducting material before they reach the corresponding electrode for collection, thus reducing the measured current signal, depending on material purity and device design. However, the current equation presented in the previous sections assumes that all charge is evacuated from the body of the semiconductor, pages 754-758 of [13]. It is thus necessary to give the two phenomena separate names. The total power absorbed by the material is called the internal quantum efficiency and represents the best-case scenario for current being generated by a semiconductor detector. The external quantum efficiency is the quantum efficiency as measured by equation 2.25. This distinction will become important in Chapter 5.

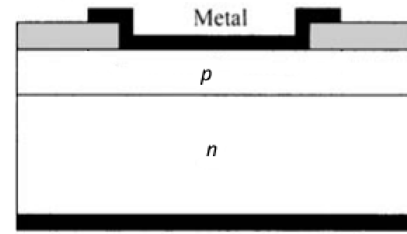

Figure 2.12 – Basic structure of a PN junction Photodiode. Image reproduced from [13].

2.3. Semiconductor Photodiodes

2.3.1. The PN Junction and Ideal Diode Equation

Once the basic semiconductor material properties are understood, they need to be combined to usable device. This is done with the PN junction, also known as a diode. The PN junction consists of a highly doped p-type region contiguously next to a n-type region. When electrodes are placed on both sides, the resulting device conducts current with non-linear characteristics with respect to voltage. Figure 2.12 demonstrates a cross section of a diode, as well as generic current-voltage (I-V) characteristics. Equation 2.29 is a formulation of the relationship between the bias applied between the two electrodes on a diode and the resulting current and is known as the ideal diode equation, page 87 of [13], page 454 of [35].

$$I = qA{n_i}^2\left[\frac{D_N}{L_N N_A} + \frac{D_P}{L_P N_D}\right] exp\left(\frac{qV}{kT} - 1\right) \tag{2.29}$$

Where I is the current flowing out of the device, V is the bias applied to the anode with respect to the cathode, q is the charge of an electron, A is the area of the diode, D_N and D_P are the diffusion coefficients of electrons in p-doped regions and holes in n-doped region, L_N and L_P are the average diffusion distance an electron travels in a p-doped region and a hole travels in an n-doped region before recombining, N_A is the impurity concentration in the p-doped region, and N_D is the impurity concentration of the n-doped region.

As can be seen in Figure 2.13, which is representative of a real diode, current characteristics are highly asymmetric with respect to voltage. When a positive bias is applied to the anode with respect to the cathode, current increases exponentially until a saturation point is reached. These two regions are called low-level injection and high-level injection, page 91 of [13]. When a negative bias is applied, as can be inferred from

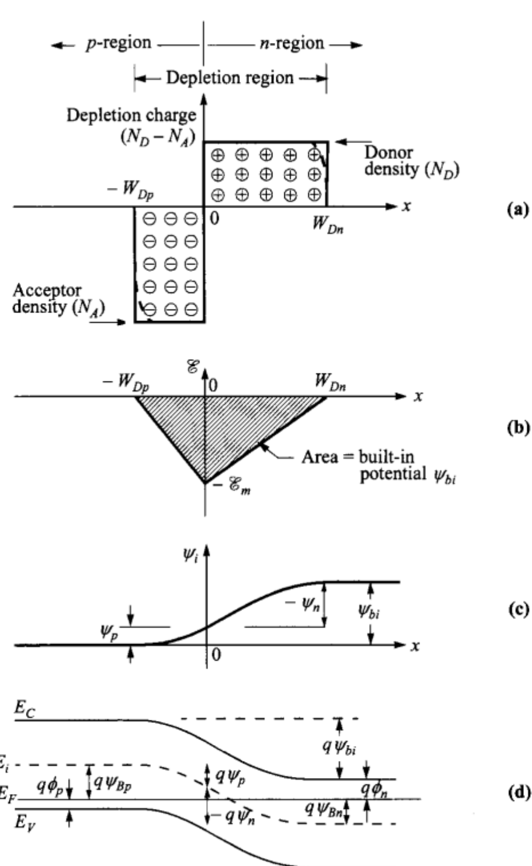

Figure 2.14 – (a) Depletion region stemming from ionized impurities in the lattice, (b) the electric field they generate, (c) the resulting potential difference from the electric field, and (d) the bending of the valence and conduction bands as a result. Image reproduced from [13].

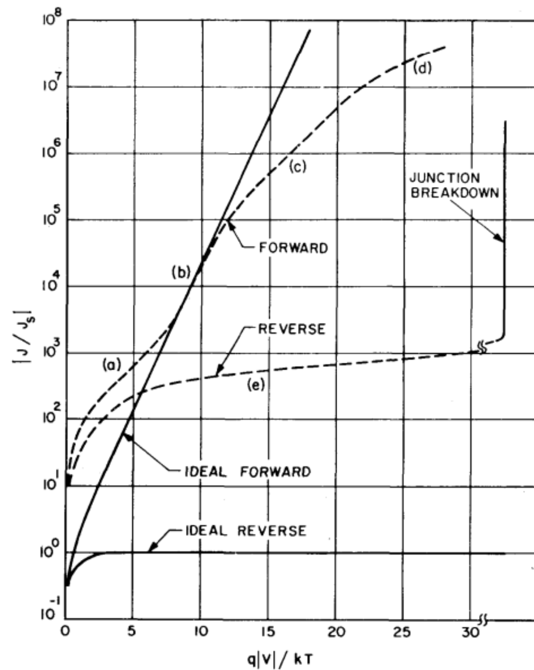

Figure 2.13 – Ideal and nonideal current of a PN junction. Distinct characteristics are (a) generation-recombination current region, (b) diffusion current region, (c) high-level injection region, (d) series resistance effect, and (e) reverse leakage current. Image reproduced from [13].

Equation 2.29, a very small leakage current, also called a dark current if no photogeneration effects take place, flows through the electrodes of the diode. The magnitude of the current increases gradually until a critical voltage is reached, called the breakdown voltage, at which point current flow magnitude again starts growing exponentially. To understand this phenomenon, which is of central importance in this dissertation, the depletion region and impact ionization must be discussed.

2.3.2. The Depletion Region, Impact Ionization, and Reverse Breakdown

At the interface of the p and n regions in a diode, the electrons and holes are attracted to each other and recombine via the Coulombic force. The result is the depletion region, a volume within the diode where only ionized impurities in the lattice remain, pages 74-75 of [13]. By the Coulombic force, because these ionized impurities have a net electric charge, they produce an electric field, page 76 of [13]. As a result of this electric field, there is a potential different between the two halves of the diode, called the built-in potential, page 75 of [13]. This can be seen in Figure 2.14 with an abrupt junction diode. The magnitude of this potential is given in Equation 2.30, page 75 of [13].

$$V_i = \frac{kT}{q} ln\left(\frac{N_D N_A}{{n_i}^2}\right) \tag{2.30}$$

The built-in potential is dependent on the product of the impurity concentration of both sides, assuming complete ionization of all impurities. Using the definition of voltage and Coulomb's law, we can use this expression to derive the electric field strength and the depletion region width, page 76 of [13].

$$\vec{E}(x) = \begin{cases} -\frac{qN_A}{\varepsilon}\left(x + W_{D,p}\right), -W_{D,p} \le x \le 0 \\ -\frac{qN_D}{\varepsilon}\left(-x + W_{D,n}\right), 0 \le x \le W_{D,n} \end{cases} \tag{2.31}$$

$$W_D = \sqrt{\frac{2\varepsilon}{q}\frac{N_D N_A}{N_D + N_A}V_i} \tag{2.32}$$

Where ε is the dielectric constant of the semiconductor, W_D is the width of the depletion region. In an asymmetric diode where $N_D \ll N_A$, and a bias is applied between the anode and cathode, Equation 2.32 becomes the Equation 2.33, page 77 of [13].

$$W_D(V) = \sqrt{\frac{2\varepsilon}{qN_D}(V_i - V)} \tag{2.33}$$

If the bias applied on the anode with respect to the cathode is positive, the depletion region width shrinks. If the bias is negative, the depletion region width grows, as does the electric field magnitude. Recall from Section 2.2.3 that charges within a semiconductor accelerate to a velocity in an electric field due to drift velocity. In the absence of photogeneration, the only charges affected by this electric field those that are thermally generated within the depletion region. As the bias falls further below 0V, the velocity magnitude of the carriers accelerated increases. Ultimately, carriers gain enough kinetic energy to allow electrons in the valence band to excite to the conduction band upon collision, producing more electron-hole pairs within the depletion region. This phenomenon is called impact ionization, page 37 of [14]. Figure 2.15 demonstrates the impact ionization rates of various materials for various electric field strengths at 300K. Unfortunately, due to the small bandgap of germanium, it has the highest impact ionization rates of all materials found in Figure 2.15.

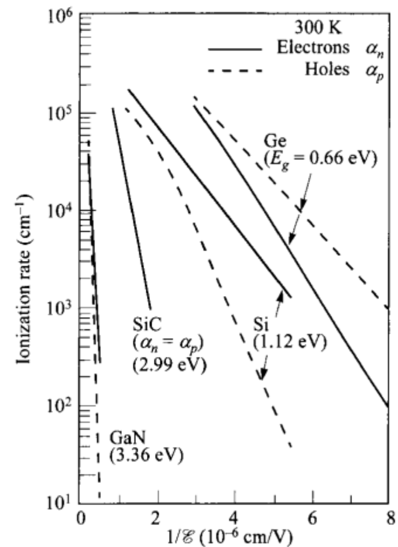

Figure 2.15 – Impact ionization rate of electrons and holes for various materials as a function of 1/E. Image reproduced from [13].

As the bias is further decreased, charge carriers gain enough energy to excite multiple pairs per impact, producing a runaway multiplication effect. This phenomenon is called avalanching, page

99 of [13]. Equation 2.34 gives the incremental hole current generated per unit distance by this phenomenon in differential form for both holes and electrons, respectively, pages 37-39 of [14].

$$\frac{dJ_p}{dx} = J_P\alpha_P + J_n\alpha_n \tag{2.34a}$$

$$\frac{dJ_n}{dx} = -J_P\alpha_P - J_n\alpha_n \tag{2.34b}$$

Where:

$$\alpha_n = \frac{1}{nv_n}\frac{dn}{dt} \tag{2.35a}$$

$$\alpha_p = \frac{1}{pv_p}\frac{dp}{dt} \tag{2.35b}$$

These equations can be solved to obtain a more exact solution. However, it is more useful to skip to the solution of interest, the breakdown voltage, Equation 2.36, page 106 [14].

$$V_{BR} = \frac{\varepsilon|E_m|^2}{2qN} \tag{2.36}$$

Where:

$$|E_m| = \frac{E_0}{1 - \frac{1}{3}\log_{10}\left(\frac{N}{N_0}\right)} \tag{2.37}$$

Where N is the smallest of the impurity concentrations of the p and n sides, E_0 and N_0 are experimental parameters and have units of $V/_{cm}$, and N_0 has units of cm^{-3} respectively. When consider these concepts in combination with photocurrent, the topic of the next section, we can form a conceptual map of how to build and optimize semiconductor photodiodes. More exact models of impact ionization and avalanching will be explored in Chapter 3.

2.3.3. Photocurrent in a Diode

In the presence of photons with energies sufficient to excite an electron-hole pairs in germanium, additional current will be available within the diode. In the presence of an internal electric field, drift will be the

primary transport mechanisms of these charge carriers to the respective electrode, and diffusion in the absence of a field. Should carriers survive the transit without recombining, they will module the current flowing through the diode device. This is demonstrated in Figure 2.16. As can be seen, current in this hypothetical device is modulated proportionally to the power irradiated onto the diode, as discussed in Section 2.2.5.

2.3.4. Common Photodiode Architectures

The implications of the previous sections are clear. Semiconductors, due to their unique material properties, can be used to make detectors of electromagnetic energy. Due to the existence of the bandgap, interactions with the photoelectric effect excite charge carriers bound to local atoms into an orbital shared by the entire semiconducting crystal, modulating the conductivity of the crystal. Impurities can be introduced into the material to produce an electric

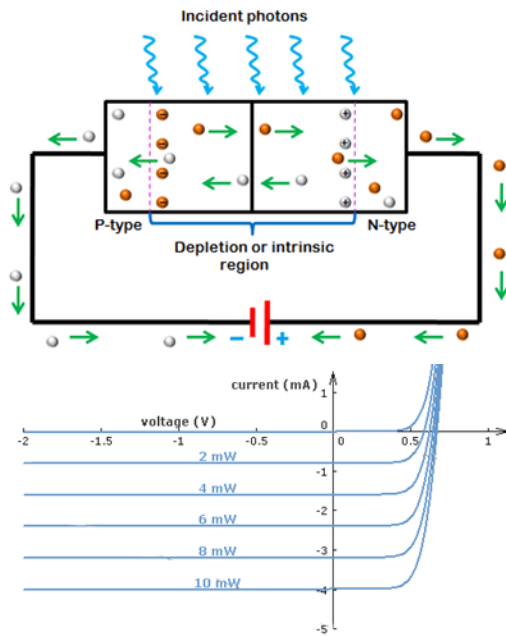

Figure 2.16 – (top) Artistic representation of a diode being illuminated by photons, and (bottom) current vs bias of a diode illuminated by various irradiances. Image reproduced from [13].

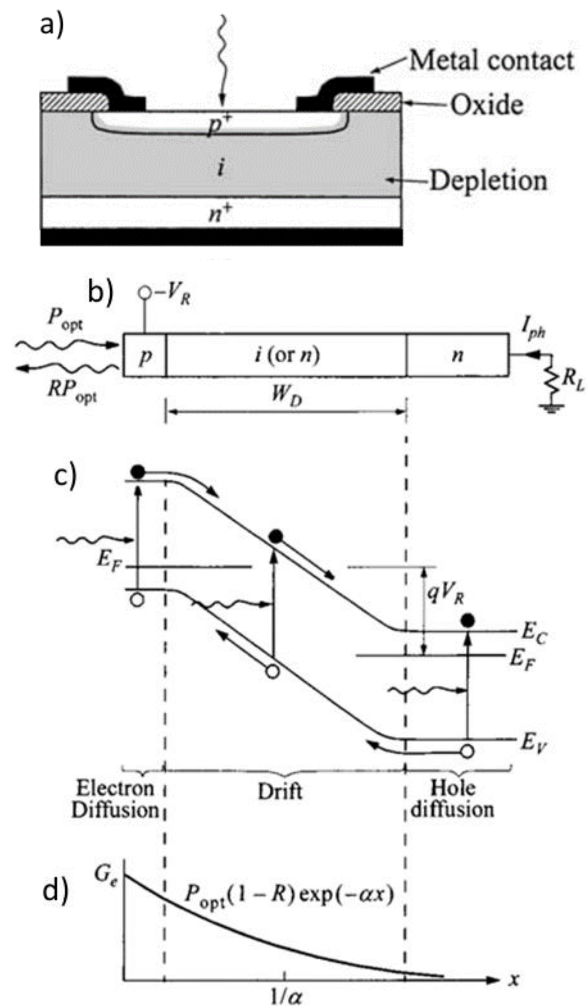

Figure 2.17 – (a) slice view of PiN photodiode, (b) same view from a different perspective, (c) the resulting band bending from the electric field, and (d) the photogeneration rate inside a PiN structure. Image reproduced from [13].

field within the body of the semiconductor, allows us to collect the generated charges with electrodes. Crystal thickness determines the detector's stopping power. As the bias cross the anode and cathode grows larger below 0V, the internal electric field magnitude and width grow within the device. As it is integral to detector design to evacuate every charge carrier produced by a photon quickly, it is highly desirable to have the electric field be at critical field strength everywhere within the photodiode. However, as the field magnitude and width grow impact ionization effects grows, culminating in the avalanching of carriers.

The goal thus is to design a photodiode in which the critical field exists throughout its body for the target thickness, and the breakdown voltage is much smaller to avoid avalanching. Care must also be taken to avoid impact ionization as well by minimizing the applied bias. While a correction factor can be applied to the collected charge to count the photons interacting with the diode, it is better to have a detector in which this is not necessary to reduce uncertainty. Three common photodiode architectures exist for the purpose of x-ray and gamma ray detection: P-i-N photodiodes, metal-semiconductor photodiodes, and avalanche photodiodes. Other photodiode architectures exist, including drift detectors, CMOS imagers, tri-anode structures, buried electrode structures, gated deep trench isolation structures, etc., but are either incompatible with the Daedalus ROIC, are too difficult to fabricate, or reduce temporal performance of the diode, so they will not be considered in this dissertation, 743-782 of [13], 146-149 of [33], [7-9, 36].

2.3.4.1. P-i-N Photodiodes

P-i-N photodiodes have the same structure as PN diodes, with a low-doped intrinsic region in between the two for ease of depletion of a wide area, page 754-760 of [13], page 378-379 of [32]. Figure 2.17 demonstrates this architecture. In this case, the diode is said to be planar due to contacts existing on flat surfaces. However, other geometries have been used historically in nuclear applications, including coaxial and point designs [37, 38]. All three of these designs can be seen in Figure 2.18. Other geometries exist, such as lateral designs, but are generally either used with lower energy photons or have fabrication procedures too complicated to justify and will not be considered in this dissertation.

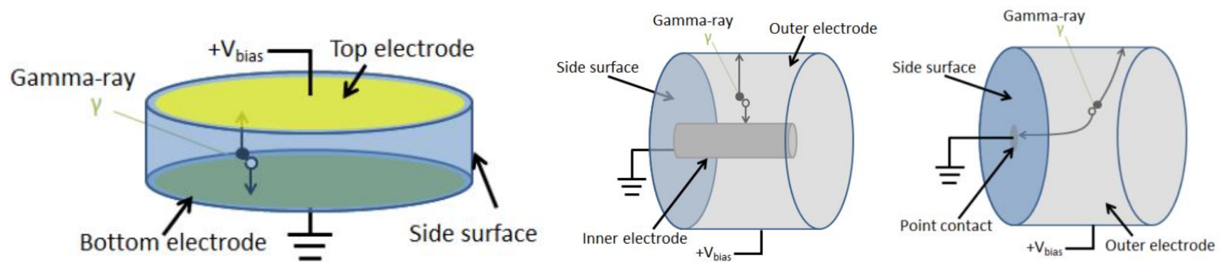

Figure 2.18 – (Left) Planar, (center) coaxial, and (right) point photodiode geometries. Image reproduced from [39].

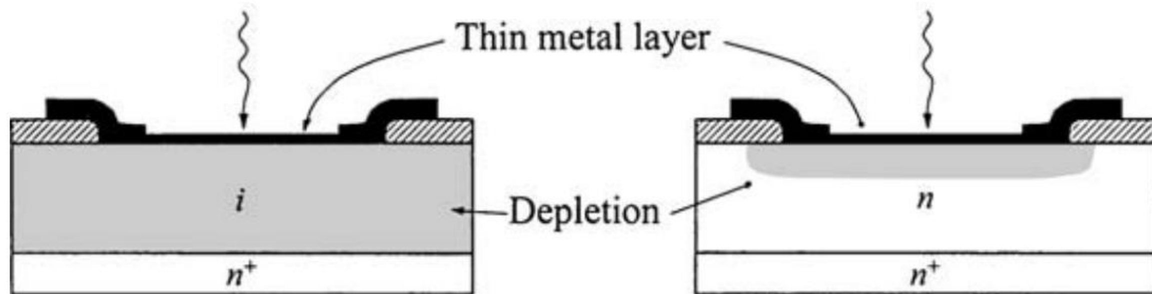

Figure 2.19 – (Left) Metal-i-N photodiode, and (right) metal-semiconductor photodiode. Image reproduced from [13].

Each of these geometries have strengths and weaknesses. Lateral designs are the easiest to fabricate due to the simplest geometry, but have the highest depletion bias out of the three, pages 679 to 682 of [13], [32]. Coaxial are far easier to deplete and have superior temporal response characteristics but are difficult to fabricate due to having to bore into the body of the diode, chemically or mechanically [32]. Point geometries attempt to rectify this by replacing the central electrode with a surface electrode but come at the cost of a higher depletion bias and impact ionization near the cathode, as well as sacrificing the superior temporal response pages 679 to 682 of [13]. Both the coaxial and point geometries are difficult to adapt to an imaging array and are better suited for a bulk detector.

In this dissertation, P-i-N diodes are primarily investigated due to the ease with which these structures can be grown epitaxially on substrate wafers. However, as will be seen in Chapter 3, the coaxial design can be incorporated into the planar design for superior depletion performance.

2.3.4.2. Metal-Semiconductor Photodiodes

Metal-semiconductor photodiodes, also known as Schottky photodiodes, are photodiodes in which the traditional P-layer of a diode is excluded, and the metal comes into direct contact with the N region of the

photodiode, pages 680-682 of [13]. This increases frequency response and decreases switching time of the diode, pages 680-682 of [13]. Schottky diodes come in two forms: metal-semiconductor photodiodes and metal-i-N photodiodes, as seen in Figure 2.19, page 679 of [13]. These diodes, however, have not been tested with the Daedalus ROIC, and are outside the defined scoped of this dissertation.

2.3.4.3. Avalanche Photodiodes

Avalanche photodiodes are operated at high reverse-bias voltages near avalanching to take advantage of current multiplication through impact ionization, page 766-783 [13]. One of the designs considered while designing a photodiode suitable for NIF utilized this effect for signal amplification. However, they can easily saturate the electron well of the Daedalus ROIC [7]. The high photon fluence count will produce washed out images, which have insufficient contrast to discern the inner workings of the hohlraum [7-9]. More importantly, they are not suitable for photon counting applications as the current does not correspond to the number of photons striking the photodiode, yielding poor quantitative data, page 770-772 [13].

2.3.5. A Brief Justification of Germanium

Several other materials are available to manufacture x-ray detectors, a sampling of which can be seen in Table 2.2. Why is germanium a good choice? To answer this question, material properties of several other materials have been investigated. Semiconducting materials with average atom size at least as large as germanium atoms were investigated, but some popular semiconducting materials were chosen as well, such as gallium nitride (GaN). Table 2.2 lists these materials as well as their effective atomic number, density, x-ray linear absorption coefficient at 80 keV, band gap energies, gap type, hole mobilities, and hole saturation velocities. Molecular linear absorption coefficients are calculated with the following Equation 2.38 from [4].

$$\mu = \frac{\rho_{molecule}}{M} \sum_i \left({}^{\mu_\varepsilon}/_{\rho} \right)_i m_i \tag{2.38}$$

Where $\left(\mu_\varepsilon/\rho\right)_i$ is the mass absorption coefficient of the ith atom in the molecular formula, m_i is the total mass of that atom in a molecule in amu, and M is the total molecular mass in amu, and $\rho_{molecule}$ is the molecular density in the material of interest. For example, for PbI_2, at 80 keV [4]:

$$\mu_{80keV} = \frac{7.6\,{}^{g}/_{cm^3}}{207.2 + 2 \cdot 126.9} \cdot \left(7.683\,{}^{cm^2}/_{g} \cdot 207.2 + 3.510\,{}^{cm^2}/_{g} \cdot 2 \cdot 126.9\right) = 33.20\ cm^{-1}$$

This allows for a more useful comparison of the stopping power of the material than a mass attenuation coefficient. While none of these materials will be used in this project, germanium has been selected before this PhD project began, this investigation will yield a deeper insight into what combination of parameters is important when selecting a material for an x-ray detector not immediately obvious from the previous sections. Two of these materials will be looked at in more depth, gallium arsenide (GaAs) and cadmium telluride (CdTe). The rest will be discussed more broadly.

Gallium arsenide is likely the most promising directly competing technology, being currently under active development by Looker et. al. at Sandia National Laboratories [34], designed as a competitor for use in the same reactor, NIF, and are simple mesa P-i-N photodiodes, as seen in Figure 2.20. However, this technology has a maximum thickness of 40µm, which is insufficient to produce the x-ray stopping power necessary for these experiments, as seen in Figure 2.21, page 148 of [40], [4, 34]. Moreover, crystals are

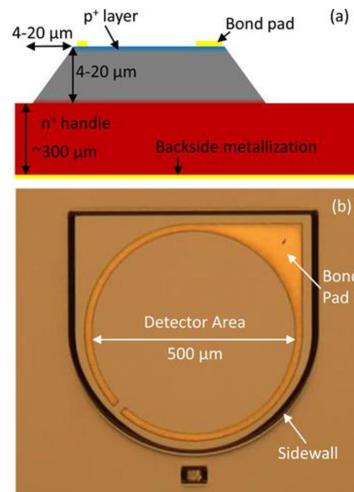

Figure 2.20 – (top) schematic sideview of GaAs diodes and (bottom) photo of a fabricated device [30].

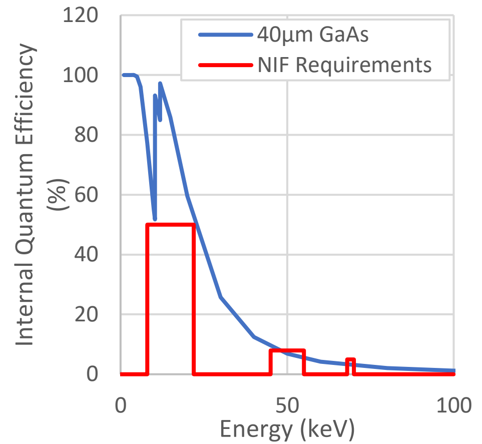

Figure 2.21 – internal quantum efficiency curve for 40µm GaAs. Data from [4].

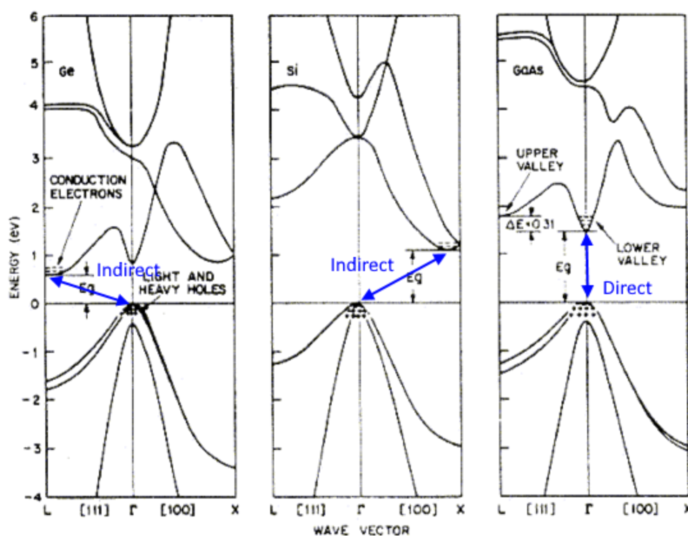

Figure 2.22 – Band structures of (left) germanium, (middle) germanium, and (right) gallium arsenide. Highlighted are indirect and direct bandgaps. Image reproduced from [13].

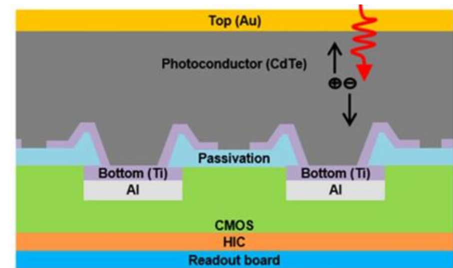

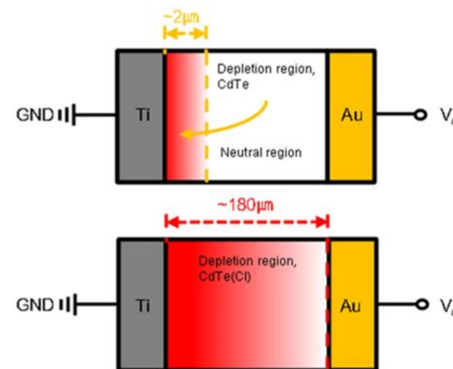

Figure 2.23 – (top) CdTe photodiode cross-section and (bottom) depletion region with and without Cl doping. Reproduced from [68].

Material	Mean Z	Density (g/cm^3)	Linear Atten. Coef. (@80 keV) (cm^{-1})	Band Gap Energy (eV)	Band Gap Type	Hole Mobility (cm^2/V s)	Hole Saturation Velocity (cm/s)
$Bi_2Te_{3(X)}Se_{3(1-x)}$ *	64.4-53.6	7.7-6.82	22.12-13.67	0.15-1.5 [37]	Indirect [41]	240-60.4 [42,43]	–
Cd_3As_2	42	3.03	6.73	X	Dirac Cone [44]	>10000 [45]	$1.5x10^8$ [46,47]
CdS	32	4.82	10.59	2.49 [13]	Direct [13]	40 [13]	–
CdSe	41	5.82	12.05	1.70 [13]	Direct [13]	X	X
CdTe	50	5.85	17.67	1.56 [13]	Direct [13]	100 [13]	$15x10^7$ [48]
GaAs	32	5.32	5.10	1.42 [13]	Direct [13]	400 [13]	$0.7x10^7$ [13]
GaN	19	6.15	4.69	3.44 [13]	Direct [13]	10 [13]	$0.7x10^7$ [49] †
Ge	32	5.323	5.06	0.66 [13]	Indirect [13]	1900 [13]	$0.6x10^7$ [20]
HgTe	66	8.1	31.81	-0.25 [46]	Inverted [50]	10^5 [50]	–
HgI_2	62	6.36	33.20	2.13 [49]	Direct [51]	0.03 [52]	$0.6x10^7$ [53]
InAs	41	5.67	12.27	0.36 [13]	Direct [13]	460 [13]	$0.9x10^7$ [54]
InN	28	6.81	17.28	0.7 [53]	Direct [55]	220 [56]	$2.5x10^7$ [57] †
InP	32	4.81	11.25	1.35 [13]	Direct [13]	150 [13]	$0.7x10^7$ [54]
InSb	50	5.78	17.60	0.17 [5]	Direct [5]	1250 [5]	$7x10^7$ [58] †
InSe	41.5	5.08	11.01	2.4 [59]	Indirect [60]	1000 [61]	–
PbI_2	62.7	6.16	21.95 ††	2.41 [60]	Indirect [62]	1.4 [63]	–
PbS	49	7.6	38.58 ††	0.41 [13]	Indirect [13]	700 [13]	$\sim10^7$ [64]
PbSe	58	8.1	33.95 ††	0.27 [65]	Direct [65]	500 [65]	$\sim10^7$ [64]
PbTe	67	8.16	33.62 ††	0.32 [65]	Direct [65]	2000 [65]	$\sim10^7$ [65]
SnTe	51	6.44	14.24	0.31 [13]	Indirect [13]	4000 [13]	–
ZnTe	41	6.34	15.47	2.26 [66]	Direct [67]	85 [68]	$4x10^7$ [68]
α-Sn	50	5.75	17.42	0.08 [13]	Indirect [13]	–	–

Table 2.2 – material properties relevant to thin film x-ray detectors. Stars (*) indicate that eutectic effects were not investigated. (†) signify reported values are for electrons, which usually is a ballpark approximation for holes. Double daggers (††) signify values reported at 100 keV due to k shell transition at 88 keV in lead. X indicates free holes have not been observed in the material. Dash (–) indicates data not found.

grown with molecular beam epitaxy, which has a low growth rate and throughput, as well as a high defect rate, page 148 of [40]. The high defect rate produces more recombination-generation sites, as discussed earlier in this chapter, reducing the device signal to noise ratio, as well as increasing the internal scattering of the charge carriers. Equally importantly, the band gap of GaAs is a direct band gap in E-k space, as seen in Fig. 2.22, which means the photons emitted from recombination of carriers have the same energy as incident photons. This produces a recursive chain of events in which photons emitted by the material are reabsorbed by the material, a phenomenon known as photon recycling, elongating the temporal response of devices made with this material.

Next, bulk CdTe x-ray detectors are already made by manufacturers such as Ortec, and have superior mass attenuation coefficients, and thus a superior internal quantum efficiency, then that of germanium [4]. The

mobility of hole charge carriers in CdTe is far inferior to that of germanium, 100 $cm^2/_{V \cdot s}$, but hole saturation velocities slightly exceed that of silicon and germanium, peaking at 15x10^7 cm/s at 300K [48, 69]. Using the data found in [4], we can find that to meet NIF requirements we need a thickness of 25µm, further decreasing temporal response. Unfortunately, CdTe films can only be deposited with physical vapor deposition reactors, Chapter 7 of [70], which makes growing PiN structures extremely challenging. Currently, only for Schottky photodiodes to be grown. Depletable Cl-doped CdTe Schottky photodiodes have been produced according to [71], as seen in Figure 2.23. This development is promising, Schottky photodiodes remain incompatible with the common cathode architecture of the Daedalus and Icarus ROICs [7-9].

In general, however, most of these materials will likely make poor x-ray absorption media. Any material with a direct bandgap produces photon recycling effects, as discussed with GaAs, potentially elongating the tail of the current response to a pulse. Any material with a bandgap smaller than germanium will also be difficult to work with due to even higher dark currents, which as will be seen in Chapter 2 is already challenging with germanium. Any material that cannot be easily grown epitaxially over a large area with a low defect density is likewise problematic. Materials with a combination of a low linear attenuation coefficient, crystal purity, mobility, and saturation velocity are also problematic, reducing the external quantum efficiency of the device. Finally, any material with a small minority carrier lifetime is problematic, potentially catastrophic, for signal integrity.

Germanium, while having difficulties, has a direct band gap, eliminating the possibility of photon recycling phenomenon. The band gap energy of germanium, 0.66eV, while difficult to work with, can be managed with intelligent device design. Germanium can be grown with a reasonably low defect rate, albeit with a rather high intrinsic impurity concentration, as will be seen in Chapter 2. Importantly, this impurity concentration does not prevent 60µm thick devices from reaching full depletion of the intrinsic region, again as will be seen in Chapter 2. This combination of parameters makes germanium a good candidate to fabricate imaging arrays.

2.4.3. Competing X-Ray Detection Technologies

Many alternative devices for direct x-ray imaging systems are already in existence, including scintillators, Geiger-Muller detectors, photomultiplier tubes, and their more modern cousins microchannel plates, pages 201-215, 219-247, 265-287 of [32], pages 45-87, 91-133, 281-329 of [72], [73]. The purpose of this section is to justify the development of germanium PiN photodiode arrays amidst other existing technologies for this application. In addition, exploring these works can help in designing photodiodes that meet or exceed the design requirements found in Section 1.3.

Scintillators are commonly used with photodiode arrays in the configuration seen in Figure 2.24 [73]. The strength of the scintillator approach should be obvious: by converting x-ray photons to optical photons the skin depth of the photons is drastically reduced, allowing for far more of the incoming energy to be absorbed by the photodiode. What's more, scintillating materials can be directly bonded to the backside of backside imaging arrays without wires, making them reliable [73]. Barium fluoride is a scintillating material with a sub-nanosecond decay time that might make this technology work in the application at NIF [74]. Scientists at the MaRIE facility are currently working on exactly this technology for ultra-fast astral observations, reporting a temporal response of 1.3ns [75]. They are however limited to 300μm in their pitch size [75], though why exactly this is the case is unclear, since BaF_2 can be deposited with chemical vapor deposition, sputtering, and thermal evaporation [76, 77, 78], making it, at least intuitively, integrable with any process needing a smaller pitch photodiode. The weakness however is the emitted photon statistics: optical photons are emitted in a spherically symmetric radiation pattern, and not necessarily in the direction of the incident x-ray photon, page 21 of [79], [72]. This has a devastating effect on image quality. Moreover, scintillators have a non-linear temporal response to x-rays, page 59 of [72], which when considered in conjunction with the spherical radiation pattern of emitted optical photons, means making an imager across a broad spectrum of x-ray energies difficult.

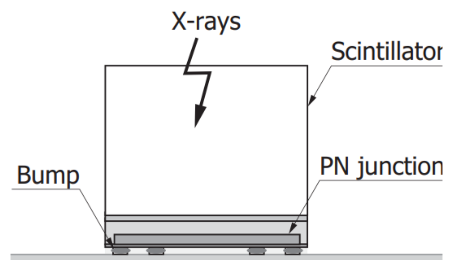

Figure 2.24 – a photodiode bonded to a scintillator, simplified schematic. Reproduced from [73].

Next, Geiger-Muller detectors have neither the spatial nor temporal resolution to support a project such as this, pages 297-302 of [72], 123-178 of [80]. They are moreover gas detectors, which would have insufficient internal quantum efficiency for imaging applications at NIF. Lastly, a careful observation of Paschen's Law they would produce dielectric breakdown of the medium without ionizing radiation if shrunk to the sizes needed for the imaging system, pages 12-14 of [81].

Photomultiplier tubes (PMTs) are sometimes used as x-ray detectors, pages 265-303 of [32]. They however do not have the temporal response necessary for high-speed imaging systems, pages 300-302 of [32]. Microchannel Plates (MCPs) are used in systems such as SLOS at NIF to get ultra-fast (sub nanosecond) temporal responses [82]. However, they only respond to electrons, and require a photocathode material to convert the signal to electrons before interacting with it, which drastically reduces the overall system quantum efficiency pages 294-295 of [72]. Spatial resolution with these kinds of systems can be difficult to manage due to scalloping and other field force interactions in the resultant electron plasma, pages 11-37of [83]. Moreover, they are an amplification tool, and still need an imaging array for form an image, and so they only encourage this project, not compete against it. The germanium photodiode array is planned on being implemented into many of the instruments found in [82], such as the SLOS instrument.

Chapter 3 – Device Simulation and Design

PiN structures were grown epitaxially with atmospheric pressure chemical vapor deposition (APCVD) on highly doped N-type germanium wafers to various thicknesses by the Lawrence Semiconductor Research Laboratory (LSRL). Due to the relative novelty of the process, epitaxial growth of germanium is both expensive to perform and has a high degree of impurity concentrations in the intrinsic region, as demonstrated by Fig. 2.1. The order of simulations is made clear by this result, then. First, establish a simulation model that matches current characteristics of real devices. Second, determine what minimum intrinsic impurity concentration must be achieved for working devices to be realizable, and whether this is theoretically possible. Third, using the final impurity concentration achieved during epitaxial growth, design a pixel using the established model that meets operating requirements.

3.1. Silvaco Model Setup

Before we begin simulating devices care must be taken to find models that accurately fit material properties. Several parameters are important are important to model, and can be categorized into mobility, velocity saturation, generation-recombination, tunneling effects, dopant properties, and metal contacts, page 50 of [84].

3.1.1. Mobility

Perhaps the most important parameter to model correctly when modeling semiconductor devices is mobility. It influences current, carrier evacuation times, and the breakdown voltage of the device being designed. Recall from Chapter 2 that Matthiessen's rule states:

$$\frac{1}{\mu} = \frac{1}{\mu_{lattice}} + \frac{1}{\mu_{impurities}} + \cdots \qquad (2.10)$$

Thus, modeling mobility consists of modeling each contribution to mobility. In the case of germanium, three dominate: acoustic phonon scattering, impurity scattering, and surface roughness scattering, page 28 of [13]. Acoustic phonon scattering can be modeled with the standard mobility model found on page 28 of [13], Equation 3.1:

Material	Carrier	μ_{max} (cm^2 V^{-1} s^{-1})	α
Silicon	Electron	1417	2.5
	Hole	470.5	2.2
Germanium	Electron	3900	2.5
	Hole	1900	2.2

Table 3.1 – parameters of Equation 3.1. Data from [13].

$$\mu_{phonon} = \mu_{max}\left(\frac{T}{300K}\right)^{-\alpha} \tag{3.1}$$

Where μ_{max} is the maximum possible mobility in the material, T is the material temperature, and α is a fitting parameter. Table 3.1 lists the parameters for germanium and silicon. The recommended model to use for impurity scattering in simulations was proposed by Masetti et. al, Equation 3.2, page 51 of [84], [85, 86, 87].

$$\mu_{dop} = \mu_{min,1} exp\left(-\frac{P_C}{N_A + N_D}\right) + \frac{\mu_{const} - \mu_{min,2}}{1 + \left(\frac{N_A + N_D}{C_r}\right)^{\alpha}} - \frac{\mu_1}{1 + \left(\frac{C_s}{N_A + N_D}\right)^{\alpha}} \tag{3.2}$$

Where N_A and N_D are impurity concentrations and μ_{const} is bulk mobility. All other parameters are fitting parameters. Table 3.2 lists these parameters for silicon and germanium. This model is well suited for any

Material	Carrier	μ_{min1} (cm^2 V^{-1} s^{-1})	μ_{min1} (cm^2 V^{-1} s^{-1})	μ_{min1} (cm^2 V^{-1} s^{-1})	P_C (cm^{-3})	C_r (cm^{-3})	C_s (cm^{-3})	α	β
Silicon	Electron	52.2	52.2	43.4	0	9.68×10^{16}	3.34×10^{20}	0.68	2.0
	Hole	44.9	0.0	29	9.23×10^{16}	2.23×10^{17}	6.10×10^{20}	0.719	2.0
Germanium	Electron	60	0	20	10^{17}	8×10^{16}	3.43×10^{20}	0.55	2.0
	Hole	60	0	40	9.23×10^{16}	2×10^{17}	10^{20}	0.55	2.0

Table 3.2 –Masetti model parameters for silicon and germanium. Data from [84]

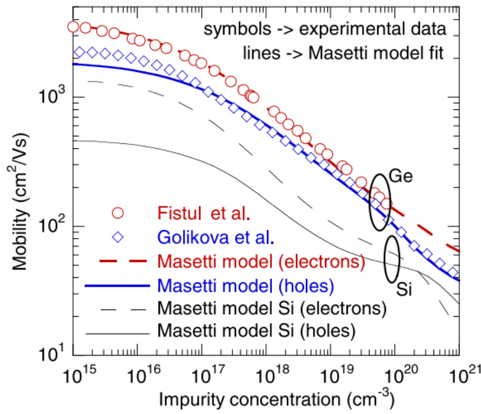

Figure 3.1 – modeling and data of mobility vs impurity concentration. Reproduced from [84].

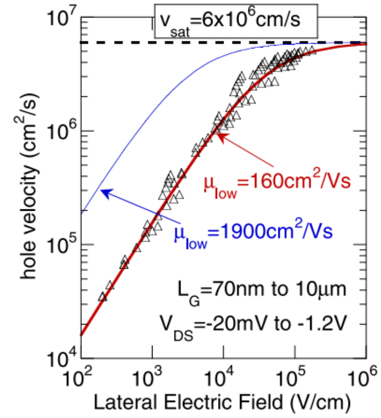

Figure 3.2 – velocity vs tangential electric field strength for holes. Demonstrates model predictions with μ_{low} set to 1900 and 160 cm^2/Vs. Reproduced from [84].

semiconductor with an indirect bandgap, such as silicon and germanium. Doping-dependent mobility was measured for electrons by Fistul et al [85] and for holes by Golikova et al [86], and the parameters found there were used to empirically fit the Masetti model for germanium [87], as seen in Figure 3.1.

Surface roughness scattering is modeled by the Enhanced Lombardi Model, but is more applicable to MOS device simulations where there is a strong transverse electric field present and was thus omitted in this study, page 52 [84].

3.1.2. Saturation Velocity

Saturation velocity is an important parameter to consider because it is desirable for carriers generated by photons to be travelling at or near this

Material	**Carrier**	v_{sat} ***(cm/s)***	μ_{low} **(cm^2 V^{-1} s^{-1})**	β
Silicon	Electron	1.1×10^7	1375	2
	Hole	8.4×10^6	487	1
Germanium	Electron	8×10^6	730	2
	Hole	6×10^6	160	1

Table 3.3 – Caughey-Thomas expression parameters. Data from [84, 88].

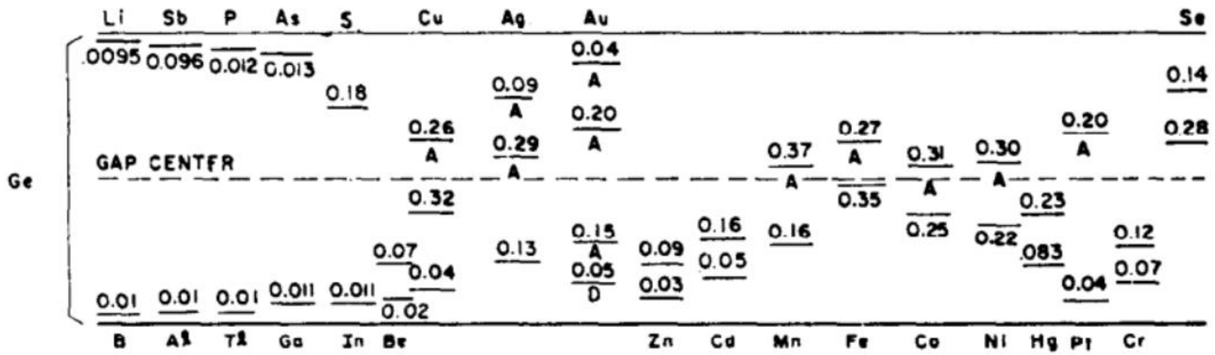

Figure 3.3 – Impurity ionization levels of important impurities for germanium. Distance from top bar to demarked line is the ionization energy for donors, and distance from bottom bar to demarked line is ionization energy for acceptors. Reproduced from [13].

velocity. Having an accurate model is essential in determining how much of the generated carriers will be evacuated, and how many will recombine within the photodiode. The Caughey-Thomas expression, Equation 3.3, is used to calculate the velocity of a charge carrier experiencing an electric field, page 52 of [84], [88].

Dopant	Type	Ionization Energy (eV)
Sb	Donor	0.0096
P	Donor	0.012
B	Acceptor	0.01

Table 3.4 – Dopants used in simulations and their ionization energies in Germanium. Data from [13].

$$v(E) = \frac{\mu_{low} E}{\left[1 + \left(\frac{\mu_{low} E}{v_{sat}}\right)^{\beta}\right]^{\frac{1}{\beta}}} \tag{3.3}$$

Where v_{sat} is the saturation velocity, E is the electric field the carrier is experiencing, and μ_{low} and β are fitting parameters. Table 3.3 displays these parameters for silicon and germanium. Figure 3.2 shows the measured and fitted and modeled hole velocities as a function of the electric field strength.

3.1.3. Electrically Active Impurities

Electrically active impurities are modeled by inputting the dopant ionization energies in the device for the material. All that is needed for this is Figure 2.6, reproduced in Figure 3.3. Because of the non-trivial impurity concentration of arsenic in the intrinsic region, it is imperative that the correct value for its ionization energy be used. Table 3.4 lists the impurities and their ionization energies used in the model.

3.1.4. Generation-Recombination

As discussed in Chapter 2, the primary source of recombination and generation effects in germanium is SRH statistics, defect induced generation and recombination. This model is important when modeling signal integrity in the photodiode. In practice, this is modeled with a fitted SHR curve, Equation 3.4, page 53 of [84], [89].

$$\tau_{SRH} = \tau_{min} + \frac{\tau_{min} + \tau_{max}}{1 + \left(\frac{N_A + N_D}{N_{ref}}\right)^{\gamma}} \tag{3.4}$$

Where τ_{max} is the maximum SHR lifetime, and τ_{min}, N_{ref}, and γ are fitting parameters. Table 3.5 lists these parameters for silicon and germanium.

3.1.5. Tunneling Effects

There are two tunneling effects in germanium that play an important role in device simulations: trap assisted tunneling and band to band tunneling [84]. Band-to-band tunneling (BTBT) occurs in large electric fields where the gap between valence and conduction bands becomes small, and the probably of tunneling becomes non-trivial [84, 90]. Trap-assisted tunneling (TAT) occurs under moderately large electric fields where the valence and conduction bands are bent, page 54 of [84, 91]. The gap between then is large enough for a direct band to band tunneling probability to be small, and a carrier tunnels through defect. In large electric fields the minority carrier

Material	*A (cm s^{-1} V^{-2})*	***B*** **($eV^{-3/2}$ V cm^{-1})**
Silicon	8.977×10^{20}	2.147×10^{7}
Germanium	8.977×10^{20}	1.6×10^{7}

Table 3.7 – BTBT parameters for germanium and silicon. Data from [84].

Material	Carrier	m_t
Silicon	Electron	0.5
	Hole	0.5
Germanium	Electron	0.12
	Hole	0.34

Table 3.6 – TAT parameters for germanium and silicon. Data from [84].

Material	Carrier	τ_{min} (s)	τ_{max} (s)	N_{ref} (cm^{-3})	γ	T_{α}	T_{coeff}	E_{trap} (eV)
Silicon	Electron	0	1×10^{-5}	10^{16}	1	-1.5	2.55	0
	Hole	0	3×10^{-6}	10^{16}	1	-1.5	2.55	0
Germanium	Electron	0	4×10^{-5}	10^{14}	0.85	-1.5	2.55	0
	Hole	0	4×10^{-5}	10^{14}	0.85	-1.5	2.55	0

Table 3.5 – SHR model parameters for silicon and germanium. Data from [84].

concentration is decreased, and junction leakage are increased [84, 90, 91]. Thus, these models were included.

The TAT model was first introduced by Hurkx et al. and describes a reduced carrier lifetime [91]. The TAT model can be seen in Equation 3.5. The BTBT model was first introduced by Schenk in [90] and describes the generation/recombination rate as a function of the ratio between the local electric field and the critical field F_C. The BTBT model is complex, and the whole model will not be reproduced in this work. A key piece of it can be seen in Equation 3.6 [84, 90].

$$\tau_{TAT} = \frac{\tau_{SHR}}{1 + \Gamma_{TAT}} \tag{3.5}$$

$$F_C{}^{\pm} = B_{BTBT}\left(E_{g,eff} \pm \hbar\omega\right)^{3/2} \tag{3.6}$$

Where Γ_{TAT} is the trap-assisted tunneling factor. TAT parameters for germanium and silicon can be seen in Table 3.6. BTBT parameters for germanium and silicon can be seen in Table 3.7. $E_{g,eff} = E_c(\Delta_l) - E_B(\Gamma_{25})$ depends on the crystal orientation and is calculated automatically by the simulator.

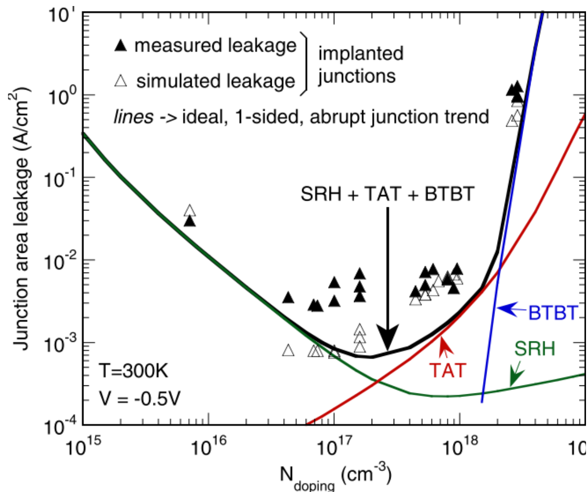

Figure 3.4 – An interplay between the SHR, TAT, and BTBT models as a function of doping. Reproduced from [82].

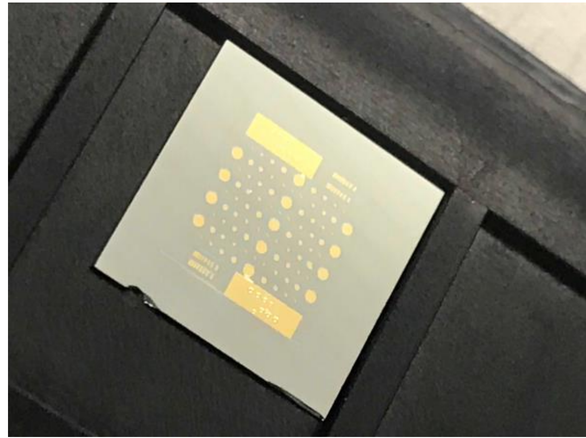

Figure 3.5 – Germanium devices, (left) fabricated and (right) simulated.

3.1.6. Generation-Recombination – The Complete Model

Because TAT and BTBT affect carrier lifetimes and generation-recombination rates, they, along with SHR statistics, form a much more complete leakage current and carrier lifetime model. Figure 3.4 demonstrates the relationship between all three models as a function of doping.

3.1.7. Defect Analysis

As discussed in Chapter 2, defects play an important role in carrier lifetimes in the body and surface of the semiconductor detector. As will be seen in Chapter 4, the poor surface oxide quality of germanium produces a high defect density and must be mitigated. However, defect density is highly dependent on the passivation method of the device and cannot be known a priori. Because the metrics of interest mostly occur in the body of the germanium, the modeling of this phenomenon was omitted. In addition, authoritative defect analysis on modern epitaxial germanium from LSRL does not yet exist, making obtaining this value difficult.

3.1.8. Metal Contact Properties

As will be discussed in Chapter 4, germanium exhibits a strong Fermi pinning at the surface, producing rectifying contacts on the cathode unless treated properly [92, 93, 94]. While implementing this parameter

was attempted in Silvaco Atlas, the simulations consistently did not converge, so this parameter was omitted.

3.2. Comparison between Simulated and Fabricated Devices

Once a model is assembled, it is imperative that it is tested against fabricated devices to test for accuracy. For this, devices were fabricated in the LLNL cleanroom and current characteristics were measured in UC Davis. Figure 3.5 shows the devices fabricated for this experiment. Figure 3.6 shows the IV characteristics of both the fabricated and the simulated devices. As can be seen in Figure 3.6, excellent agreement exists between the fabricated and simulated devices, even with defect density and metal contact modeling neglected.

3.3. Wafer Development Simulations

PiN structures were grown epitaxially on substrate germanium wafers at LSRL. However, due to how young the technology is, initial wafers produced this way had a relatively high arsenic concentration in the intrinsic region, as seen in Figure 3.7. The first question that needs to be answered is at what intrinsic region impurity concentration does the device breakdown voltage exceed the depletion bias for a 60μm planar photodetector? After that, at what bias does the internal electric field reach the critical field throughout the device? A fully depleted device with a critical field throughout the intrinsic region is necessary for high-speed device fabrication. If devices reach avalanching before the critical field is reached everywhere in the device, or if the critical field bias is close to the breakdown voltage and incoming photons trigger avalanching, high-speed operations cannot be achieved at low power, causing the photodiode to not meet required specifications. The goal of these simulations was to provide an impurity profile to strive for in the epitaxial deposition process.

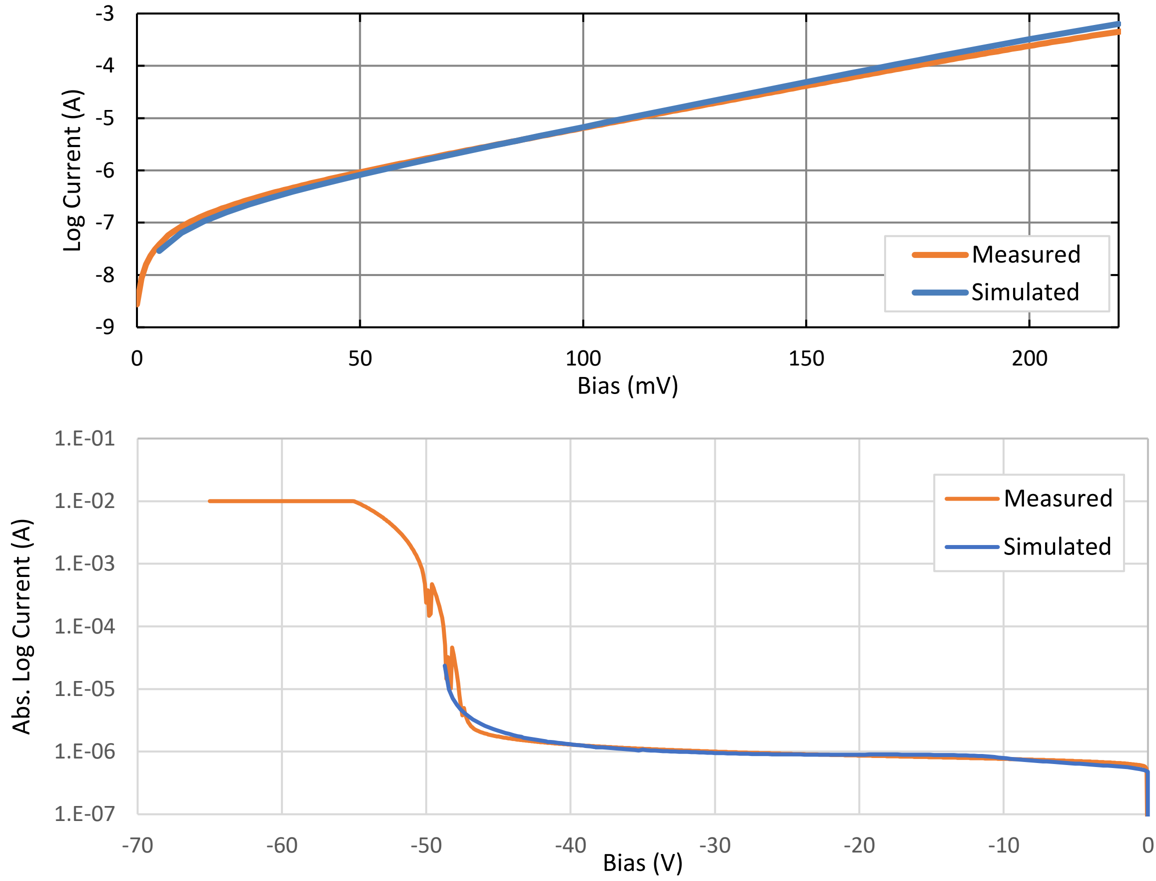

Figure 3.6 – Comparison of (top) IV characteristics and (bottom) reverse IV characteristics of real and simulated germanium diodes.

Recall from Equation 2.33 that the depletion width is a function of the intrinsic region doping, provided the anode doping is at least an order of magnitude larger.

$$W_D(V) = \sqrt{\frac{2\varepsilon}{qN_D}(V_i - V)} \tag{3.7}$$

Solving for the voltage, we obtain Equation 3.8.

$$V = V_i - \frac{qN_D}{2\varepsilon}{W_D}^2 \approx -\frac{qN_D}{2\varepsilon}{W_D}^2 \tag{3.8}$$

Thus, the only parameter of interest in this simulation is the intrinsic region doping. One would simply have to find a doping low enough to achieve a bias in which the critical field exists within the entire intrinsic region.

3.3.1. **Internal Electric Field Simulations**

To answer this question, the model established in Section 2.1 was used, and the SRP profile was modulated with Silvaco automation tools constructed in the Python programming language. Using the SRP profile was used instead of a uniform value as minor variations in the doping profile will modulate the depletion bias slightly. Internal electric field magnitudes along the center cutline were extracted and the results were used to guide process development. Figure 3.8 shows these internal electric fields of various impurity concentrations as well as reverse current characteristics at 25C. Using this process, it was determined that the impurity concentration

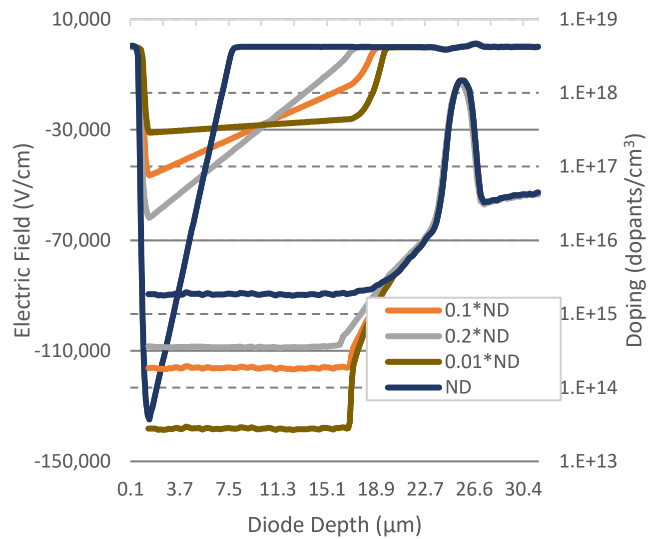

Figure 3.8 – Simulations of nominal doping of first generation of epitaxial wafers. Simulations show internal electric fields at the breakdown voltage as a function of various percentages of nominal doping.

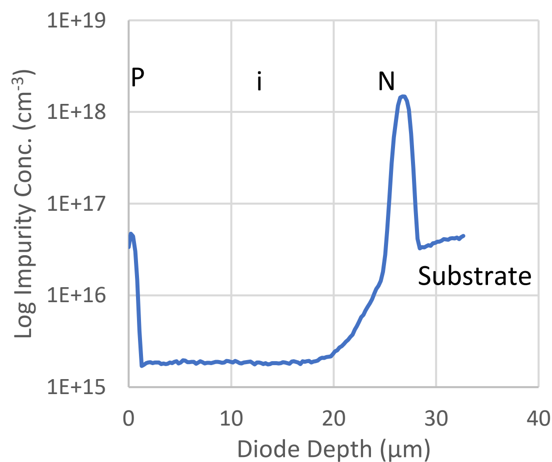

Figure 3.7 – First generation wafer SRP measurement result for a 20µm intrinsic region.

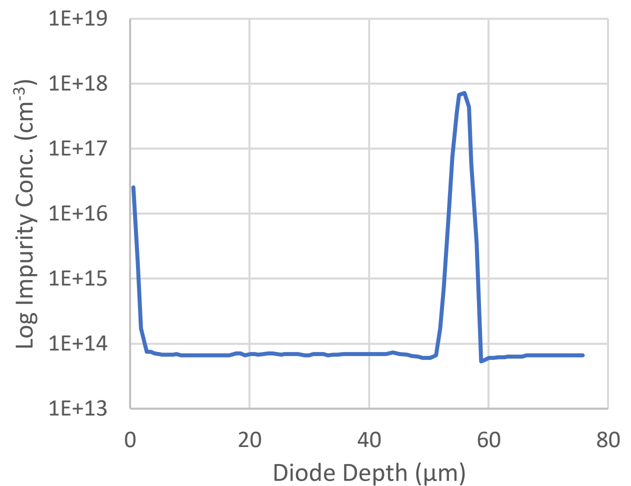

Figure 3.9 – SRP data of year 3 epitaxial structures.

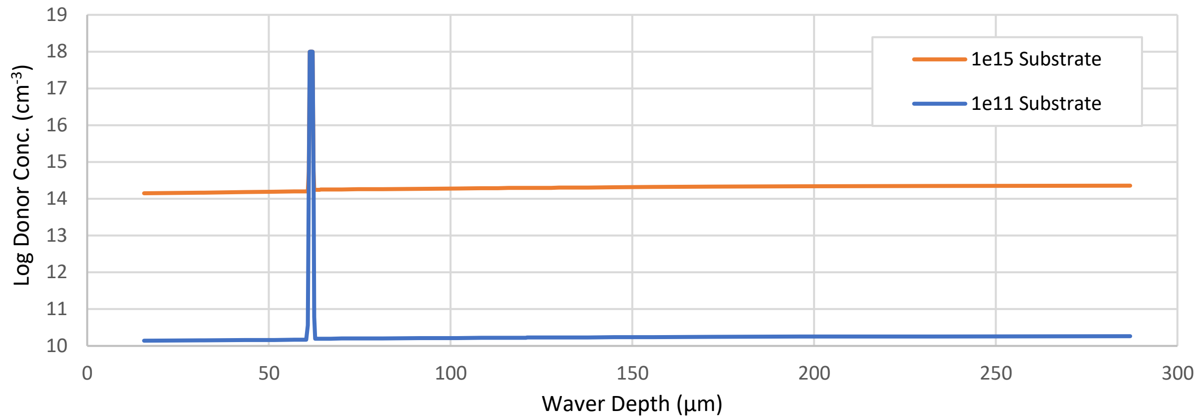

Figure 3.10 – Epitaxial wafer growth simulations with a 10^{15} antimony concentration substrate and 10^{11} antimonty concentration substrate. Antimony floods PiN intrinsic layer due to high diffusivity in germanium.

could not exceed 8x10^{14} $atoms/_{cm^3}$. These simulations provided a roadmap for wafer development.

Using doping compensation techniques, a silicon nitride back seal to keep the process chamber cleaner, as well as methods to clean up germanium tetrachloride delivery system, the impurity concentration reached a concentration of 2 x 10^{15} $atoms/_{cm^3}$ for the second round of wafer growth, and finally concentration of 1 x 10^{14} $atoms/_{cm^3}$ for the final round of wafer growth, as seen in Figure 3.9.

3.3.2. Epitaxial Process Simulation

Once the third round of epitaxial wafer production was completed, it was not immediately obvious as to why the impurity concentration could not be reduced further. Because reduction of the intrinsic impurity concentration is the most direct method for depletion bias reduction, a critical question remained: what was impeding the reduction of the intrinsic region impurity concentration reduction, and could the obstacle be eliminated? As can be seen in Equation 3.7, the interest to further reduce the intrinsic region impurity is strong, it further reduces the depletion bias of the devices. To answer this question, Silvaco Victory Process was used to grow epitaxial germanium on a germanium seed wafer.

The process was simulated thus: the wafer first is heated to +750C in five minutes, and 30µm of intrinsic germanium is deposited over the course of an hour. Following this, the germanium wafer is cooled to +300C in five minutes, kept in a nitrogen environment for six minutes at a constant temperature. This is

the step at which cleaning of the chamber occurs in the real process. Then the wafer is reheated to +750C in five minutes, and 30μm of additional intrinsic germanium is deposited onto the wafer. The wafer is then allowed to cool to room temperature.

The state of the chamber was neglected for this simulation. Only processes internal to the wafer were analyzed. This was done twice: once with a wafer impurity concentration of $10^{15}\ {atoms}/{cm^3}$ and once with $1 \times 10^{11}\ {atoms}/{cm^3}$. As can be seen in Fig. 3.10, due to the high diffusivity of antimony in germanium at +750C, an intrinsic impurity concentration lower than the substrate impurity concentration is not feasible. Thus, one of three courses must be undertaken: a high purity germanium wafer must be used as a substrate, the process must be redeveloped with a lower temperature, or an intermediate layer that both allows for epitaxial growth of germanium and negate the diffusion of antimony into the epitaxial layer. None of these methods test for external conditions, however, such as chemical and chamber purity. Unfortunately, funding did not permit for additional studies in intrinsic impurity reduction. However, since this study will continue by this author at LLNL after this dissertation, these findings are still relevant.

3.3.3. Heterojunctions

Heterojunctions are material interfaces in which two different semiconducting materials or different semiconducting alloys are adjacent to one another in a device. This produces an interface in which the band gap of the two materials is not equal, and if the device is designed correctly, can reduce dark current of the photodiode, pages 122-123 of [13]. Heterojunctions come in four types, straddling, staggered, and broken

gap heterojunctions, and barrier structures, pages 124-129 of [14, 95]. The first three incorporate bulk materials to implement the heterojunctions, pages 124-129 of [13], and are seen in Figure 3.11, the last uses a GeSi superlattice [95], that is, alternating layers of 10nm or less of germanium and Ge_XSi_{1-X} to block SHR current, seen in Table 3.8.

Early in wafer development, heterojunctions were attempted to be incorporated. Incorporating them resulted in too much strain for the wafers to be useful, as seen in Figure 3.12. Nevertheless, heterojunctions were explored. There are several types that could be tested: heterojunction anode,

Structure	Flatband Diagram	Adjusted Flatband Diagram
XB_nn (aka n Barrier)	Anode, Cathode	Not Applicable
XB_pp (aka p Barrier)	Anode, Cathode	Same as unadjusted
Dual Band	Anode, Cathode	Anode, Cathode
Complementary Barrier	Anode, Cathode	Cathode, Anode

Table 3.8 – barrier structures reported in literature and their adjusted forms for photodiodes.

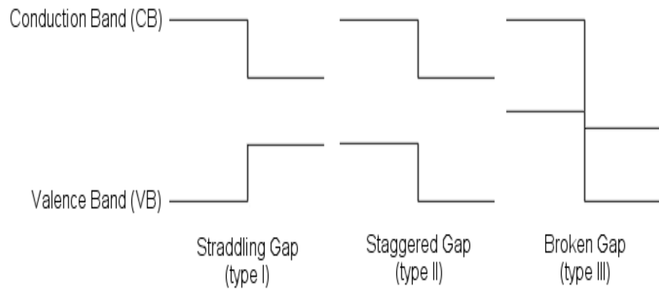

Figure 3.11 – Epitaxial wafer growth with a heterojunction anode resulted in significant internal strain and deformation of germanium wafers.

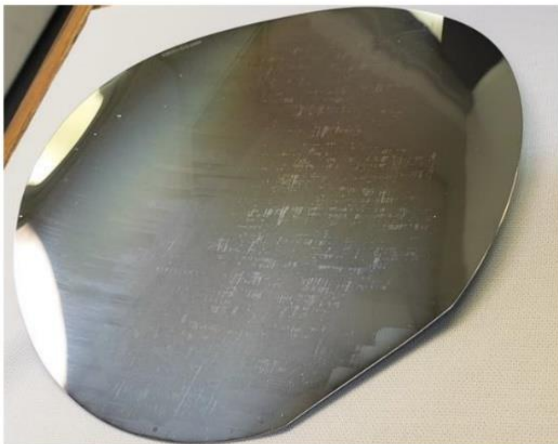

Figure 3.12 – Epitaxial wafer growth with a heterojunction anode resulted in significant internal strain and deformation of germanium wafers.

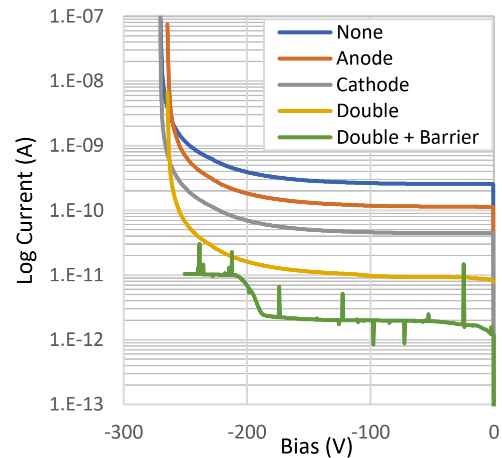

Figure 3.13 – Dark current as a function of bias with various $Ge_{0.9}Si_{0.1}$ heterojunction structures. Having a double heterojunction in combination with a p barrier structure drastically decreases the device dark current.

heterojunction cathode, and superlattice barrier structures. A single 25μmx25μm pixel was modeled in Silvaco Atlas with $Ge_{0.9}Si_{0.1}$ heterojunctions incorporated various combinations at 300K. As can be seen in Fig. 3.13 and Table 3.9, dark current could be diminished from by over an order of magnitude.

To find a solution to the strain problem, the epitaxial growth simulation model from the previous section was used for testing two methods for reducing strain: using the strain relaxation inherent to superlattice structures known to exist with certain materials and by modulating the wafer size. This remains an area of active research.

3.4. Device Simulations

Once a final impurity profile has been measured, the search for a device structure in which carrier velocity is fully saturated begins. In this dissertation, three photodiodes will be studied: a standard planar PiN photodiode as a reference, a gaussian planar superjunction, and a deep pit photodiode, and a superjunction and deep pit hybrid structured. Figure 3.14 displays graphical representations of the devices discussed in this section.

Devices in Sections 3.4.1 to 3.4.4 were simulated without the substrate or the epitaxial germanium surrounding the pixel structure. This has the effect of reducing the dark current. This produces simulated I-V curves that are not comparable to measured I-V curves of real devices. This was done for computational efficiency and to minimize convergence issues present with larger meshes. However this still produces a benchmark that real devices can be compared against once they are fabricated.

HTJ Structure	**Current Density at -225V (A/cm^2)**	**Current Per Pixel at -225V (A)**	**Projected Array Current at -225V (A)**
None	9.06e-5	5.66e-10	2.97e-4
Anode	4.67e-5	2.92e-10	1.53e-4
Cathode	1.66e-5	1.04e-10	5.45e-5
Double	4.32e-6	2.70e-11	1.42e-5
Barrier	6.70e-6	4.19e-11	2.19e-5
Double + Barrier	2.98e-7	1.86e-12	9.75e-7

Table 3.9 – Figure 3.13 tabulated and projected to a full array.

3.4.1. Planar Photodiode

The first photodiode structure is an obvious one: a planar photodiode. Simple in design and effective in operations, the current Daedalus imaging array consists of an array of planar silicon photodiodes. They are simple to fabricate and have very well understood properties. Figure 3.15 demonstrates the photodiode structure used for the simulation. Figure 3.16 demonstrates the internal electric field strength of a PiN photodiode, both two dimensions and the center axis of the structure. Figure 3.17 demonstrates their carrier concentrations, showing they are indeed fully depleted. Because final device is to be backlit, the x-ray beam origin has been placed to aim at the cathode, perpendicular to diode layers, as seen in Figure 3.18a. Figure 3.18b demonstrates x-ray penetration depth of various energies into the diode. Figure 3.18c demonstrates x-ray irradiance on the photodiode surface. One nanosecond pulse widths and evacuation times are dictated by NIF experiment timing requirements [1, 81]. Figure 3.19 demonstrates x-ray response when biased to saturation velocity. There are four parameters of interest: rise time, fall time, and the full width at half max (FWHM), and the charge evacuation time. Together these parameters specify how well the photodiode evacuates charge from the intrinsic region. It is critical that all charge generated by an x-ray pulse be evacuated from the photodiode body before the next x-ray beam hits the photodiode.

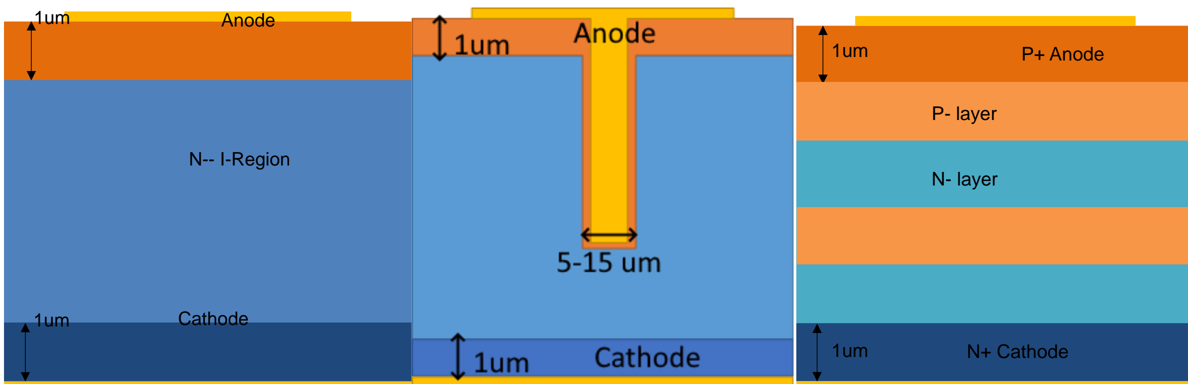

Figure 3.14 – (left) planar photodiode, (middle) deep pit photodiode, and (right) planar superjunction photodiode.

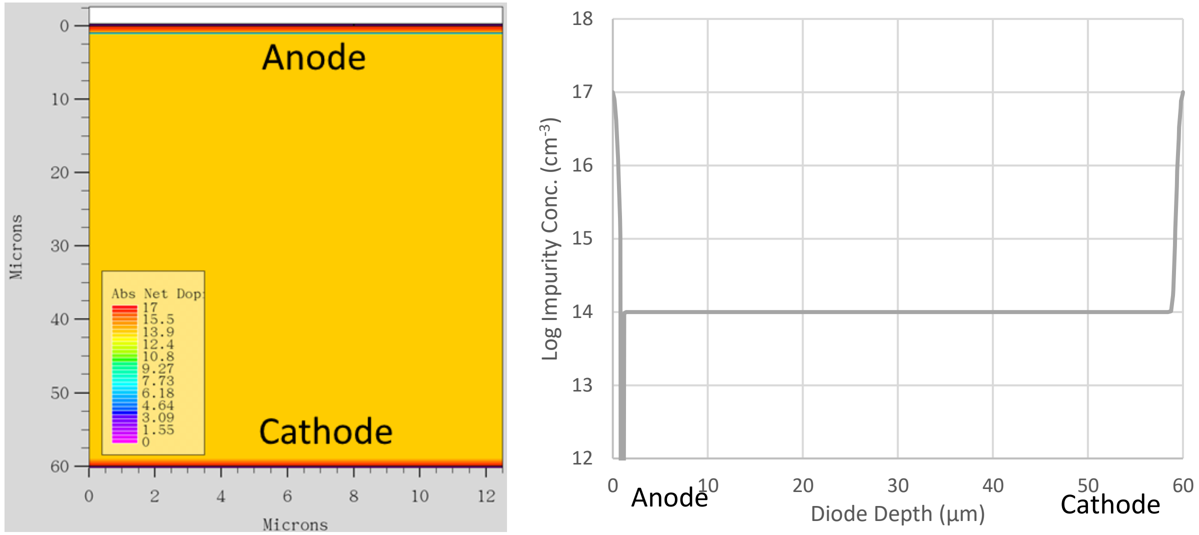

Figure 3.15 – (left) cross-section of planar PiN photodiode, and (right) doping along center cutline.

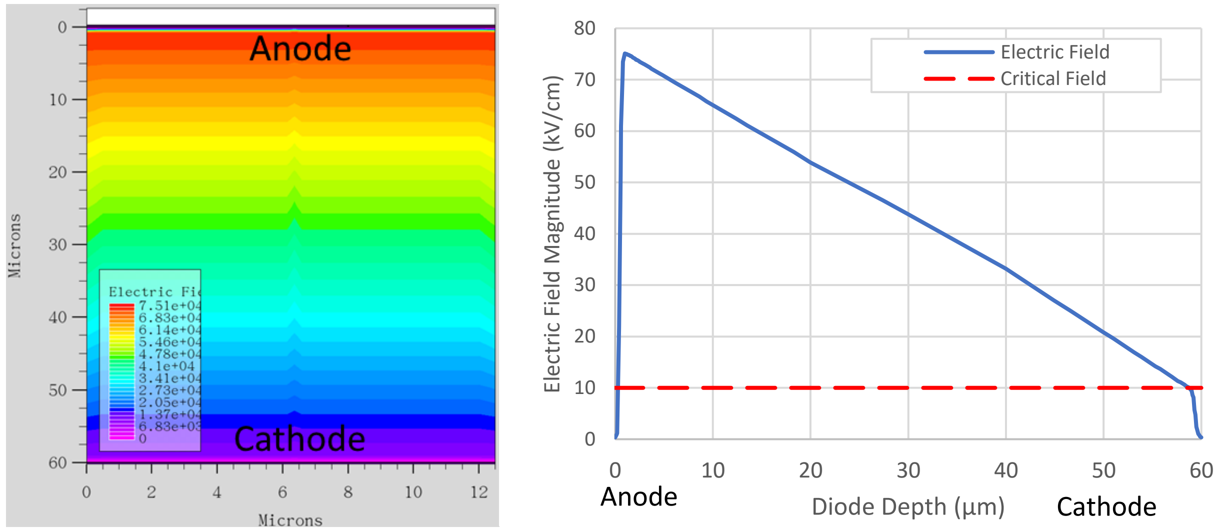

Figure 3.16 – (left) electric field magnitude in cross-section of planar PiN photodiode, and (right) electric field magnitude along center cutline.

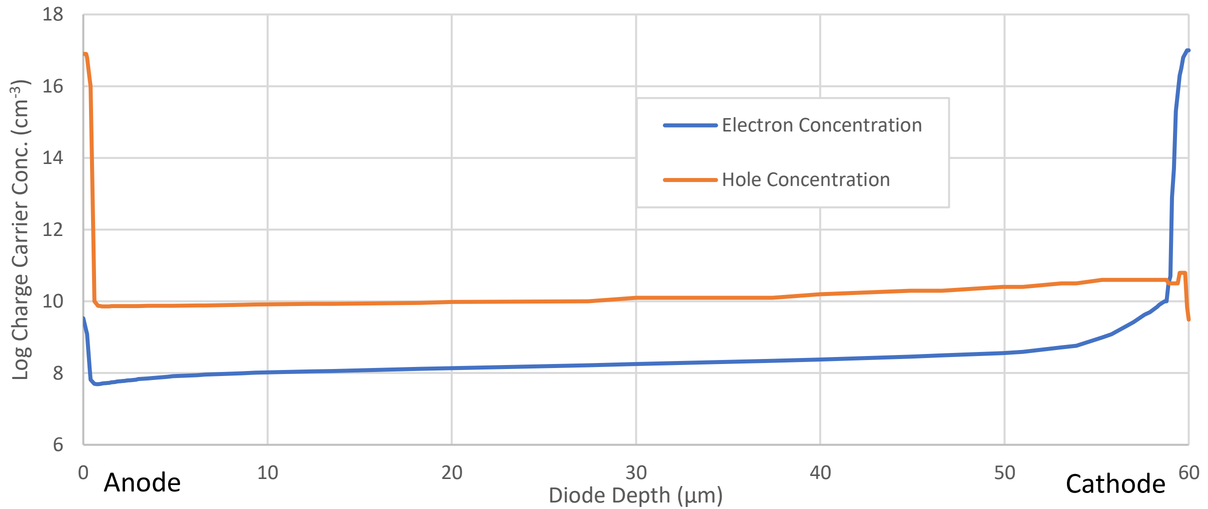

Figure 3.17 – hole and electron concentration along center cutline. $10^9 < n_i$, indicating depletion within the intrinsic region of the diode.

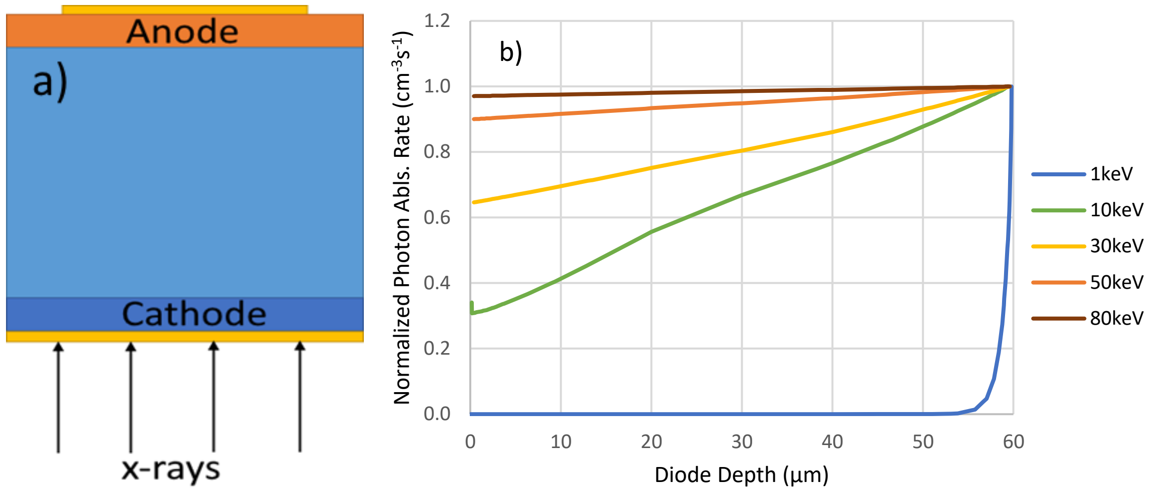

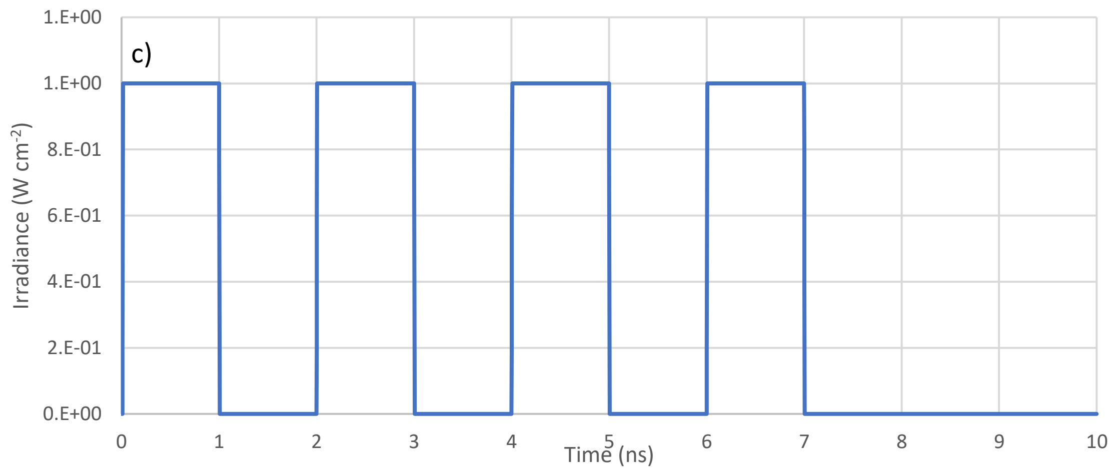

Figure 3.18 – (a) Orientation of x-rays, (b) simulated x-ray penetration depth using NIST mass-attenuation coefficients of germanium, and (c) normalized x-ray irradiance on photodiode surface.

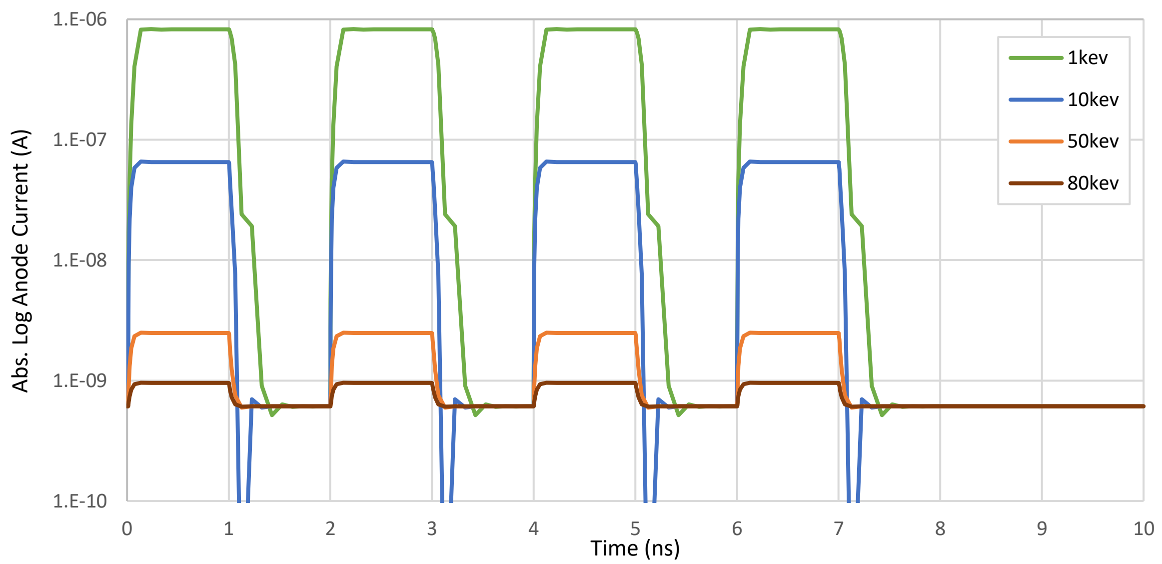

Figure 3.19 – X-ray photodiode response. Charge evacuation is predicted to be sub nanosecond, which is well in line with NIF experiment. Dark current was subtracted from measurement for ease of comparison.

3.4.2. Superjunction Photodiode

3.4.2.1. Simulation Results

By the suggestion of literature [96- 98], superjunction photodiodes were applied to the PiN structure, seen in Figure 3.21. It was found that they significantly lower the photodiode depletion voltage, as seen in Figure 3.23. However, the vertical trenches make the structures time consuming and expensive to manufacture epitaxially. LSRL does not have photolithography or DRIE capabilities, making the fabrication a multi-laboratory process. So, the lightly doped n- and p- regions seen in Figure 3.21a were flipped to be parallel with the p+ and n+ regions, as seen in Figure 3.21b. To reduce layer interface scattering, the periodic structure was modified to a sinusoidal-like doping pattern, as seen in Fig. 3.22. This structure consists of overlapping gaussian impurity concentrations to produce a quasi-sinusoidal structure with more gradual n- and p- junctions and has been named the gaussian planar superjunction (GPSJ) photodiode. Depletion bias simulations were run and were found to strongly be a function of the number of layers within the photodiodes, as seen in Figure 3.23. As can be seen, depletion biases can be reduced by an order of magnitude when compared to a standard PiN.

Figure 3.24a demonstrates the internal electric field strength of GPSJ photodiodes with a variety of layers, biased to depletion (not saturation velocity). Figure 3.24b demonstrates the internal electric fields of the diodes used in this study, biased to saturation velocity everywhere within the photodiodes. The six-layered diode was biased to -90V, eight-layer to -85V, and ten-layer to -80V. Figure 3.25 demonstrates their carrier concentrations, showing they are indeed fully depleted. Figure 3.26 demonstrates x-ray response when biased to saturation velocity. As can be seen, currents and response times are within tolerances, but tradeoffs exist with the number of layers and temporal response. This is due to an increase in capacitance within the photodiode structure as the number of layers increase. It has been found that by modulating the width of the P- layers impact ionization can be reduced, as can be seen in Figure 3.27. As seen in Figure 3.28, with proper p- region width modulation, no impact ionization occurs within the intrinsic region when eight or more layers are used when devices are biased to saturation velocity. The strength of this device is

that it can be grown with the current high temperature epitaxial process, allowing gains in performances without additional research and development in the epitaxial growth of germanium process, as will be seen later in this chapter.

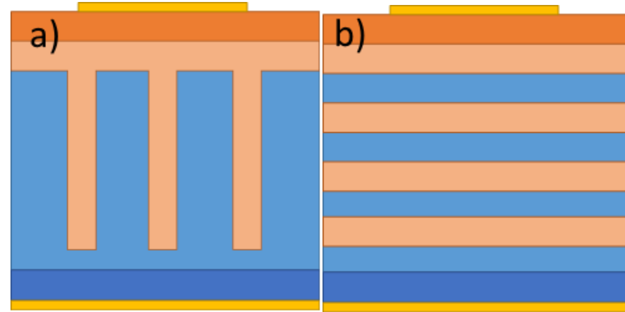

Figure 3.21 – (a) vertical superjunction photodiode, and (b) planar superjunction photodiode.

3.4.3. Pitted Anode Devices

Superjunction devices, although exceedingly promising, have the disadvantage of a higher production complexity, and thus a higher production cost. Fabrication of this design is anticipated in the near future. As an alternative, deep trench and deep pit structures were investigated. Although pitted anode designs exist in literature for this diode structure [99, 100, 101], the structure seen in Figure 3.29 has been developed to fit the unique imaging requirements of NIF.

The larger the pits, the easier to deplete the structure. The smaller the pits, the easier they are to fabricate. Figure 3.30 shows structure simulated in Silvaco. Figure 3.31 shows the electric field as both a vector map and along the center cutline of a 30µm pit depth when the diode is biased at -150V. X-ray response can be seen in Figure 3.32, and a comparison with PiN response can be seen in Figure 3.33. Unfortunately, this comes at the cost of an increased impact ionization along the area between the pit and the cathode, as seen in Figure 3.34.

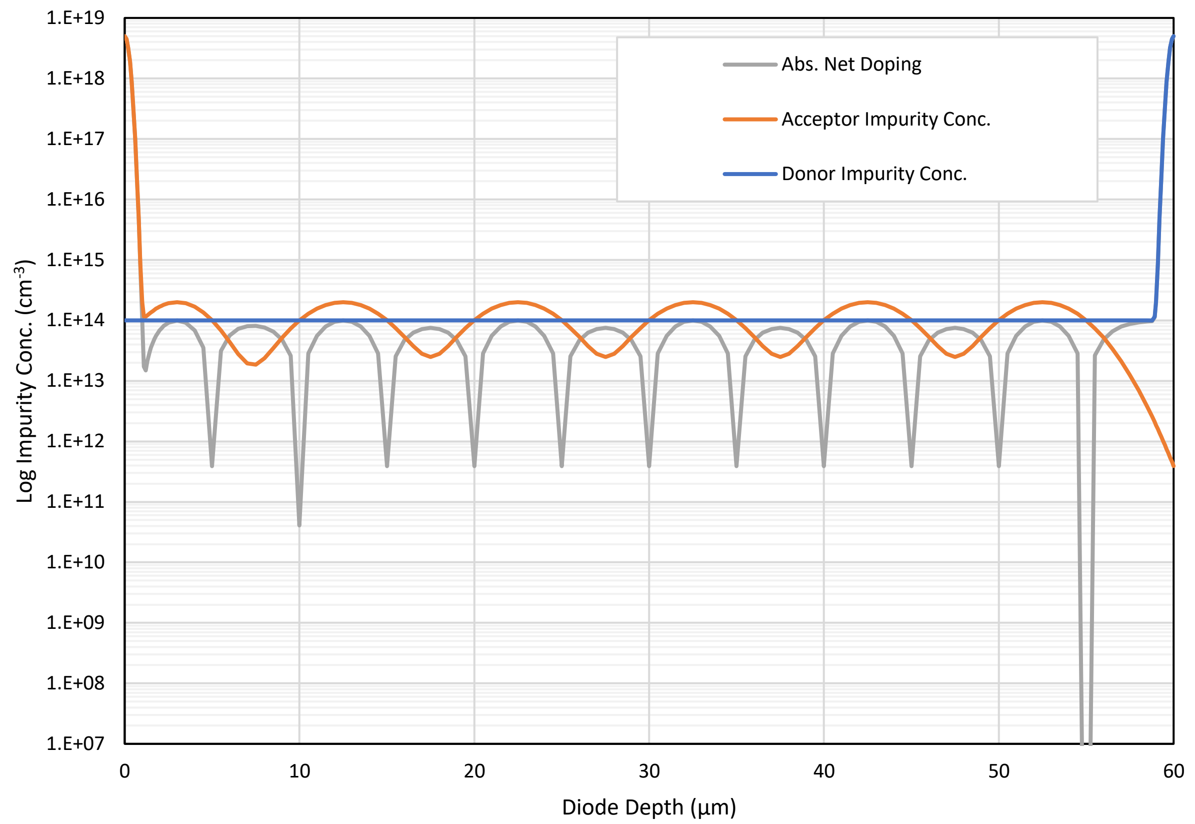

Figure 3.22 – doping structure of a twelve-layer GPSJ photodiode.

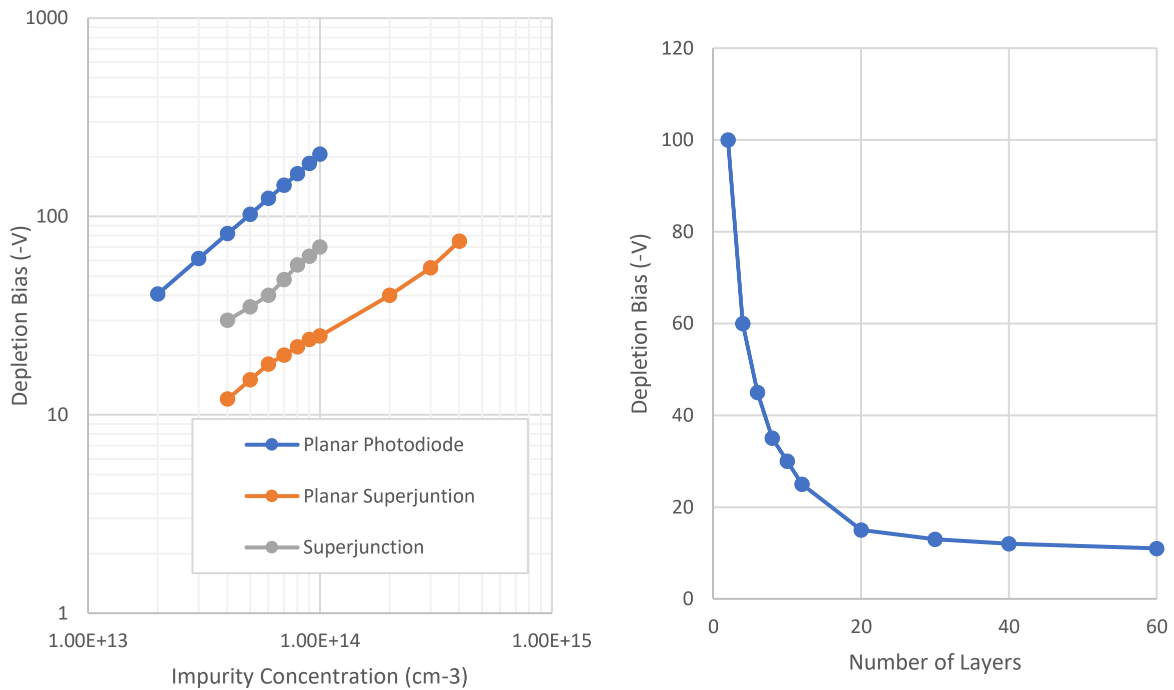

Figure 3.23 – (left) depletion biases of a planar PiN, a vertical superjunction, and a twelve-layer lateral superjunction at various impurity conenctrations, and (right) depletion bias of a 1e14 impurity concentration intrinsic region as a function of the number of layers.

a)

Electric Field Magnitude (kV/cm)

2 Layers
4 Layers
6 Layers
8 Layers
10 Layers
12 Layers
20 Layers

Diode Depth (μm)

b)

Electric Field Magnitude (kV cm^{-1})

6 Layers
8 Layers
10 Layers
Critical Field

Diode Depth (μm)

Figure 3.24 – Internal electric field of gaussian planar superjunction devices of varying number of layers biased to (a) depletion and (b) to velocity saturation. Intrinsic impurity concentration was fixed at 10^{14} cm^{-3}.

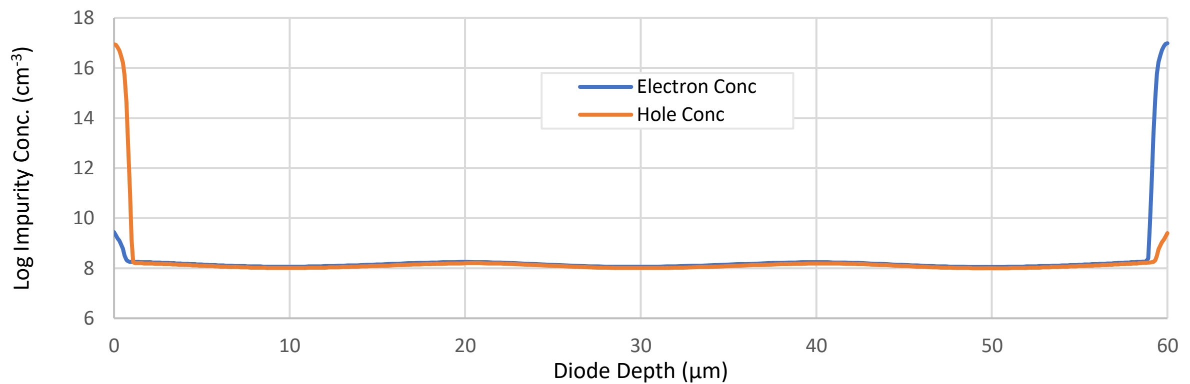

Figure 3.25 – Electron and hole concentrations for six-layer devices.

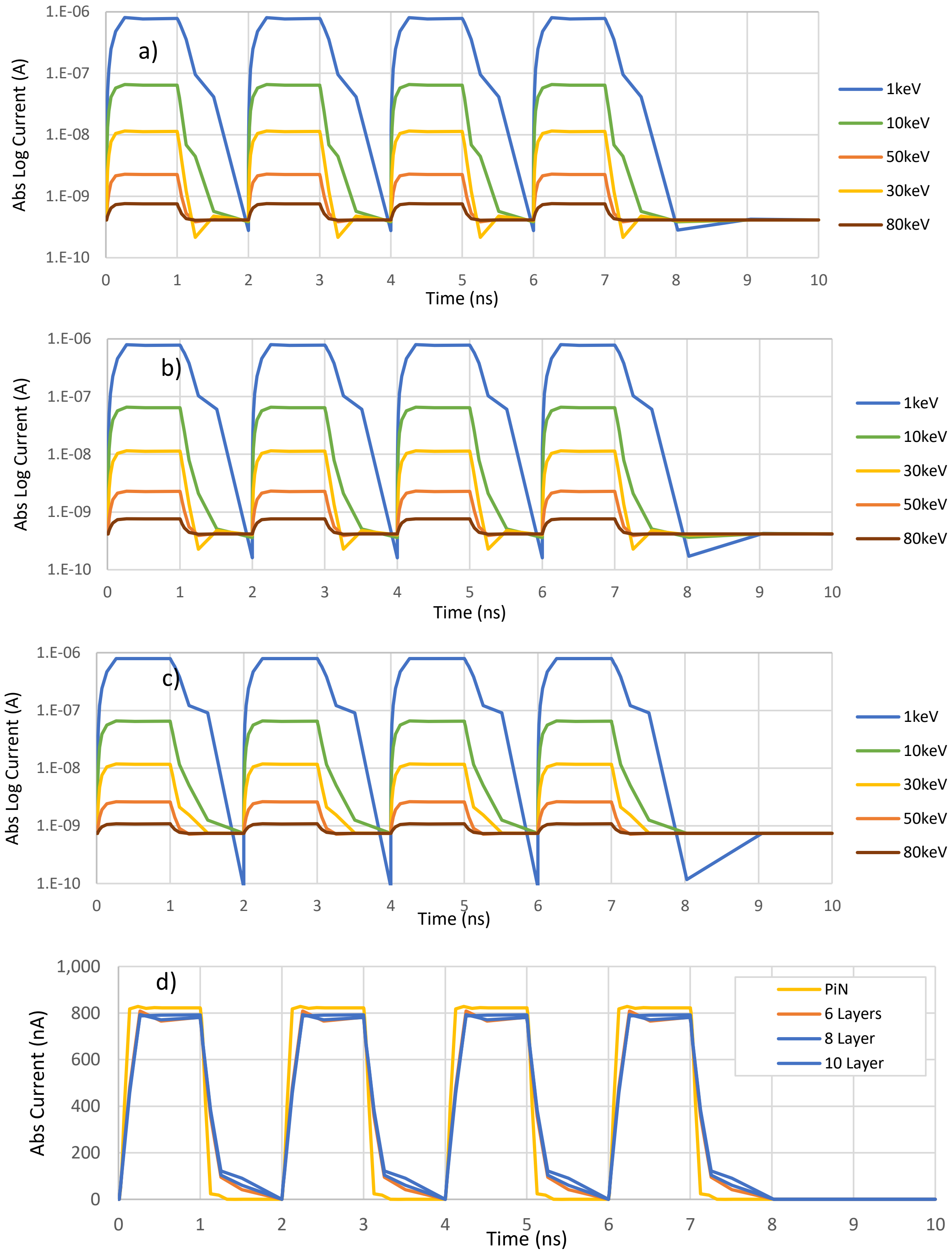

Figure 3.26 – X-ray response of GPSJ photodiodes to various x-rays, including (a) 6-layer devices, (b) 8-layer devices, and (c) 10-layer devices. (d) Characteristic signs of capacitance increase can be seen in the 1keV currents of 1keV x-rays as the number of layers increases as compared with the PiN.

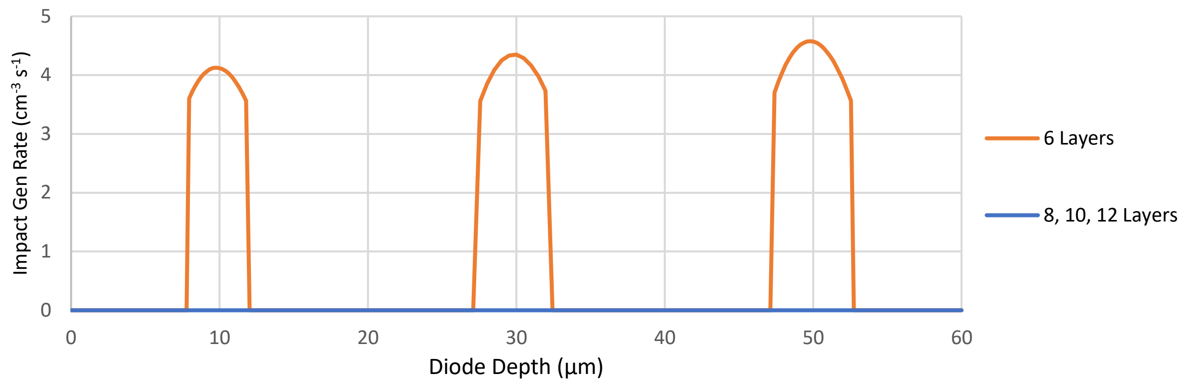

Figure 3.27 – Impact ionization rate of GPSJ photodiodes biased to the critical field everywhere within the photodiode.

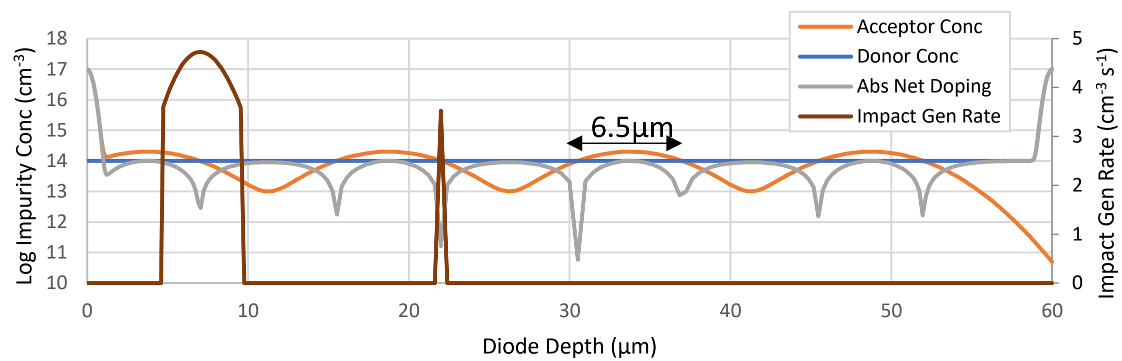

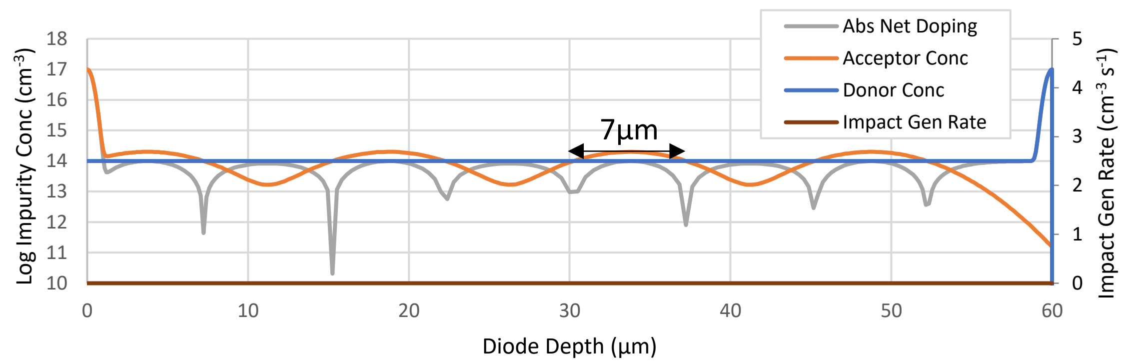

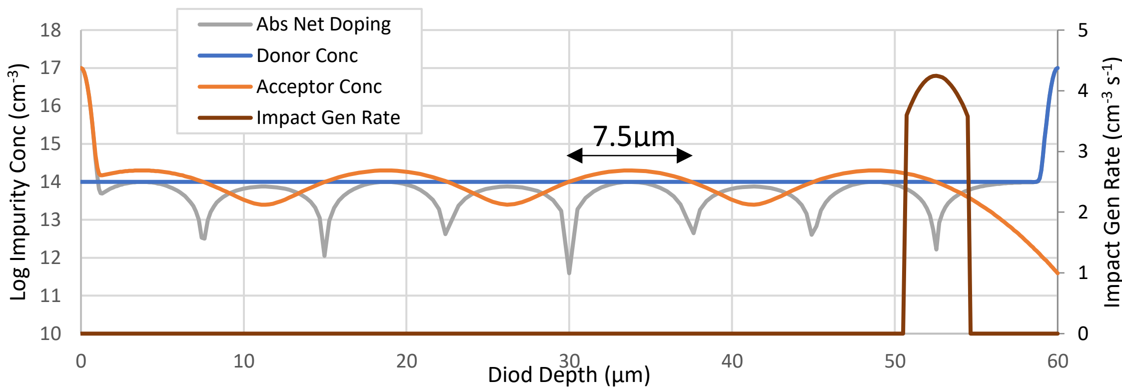

Figure 3.28 –Impact ionization for eight-layered GPSJ photodiode with (a) 6.5µm junction to junction distance, (b) 7µm junction to junction distance, and (c) 7.5µm junction to junction distance.

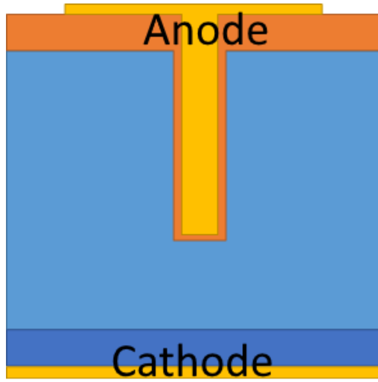

Figure 3.29 – Deep pit photodiode structure developed for NIF.

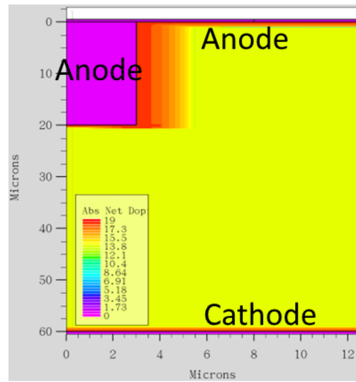

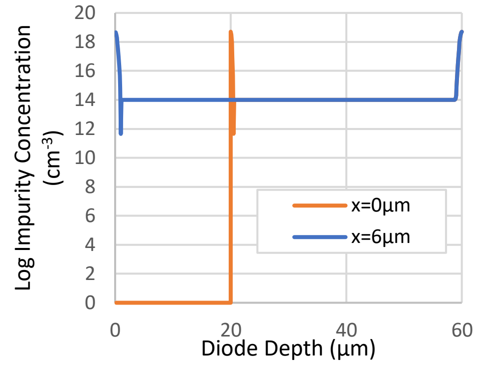

Figure 3.30 – (left) planar view of simulated structure doping, and (right) doping along the center cutline (x=0µm) and 6µm from the center.

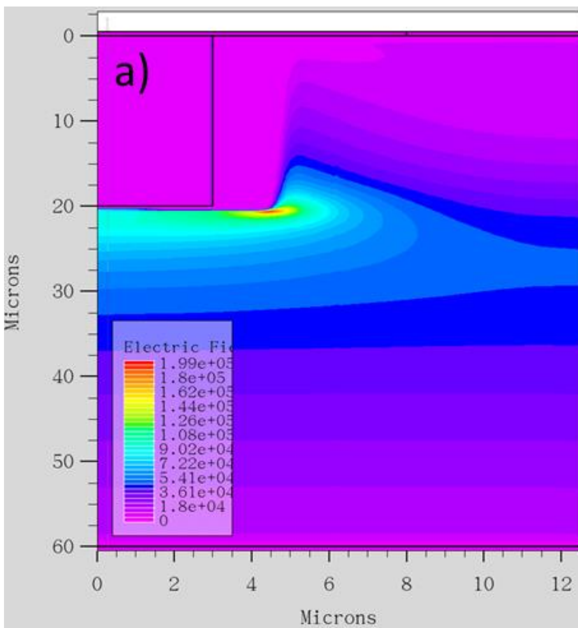

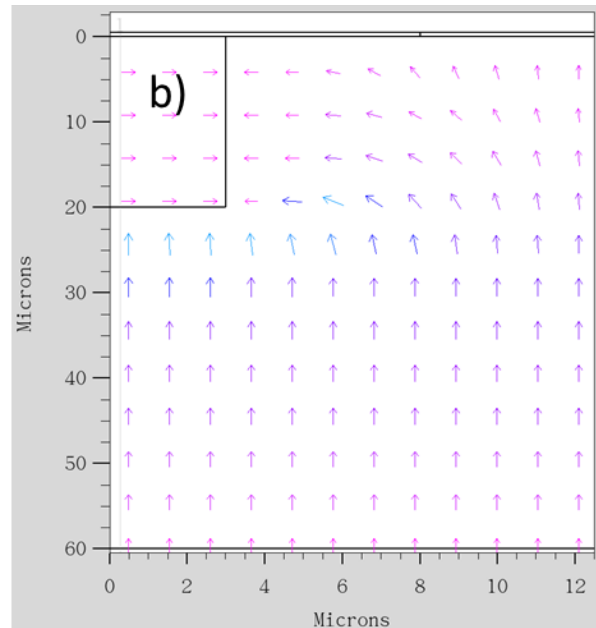

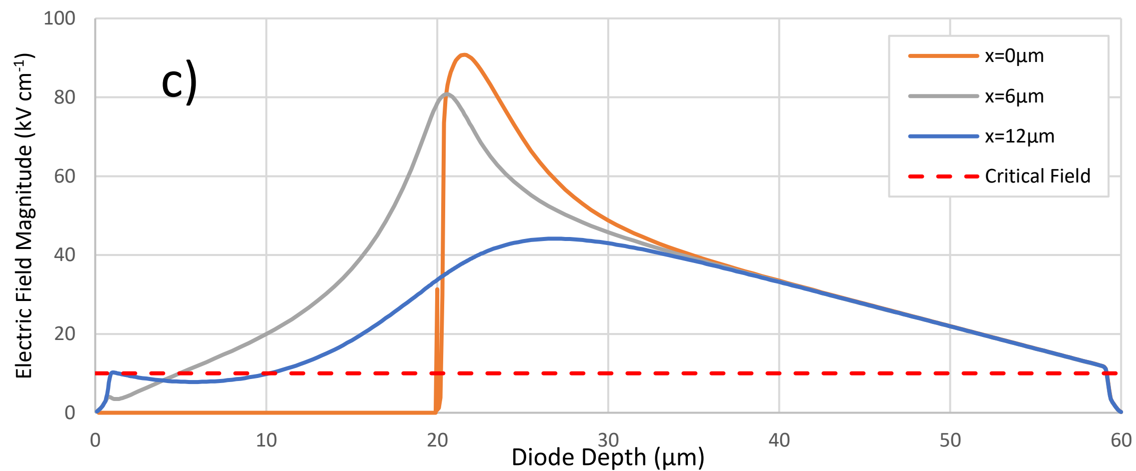

Figure 3.31 – (a) planar view of electric field magnitude, (b) vector view of electric field, and (c) electric field across multiple cutlines.

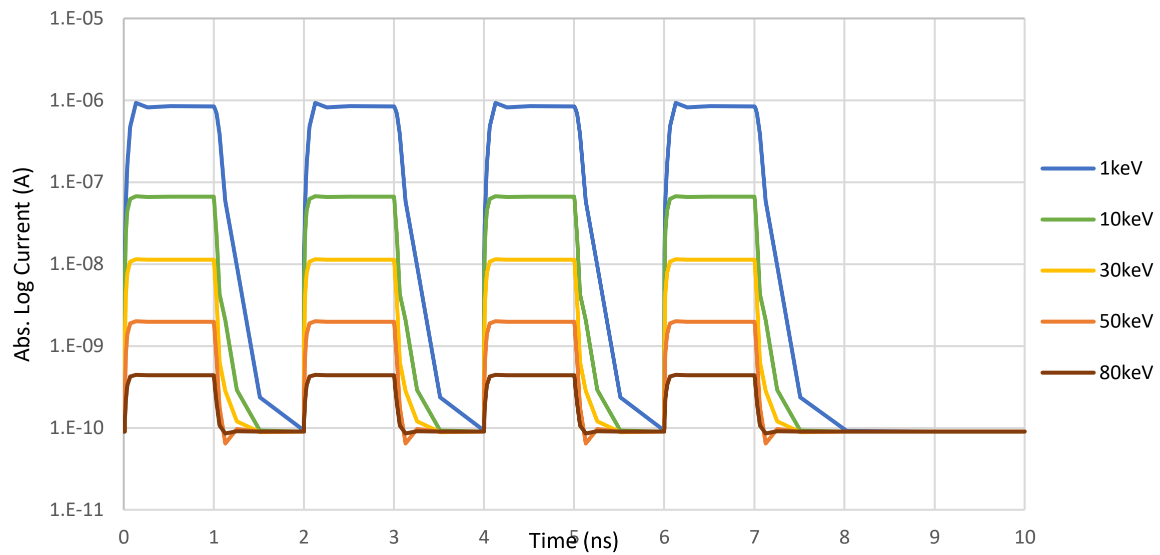

Figure 3.32 – Photodiode response to x-ray pulses.

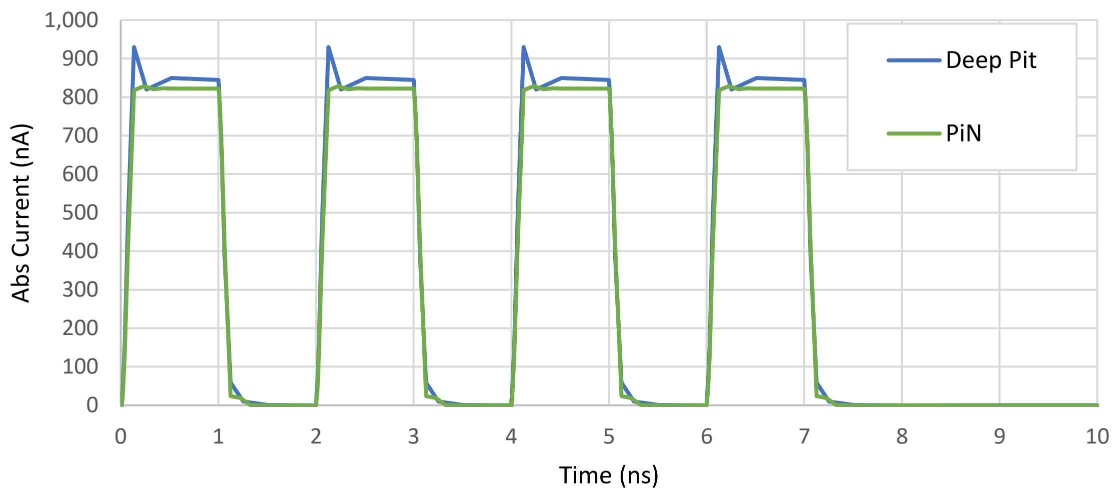

Figure 3.33 – Photodiode response comparison of PiN and Deep Pit structures. Device speeds are comparable.

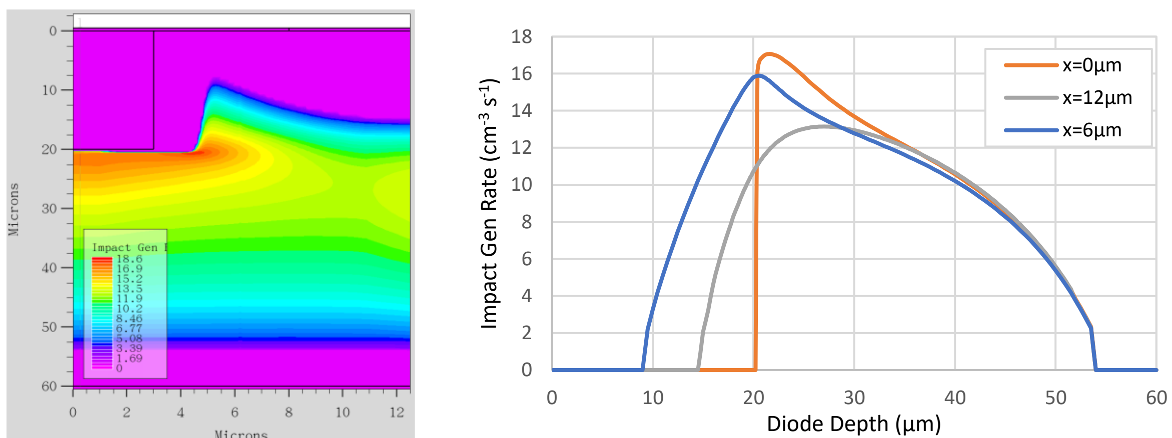

Figure 3.34 – (left) planar view of simulated impact ionization, and (right) impact ionization along the center cutline (x=0µm) and 6µm from the center.

3.4.3.1. Scintillating Deep Pit Devices

Figure 3.35 – Deep pit photodiode structure with the center conductor replaced with a scintillator.

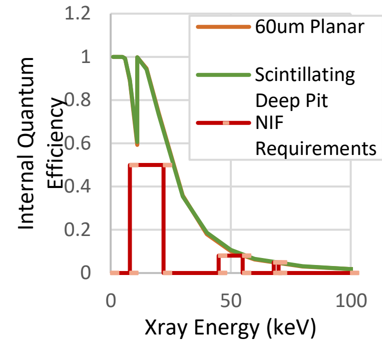

Figure 3.36 – Calculated internal quantum efficiencies of 60μm germanium PiN and scintillator-germanium PiN hybrid. Data from [4].

During the investigation of deep pit devices, a question arose: if the central pit will be filled with a dielectric, is any gain to be had from filling the pit with a scintillating material for additional quantum efficiency gain? To answer this question, a simplified model was used in which the x-ray attenuation coefficients of various scintillators were used, and fluorescence was assumed to be lossless. Figure 3.35 shows this structure. Table 3.10 shows the scintillating speeds of various materials, and the only material fast enough for this design is BaF_2. Observe that this structure eliminates the reduced image quality issue typical to scintillating photodiodes, making this a useful area to explore with simulations. Using Equation 3.9 and the mass-attenuation coefficients of BaF_2, the effective internal quantum efficiency of a scintillating deep pit can be calculated to make an effective comparison with a planar 60μm planar photodiode.

Material	Decay time (ns)
CsI:Tl	800
Mal:Tl	230
$LaBr_3$:Ce	35
K_2LaI_5:Ce	24
BaF_2	0.6–0.8
$Bi_4Ge_3O_{12}$	300
$PbWO_4$	2–3
$CdWO_4$	5000
$YAlO_3$:Ce	20–30
$LuAlO_3$:Ce	18
$Y_3Al_5O_{12}$:Ce	90–120
$Lu_3Al_5O_{12}$:Ce	55
Gd_2SiO_5:Ce	60
Lu_3SiO_5:Ce	30

Table 3.10 – Decay time for various inorganic scintillating materials. Data obtained from [74].

$$\eta_{effective} = \frac{A_{Pit}\left[1-\left(1-\eta_{BaF_2,15um}\right)\left(1-\eta_{Ge,45um}\right)\right] + A_{Non-Pit}\eta_{Ge,60um}}{A_{Det}} \tag{3.9}$$

As can be seen in Figure 3.36, effective internal quantum efficiencies hardly increase with the given geometry. Fabrication complexity increases significantly as well. Not only does the conformal deposition of oxides within the pit increase the research and development time of the device, but metal must also be kept less than 10nm in thickness and coated with an anti-reflective coating to maximize optical photon transmission. It is for these reasons that this architecture was abandoned.

3.4.4. Hybrid Structures

Hybrid structures were simulated in Silvaco to see if multiple structures could be combined to leverage their individual strengths simultaneously. Specifically, the 20µm pit photodiode was combined with the eight-layer superjunction photodiode with an intrinsic impurity concentration of 10^{14} cm^{-3} to attempt to further reduce the depletion bias, as can be seen in Figure 3.37. Figures 3.38, 3.39, and 3.40 show the internal field electric field, x-ray response, and impact ionization, respectively. Unfortunately, as can be seen in Figure 3.41, it does not appear possible to reach saturation velocity everywhere within the photodiode. However, as can be seen in Figure 3.42, temporal performance gains are had over the GPSJ anyway, partially due to the decreased distance photogenerated carriers must travel to the anode, and partially because of the reduced capacitance of the design. As expected, the hybrid structure inherits the increased impact ionization of the deep pit photodiode. This can be modulated by varying the number of

layers, the pit depth in the photodiode, the layer width. However, the x-ray results make this device look the most promising.

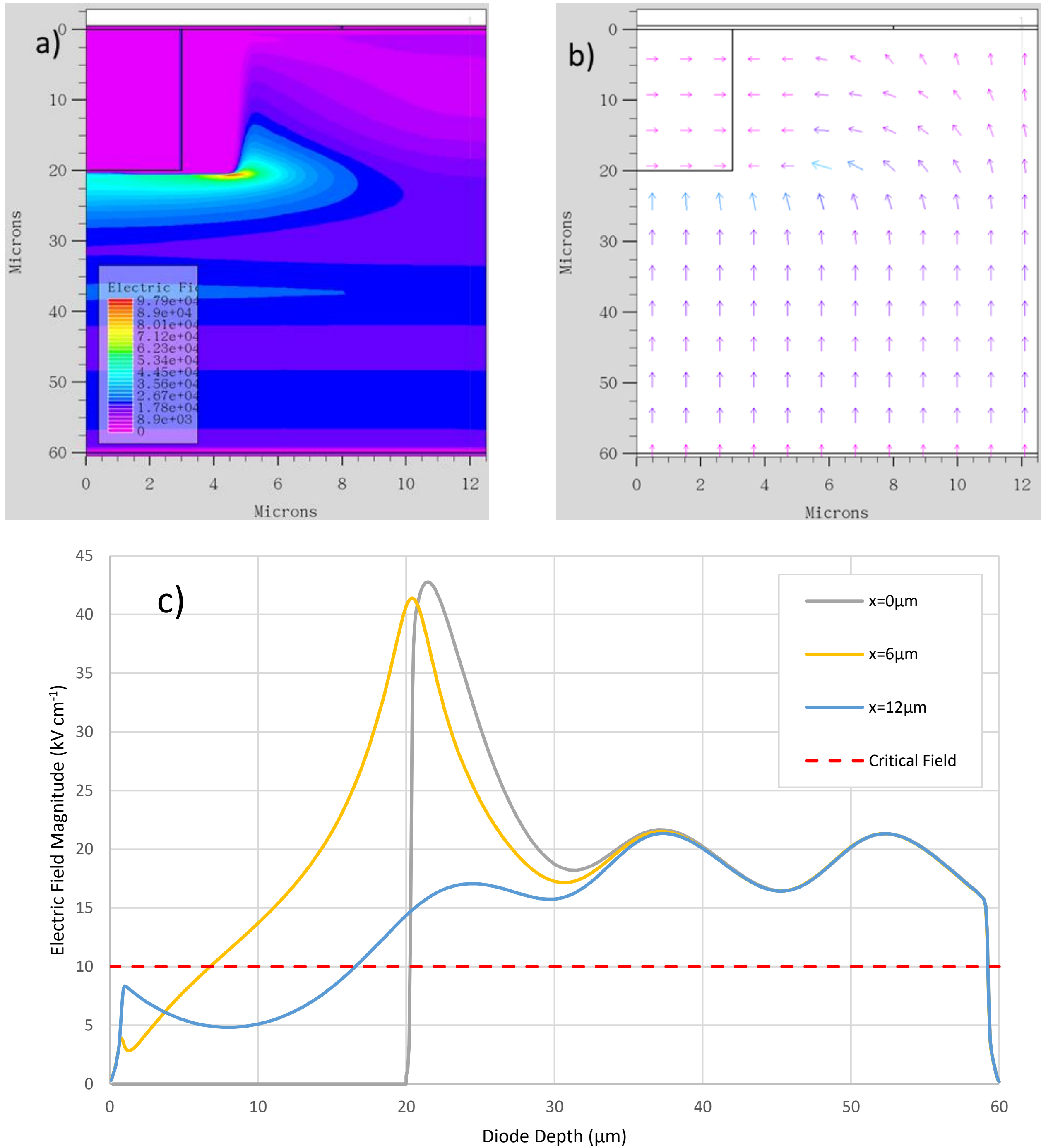

Figure 3.38 – (a) planar view of electric field magnitude, (b) vector view of electric field, and (c) electric field across multiple cutlines. Biased at -85V.

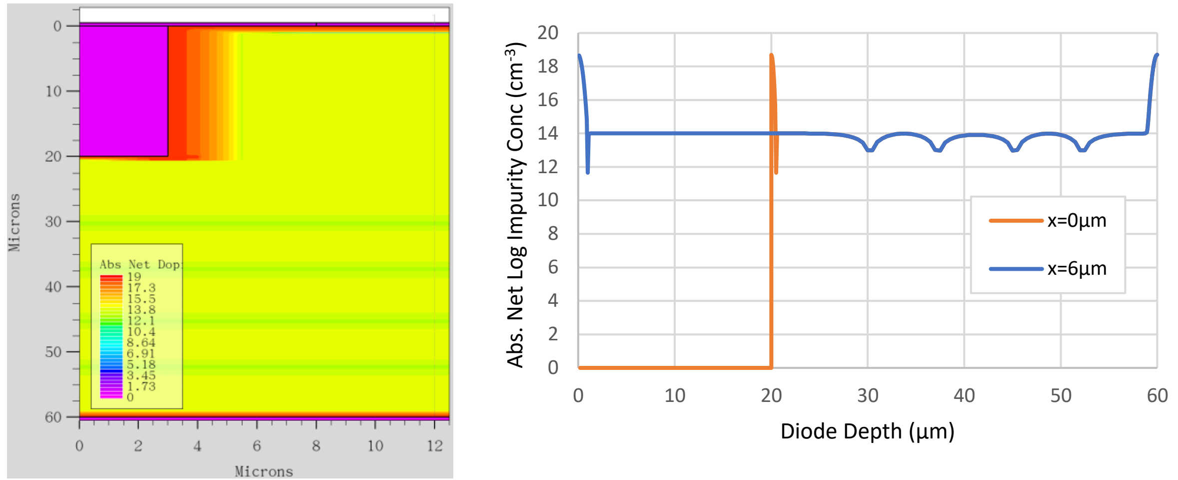

Figure 3.37 – (left) planar view of simulated structure doping, and (right) doping along the center cutline (x=0μm) and 6μm from the center.

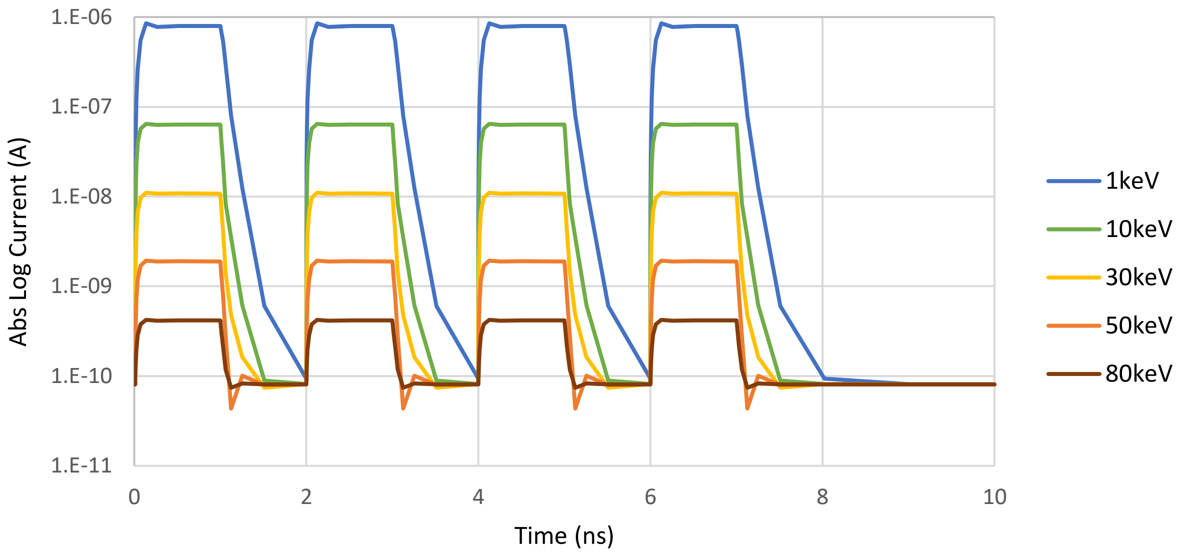

Figure 3.39 – Photodiode response to x-ray pulses.

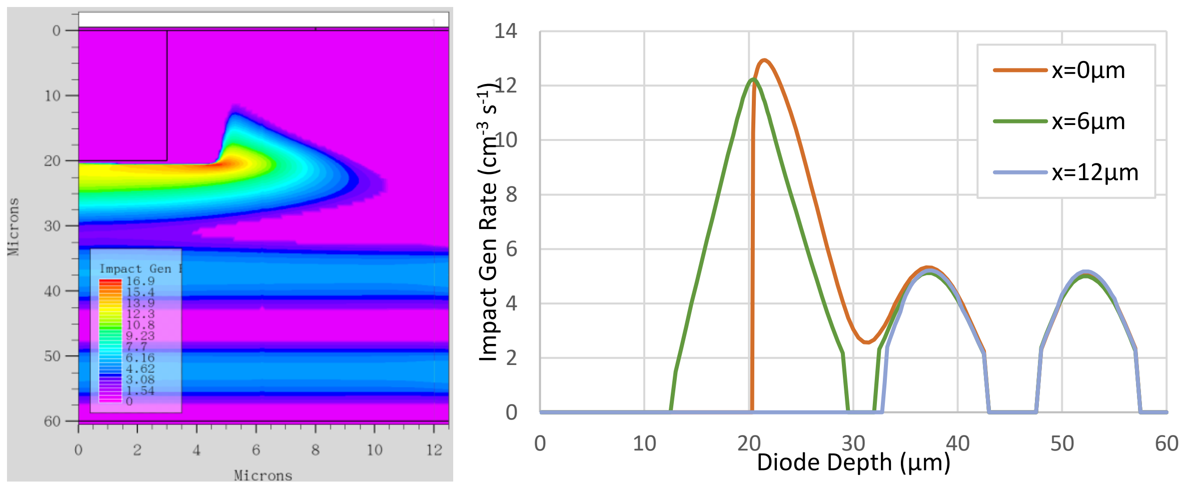

Figure 3.40 – (left) planar view impact ionization, and (right) impact ionization along the center cutline (x=0μm) and 6μm from the center.

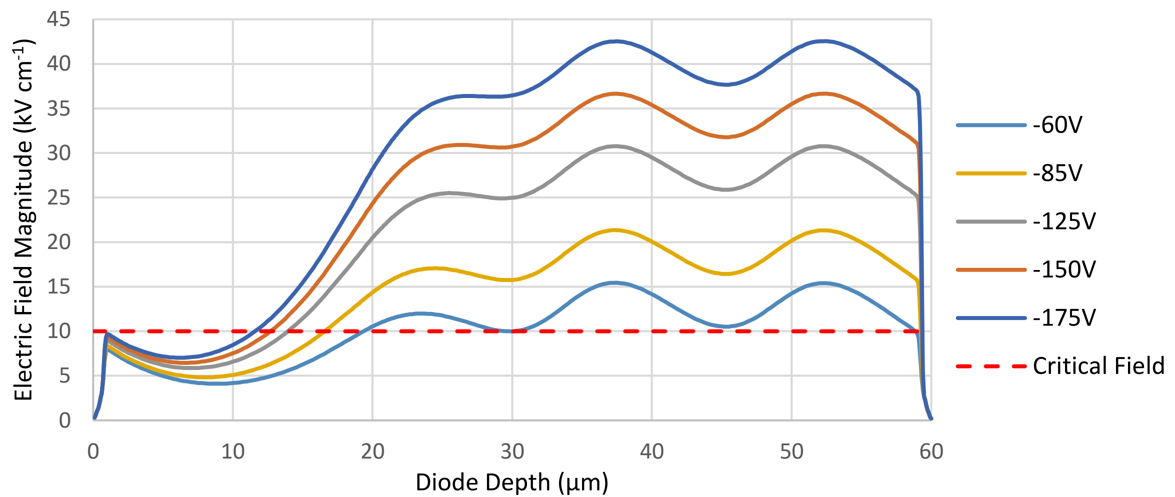

Figure 3.41 – Electric field magnitude 12µm away from center of hybrid photodiode structure at various biases.

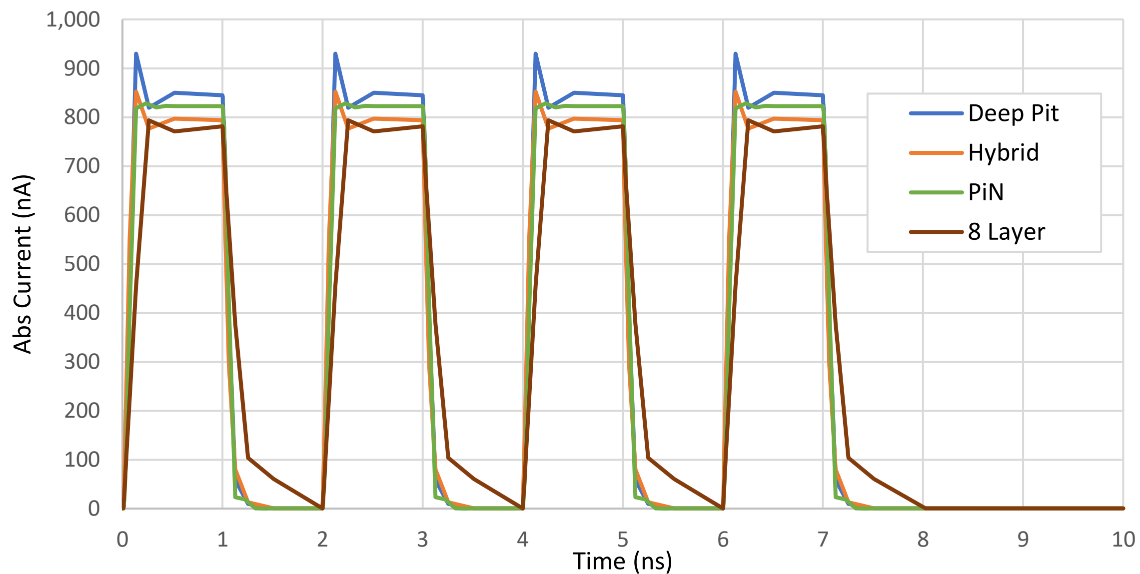

Figure 3.42 – Photodiode response to x-ray pulses of various designs. Temporal response of the deep pit, hybrid, and PiN are comparable.

3.5. Conclusions

The search for a photodiode structure to achieve device requirements proved fruitful. While none of these simulations have been compared to fabricated devices, these results nonetheless provide a roadmap for future germanium photodiode development for high-speed, low bias germanium photodiodes, with the most

promising device being the hybrid structure from Section 3.4.4. Once fabricated, the I-V characteristics of these architectures will be compared against the results plotted in Figure 3.6.

Chapter 4 – Fabrication Challenges

The temporal and quantum efficiency advantages of germanium photodiodes are clear. There are however six major challenges to overcome before production can move from prototypes to the final imaging array: high intrinsic impurity concentration, ohmic cathode formation, surface passivation, anode stability, substrate wafer etch, and post-dicing passivation. Only the first two will be discussed here, substrate wafer etch is an ongoing effort as part of a separate doctoral project, and a solution to the high impurity concentration problem was discussed in Chapter 3. Because epitaxial wafers were grown at LSRL, nothing can be done by the writer of this dissertation. This chapter describes the problems in greater detail and, when possible, provides solutions, and builds upon significant work already performed in this area [5, 99, 100].

4.1. Surface Passivation

Recall from Chapter 2 that surface defects cause a decrease in carrier lifetimes and an increase in generation-recombination centers. Unless there exists a film to bond with all the available bonds on the surface of germanium, the entire surface of the semiconductor is a defect, page 413 of [25]. With silicon, the surface forms a film consisting of a single chemical, silicon dioxide (SiO_2) [101]. However, the surface of germanium forms many forms of oxides, causing the formatting of dangling bonds, as seen in Figure 4.1, and thus defects to form [31]. For germanium semiconductor devices, surface passivation falls into six categories: germanium oxide passivation (GeO), epitaxial silicon, dielectric film deposition with atomic layer deposition (ALD), surface sulfurization, amorphous germanium, and amorphous hydrogenated silicon [39, 102-109]. Each of these methods strives to reduce the density of suboxides, and thus interface traps, at the interface layer. Figure 4.2 demonstrates these various passivation stacks. Four methods of passivation were tested with epitaxial germanium for this dissertation: conversion of GeO_X films to GeO films, ALD, sulfurization, and combinations of these. The ALD films tested are Al_2O_3, HfO_2, and SiO_2.

Before passivation can be done, the surface must first be cleaned of organics and other contaminants [102, 110, 111]. Without properly cleaning the layer before depositing the passivation material will not be able to bond with germanium on the surface, causing the interface can be corrupted. This cleaning entails removing surface contaminants including oxides and organics, while leaving the surface relatively smooth. In addition to removing contaminants, cleaning methods can incorporate chemicals that can add a temporary passivation layer to the surface. This layer is unstable in air but can protect the surface from oxidation and contaminants for a few hours. Some temporary passivation layers have shown to promote better long-term passivation characteristics after being protected from decay in air by adding a permanent passivation layer on top [112, 113]. In this work, sulfur is the temporary passivation material tested. HCl, HF, and $(NH_4)_2S$ wet etches can terminate with chlorine, hydrogen, and sulfur, respectively. However, studies have shown that not only does S have superior stability properties to that of H and CL, but sulfur termination can also act as a stable passivation layer after the deposition of films with ALD [112].

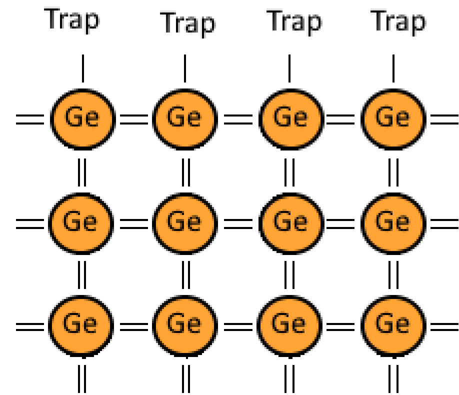

Figure 4.1 –Unpassivated germanium surface.

Following cleaning, the GeO_X suboxides residing surface must be converted to GeO using an oxygen plasma. Unlike GeO_X, GeO is not water soluble, and can be removed with a +390°C anneal in vacuum if desired. GeO_2 can be removed with a higher temperature vacuum anneal of +600°C, but this temperature surpasses the PiN increases impurity diffusivity throughout the crystal, damaging the internal structure. Additionally, acids such as HCl have been shown to remove germanium oxides. These acid cleanings are often performed several times, each cleaning step having a duration of a couple of minutes. In between

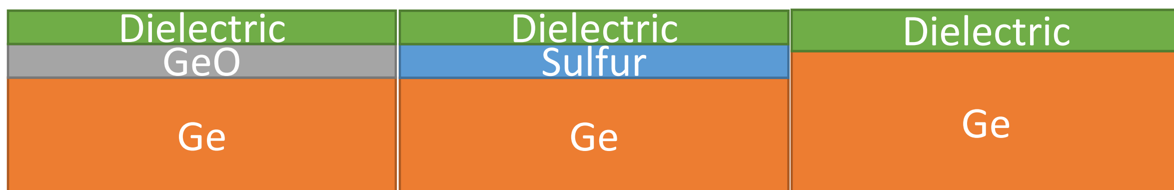

Figure 4.2 – (left) GeO passivation, (middle) sulfur passivation, and (right) dielectric passivation.

each acid cleaning step, a DI water rinse is performed. Since GeO_2 is water soluble the DI rinsing step in the cyclic etch likely aids in removing GeO2 by using two different removal mechanisms (water and HCl) in step of one.

Organics can be effectively removed by methods including oxygen plasma treatment and some wet etches. The wet etches include HCl and NH_4OH. Once the oxide is removed, any of the organic removal methods clean the surface of organics initially, but organics could redeposit on the surface afterwards if exposed to the atmosphere. If the surface is not subjected to organics removal in-situ in the ALD, then oxides and organics will recontaminate the surface. Where GeO could not be used as a protection layer, S was used as a temporary protection layer. Samples that were soaked in $(NH_4)_2S$ are protected from contamination after the soak for up to 4 hours, though the duration of protection was not verified experimentally. Additionally, the sulfur- termination layer remains on the Ge surface after the ALD and has be shown to have a lower D_{it} than Ge without the temporary passivation layer.

4.1.1. Experimental Procedure

Continuing the work of [100], 1.5cm by 1.5cm epitaxially grown germanium chips were first cleaned by submerging in five minutes each in acetone, methanol, and isopropanol. The samples were then rinsed in DI water and blown dry with N2. To make sure each sample had the same thickness of oxide, an oxide layer was gown on each samples' surface by submerging the samples in H2O2 (10%) for thirty seconds, followed by a N2 dry. Then every sample was exposed to oxygen plasma for fifteen minutes. Next some of the samples were cleaned with the cyclic HCl etch. This etch has two steps consisting of submerging the samples in HCl (30%)

Sample Number	HCl Clean	Ex-Situ Anneal	$(NH_4)_2S$	In-Situ Anneal
1				
2	✓			
3		✓		
4	✓	✓		
5			✓	
6	✓		✓	
7		✓	✓	
8	✓	✓	✓	
9	✓			✓
10		✓		✓
11	✓	✓		✓
12			✓	✓
13	✓		✓	✓
14		✓	✓	✓
15	✓	✓	✓	✓

Table 4.1 – Experimental combinations of processing steps.

for 2min and then rinsing the samples in DI for 30s. These steps were repeated three times per samples. Then some of the samples were annealed for 400C, some in-situ in the ALD chamber and some ex-situ. Next, some of the ex-situ annealed samples were submerged in $(NH_4)_2S$ for twenty minutes to terminate the surface in sulfur and were the DI rinsed and N_2 blown dry. Finally, ALD was performed on the samples to deposit the dielectric passivation layers. Samples received one of three different materials: Al_2O_3, HfO_2, and SiO_2. The thickness of each ALD layer was then measured using ellipsometry and were found to be within 1nm of 6nm, the intended thickness. Table 4.1 summarizes the cleaning steps taken for each sample. Table 4.1 was done a total of 3 times so that each dielectric material, hafnia, silica, and alumina, could be deposited on each 14-chip group. Having different samples undergo different combinations of steps allows for a direct comparison of the effectiveness of the various passivation methods.

4.1.2. Results

Figure 4.3 shows two methods were found effective in reducing GeO_2 counts: any sulfur termination method without an *in-situ* anneal and HCl bath + ex-situ annealing. The GeO_2 oxide count was likewise capping material invariant. While the HCl + anneal method has some GeO_2 on the surface, sulfur termination has none. Given these results, sulfur termination is found to be extremely effective at passivating epitaxial germanium. 0020Figure 4.4 shows a sampling of the ineffective methods of XPS results. GeO_2 counts were found to be invariant of the capping dielectric used. [114] was used to help collect data. Unfortunately, all silica samples were found to be contaminated. This was not observed until after the XPS data had been collected. As will be seen in the next section, methods containing the in-situ anneal step proved unfruitful.

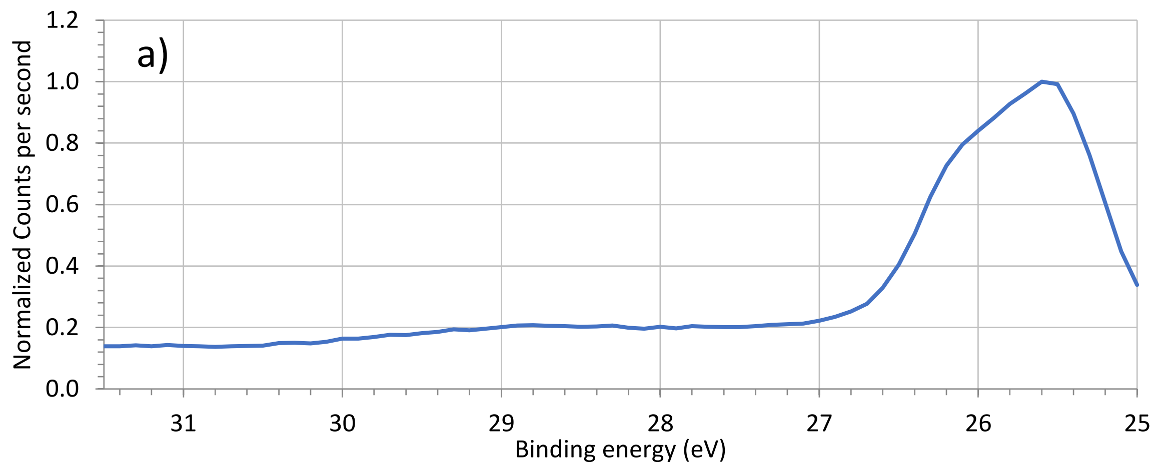

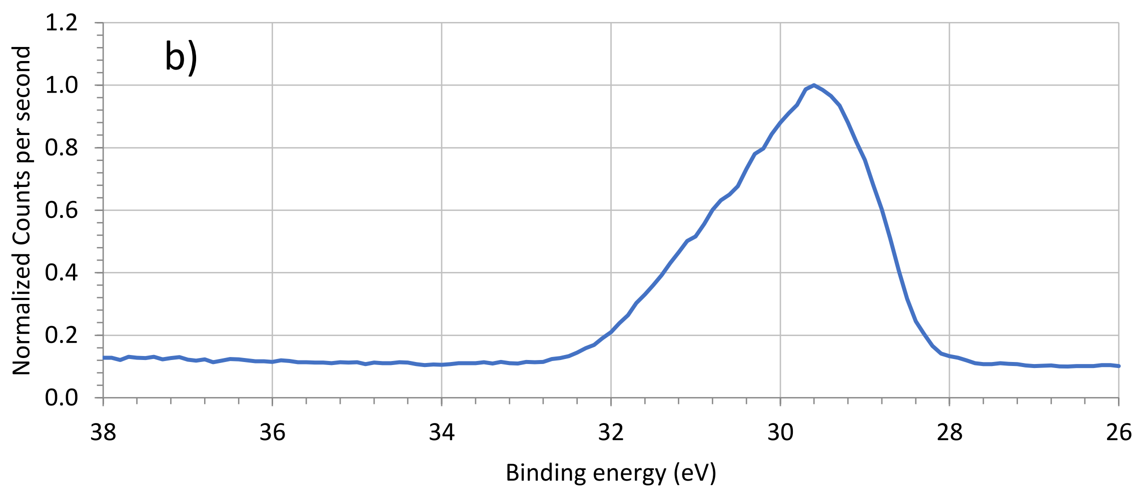

Figure 4.3 – (a) average count of samples undergoing the HCl + anneal steps, and (b) S terminated. All binding energies unadjusted relative to C footprint.

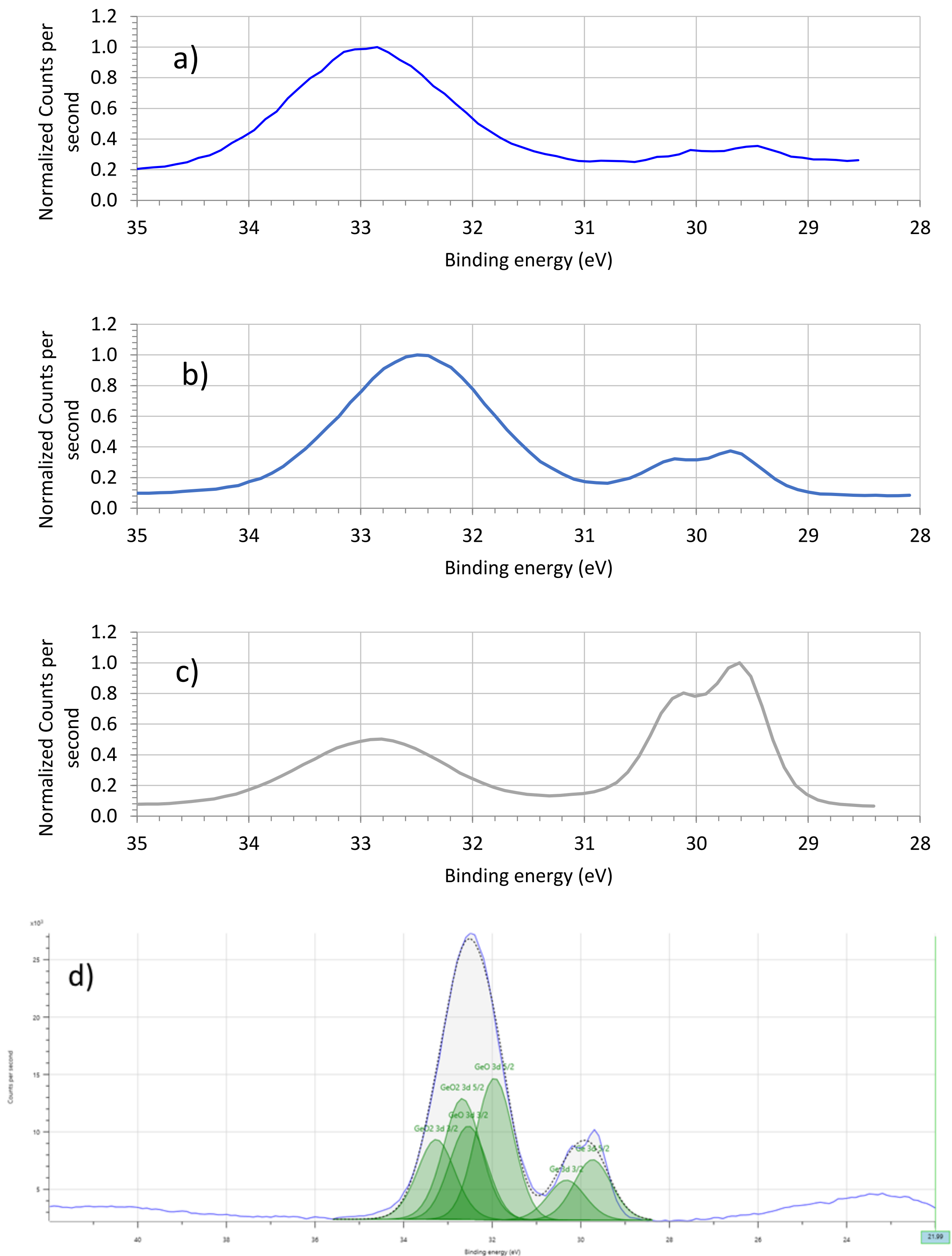

Figure 4.4 – (a) average count of samples undergoing the anneal step only, (b) HCl only, (c) all silica samples, and (d) fitted HCl only sample showing equal amounts of GeO_2 and GeO. All binding energies unadjusted relative to C footprint.

4.2. Cathode Ohmic Contact Formation

Metal-Semiconductor contact formation is crucial for the success of any semiconductor device. Two of the primary metrics for judging the quality of a contact are its contact resistance and whether it is an Ohmic or Schottky contact, chapter 3 of [13]. In a PiN structure, it is desirable that both electrodes are ohmic, exhibiting linear I-V characteristics with a minimal voltage drop across the contact. To achieve such a low voltage drop at the contact, the charge carriers arriving at the metal-semiconductor junction must meet a low barrier to entry; this is known as accumulation mode, chapter 3 of [13]. Typically, accumulation is possible when the work function of the metal is less than that of the semiconductor. In contrast, depletion-mode occurs when the metal work function is higher than that of the semiconductor. Depletion restricts the flow of carriers by increasing the energy barrier at the metal-semiconductor junction. Band diagrams of both anodes and cathodes under various conditions can be seen in Figure 4.5.

Unfortunately, it has been reported that the barrier height in Ge remains high independent of the metal regardless of work function, as seen in Figure 4.6 [92-94]. This phenomenon is called Fermi level pinning and can be seen in Equation 4.1a and Equation 4.1b [92].

$$\Phi_{b.e} = S(\Phi_m - \Phi_{CNL}) + (\Phi_{CNL} - \chi_S) \tag{4.1a}$$

$$S \equiv \frac{\partial \Phi_{b.e}}{\partial \Phi_m} \tag{4.1b}$$

Where $\Phi_{b,e}$ is the electron barrier height in eV.

Germanium exhibits a pinning factor of 0.1 [92], a strongly pinned surface. In germanium, this creates depletion and Schottky contacts on any N-doped surface.

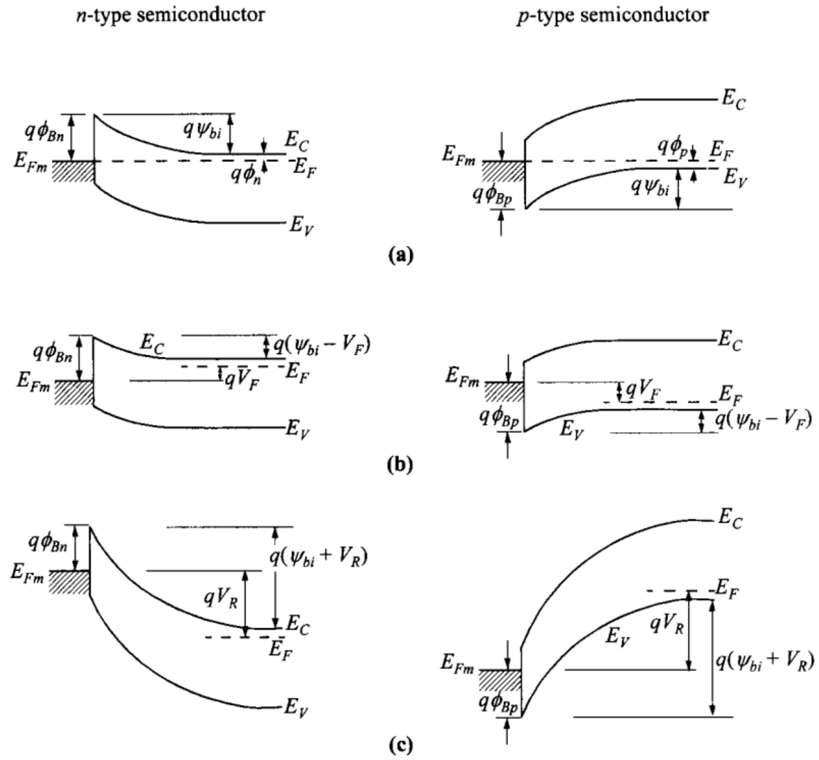

Figure 4.5 – Energy band diagrams of metal on semiconducting material under (a) thermal equilibrium, (b) forward bias, and (c) reverse bias. Reproduced from [13].

It is hypothesized that Fermi level pinning in Germanium is caused by the high density of surface states present at the metal-semiconductor interface [92-94]. Surface states can be present because of chemical bonding between the metal and semiconductor or a high interface trap density. These surface energy states essentially hold enough charge to pin the Fermi level regardless of the influence of the metal work function. In N-type germanium, the Fermi level is strongly pinned close to the charge neutrality level, which is about 0.09eV from the valence band [92]. The result of fermi level pinning results in N-type germanium contacts having high resistances and being rectifying in nature.

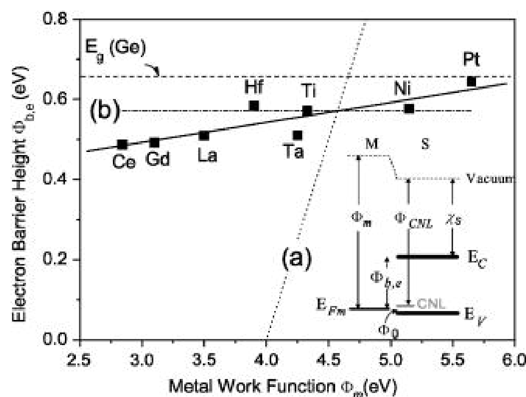

Figure 4.6 – Measured electron barrier height of N-type germanium with various metals.

Several strategies have been proposed to alleviate fermi level pinning in germanium contacts. The first is through ion implantation, which has been shown to modulate the Schottky barrier height, lowering the resistivity of the contacts [115]. However, due to the brittle nature of germanium, ion implantation can produce a porous surface [116], rendering this

approach as undesirable. The second approach uses a several-nanometer thick interlayer to reduce metal-induced gap states by suppressing the metal wave function from tailing into the semiconductor bandgap [117-121]. This causes charge carriers to tunnel through the interlayer, and while it does not alleviate the fundamental problem of Fermi level pinning at the cathode, it removes it as an issue. To find the most favorable interlayer and metal combination for the imaging array, a variety of combinations of interlayer and metal were deposited on germanium. These materials are outlined in Table 4.2. A graphical representation of this approach can be seen in Figure 4.7.

4.2.1. Experimental Procedure

Continuing the work of [99], 1.5cm by 1.5cm epitaxially grown germanium chips were first cleaned by submerging in five minutes each in acetone, methanal, and isopropanol. Solution containers were put into a sonicator for agitation. Following this, Ge chips were placed into a PETS reactive ion etching (RIE) machine for oxygen plasma treatment to convert the various germanium suboxides (GeO_X) to GeO for ease of desorption.

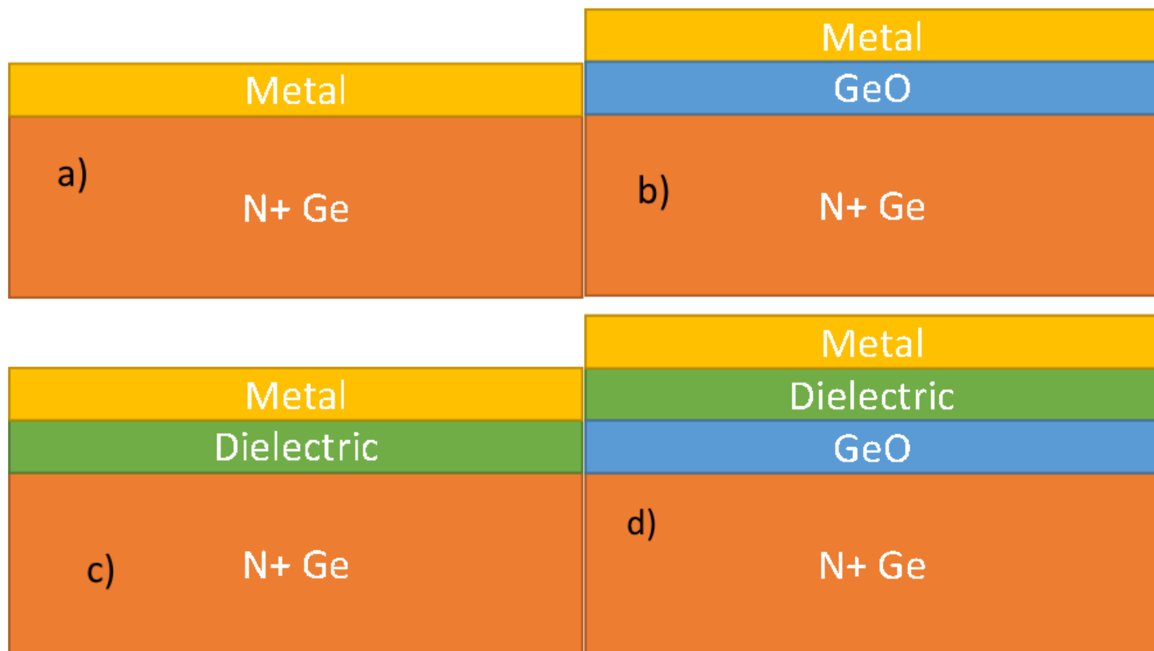

Figure 4.7 – Experimental combinations. (a) Metal on semiconductor, (b) metal on germanium oxide, (c) metal on oxide, (d) mixed.

Additionally, as a control, one 1.5cm x 1.5cm chip of germanium was cleaned in the same sonicator bath sequence as the other, and afterwards was exposed to a cycle HCl-H_2O_2 bath to etch the oxide. Following this, some chips were loaded into a Lesker Labline sputtering system, and some were loaded into a Picosun R-200 PEALD machine for interlayer deposition. Before depositing dielectric interlayers, some chips were exposed to an in-situ anneal under vacuum to desorb the oxide layer, and some were not. This is summarized in Table 4.3. Annealing was done at 400C at a pressure of 1.5 Torr in the ALD machine and $5x10^{-6}$ Torr in the sputtering machine. Anneal duration was 30 minutes. Samples were not exposed to the atmosphere after the anneal to prevent oxide layer regrowth. All dielectric film thicknesses were checked by an ellipsometer for film thickness after deposition.

Interlayer	Deposition Method	In-Situ Anneal?	Thickness (nm)	Metal	Deposition Method	Thickness (nm)
Pd	E-Beam Evap.	No	5, 150	Au	E-Beam Evap.	150
Al_2O_3	ALD	Yes	2, 3.5, 5	Ni	E-Beam Evap.	70
Al_2O_3	ALD	No	2, 3.5, 5	Ni	E-Beam Evap.	70
TiN	Sputter	Yes	2, 3.5, 5	Al	Sputter	50
Ni	E-Beam Evap.	No	5, 50	Ti/Au	E-Beam Evap.	50/100
Au	E-Beam Evap.	No	5, 30	Ni	E-Beam Evap.	70
ZnO	ALD	Yes	2, 3.5, 5	Al	Sputter	50
Cr	E-Beam Evap.	No	5, 20	Au	E-Beam Evap.	100

Table 4.2 – List of different metal/interlayer combinations, thickness of the layers, and deposition method for P-type Germanium.

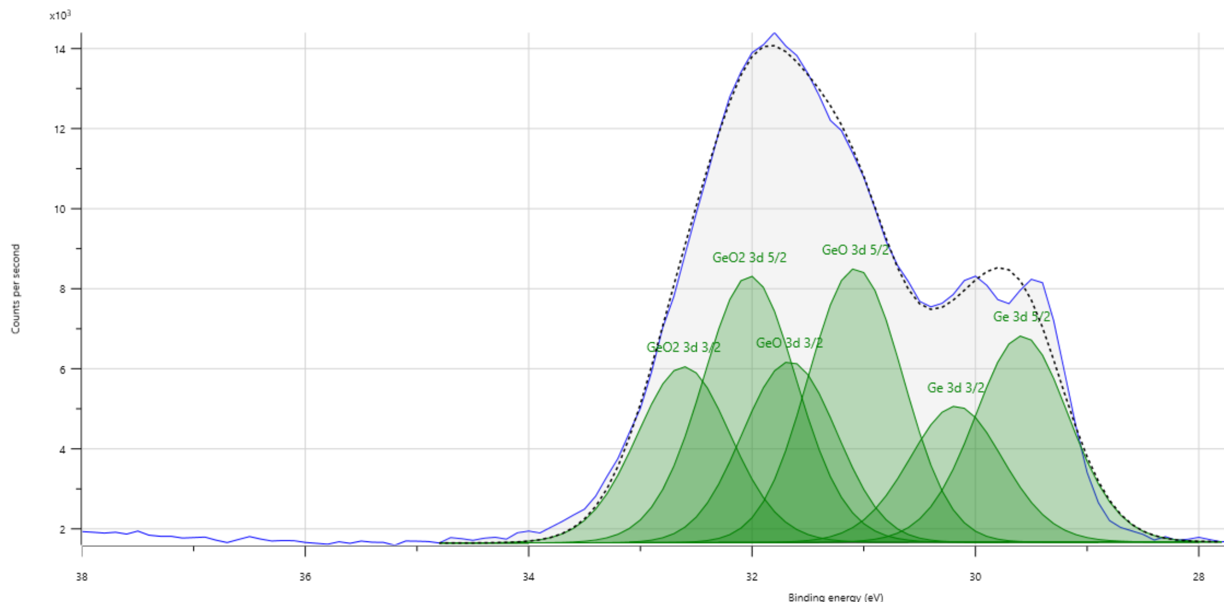

Figure 4.8 – XPS model of GeO and GeO2 count after an in-situ anneal in the ALD machine. Equal amounts of both oxides can be seen.

4.2.2. Results

Unfortunately, due to the relatively high pressure in the ALD machine, the ellipsometer found films deposited in the ALD machine to be 4nm thicker than intended, revealing oxides had regrown after the anneal. Following these depositions, all samples were loaded into an x-ray photoelectron spectroscopy (XPS) machine to examine the presence of germanium oxides on the surface.

As seen in Figure 4.8, XPS results only confirmed what the ellipsometer had shown: that oxides had regrown on the surface of germanium after the anneal. Because these oxides hinder the tunneling effect needed for ohmic contact formation, this experiment is currently undergoing a redesign.

4.3. Metallization Adhesion and Stability over Time

It has been observed that metallization on the anode is not stable, manifesting as flaking over time. Moreover, wire bonding has been found to be of very poor quality at best and impossible at worst during the SMA packaging process. This is manifested by the surface metallization being torn off by the wire bonder on most attempts, and an unstable bond when

Figure 4.10 – Schematic diagram of anode metalization.

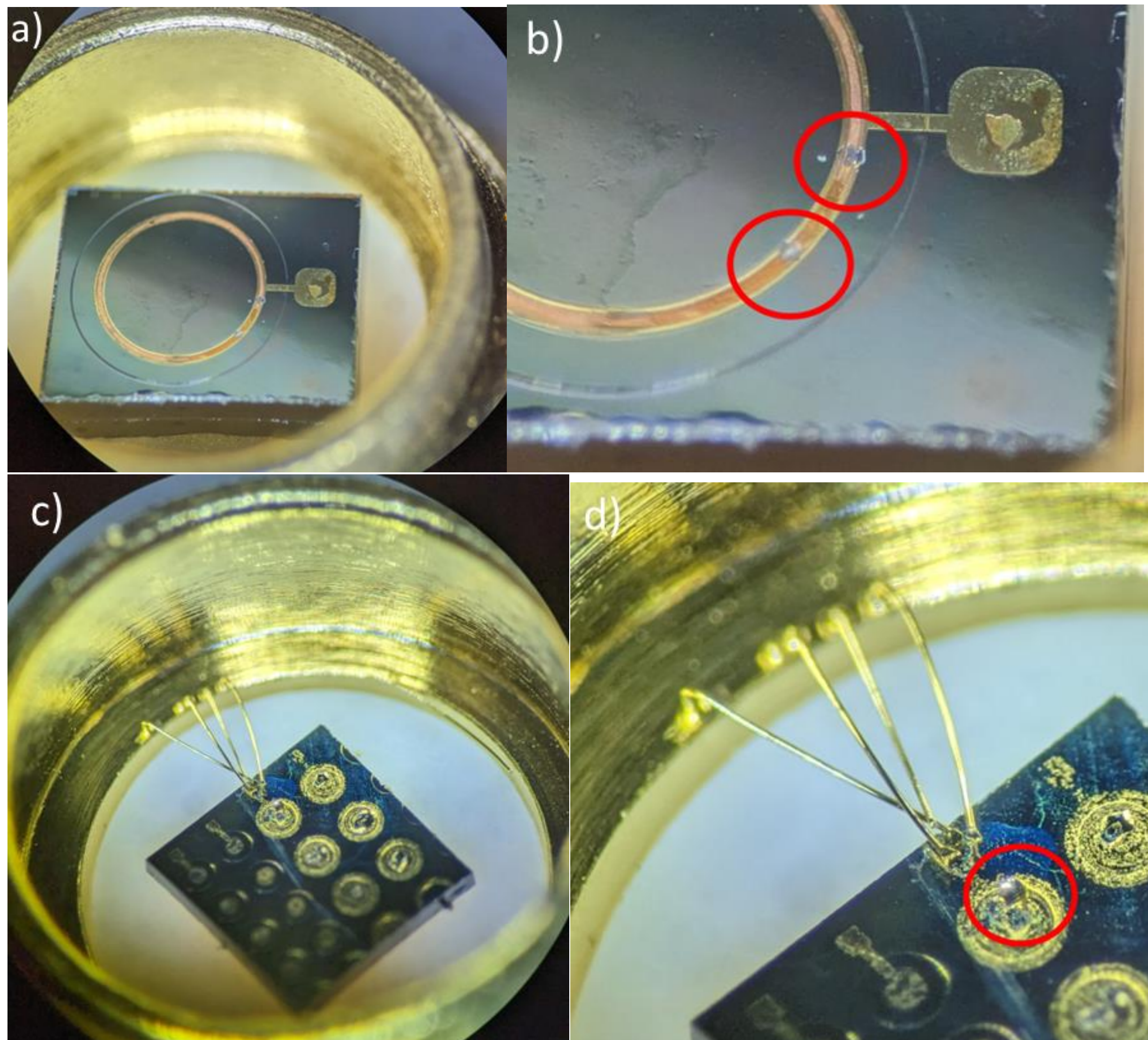

Figure 4.9 – Metal delamination during wire bonding and over time. (a) Microscopic view of ringed anode fabricated by the writer of this dissertation, (b) close up of anode with red rings highlighting failed wire bonding, (c) microscopic view of photodiodes fabricated for [141], (d) close up with red ring highlighting failed wire bonding. Wire bond in (c) and (d) had to be reinforced, hence the presence of multiple wires in (c) and (d). The differences in severity of the flaking is due to a difference in time exposed to atmosphere, where (a) was exposed to one year and (c) was exposed for three years.

it does succeed, causing bonds to tear off with shock or time. Figure 4.9 demonstrates all these problems under an optical microscope. For the devices fabricated for x-ray testing, platinum (Pt) was deposited onto the surface of germanium as an interlayer and gold (Au) was deposited on top of it. A schematic diagram of this can be seen in Figure 4.10. Several Pt/Au thickness combinations have been attempted to rectify this delamination problem, in Table 4.4. However, the problem persists. Moreover, the problem has been observed across two different cleanrooms and recipes, implemented by two different experimenters. Thus, the issue is unlikely to be of poor technique or bad materials.

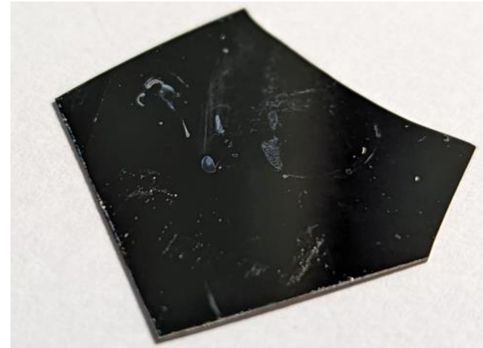

Figure 4.11 – Uncleaned cathode surface. Adhesion has been stable over time.

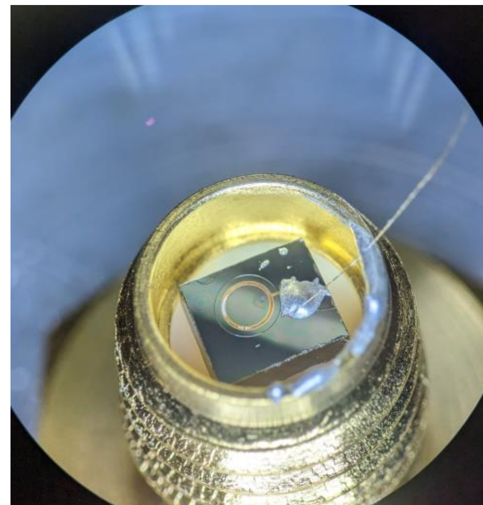

Figure 4.12 – wire bonding with silver epoxy. Care must be taken to avoid the active area of the detector.

Two possible causes to the problem exist: either delamination is caused by poor surface oxide quality of germanium or Pt is a poor interlayer for the gold. The same problem has not been observed with cathode metallization, seen in Figure 4.11, hinting at the Pt being the culprit. However, the definitive answer is currently unknown. Thus, an experiment has been planned to solve this problem.

The experiment consists of two parts: redeposit the Pt/Au combination with surface cleaning methods in Section 4.1 applied and try different metallization combinations. As seen in Section 4.1, several methods exist to clean the surface of germanium and convert the various sub-oxides to GeO. After the conversion the same Pt/Au recipe will be attempted. As for the second part, several metals will be attempted with p-type germanium, including aluminum, indium-gallium, titanium, and gold, as suggested by literature [122-124]

Unfortunately, the experiment has never gotten past the first part. After the conversion of surface oxides the sample was sent to an XPS laboratory for characterization, but this problem was observed late in the doctoral study, and little time remained for anything but x-ray testing. Thus, Figure 4.6 shows the XPS results of surface oxides on the germanium chip, but no more results are available. The study will be continued in LLNL. As a temporary solution, silver epoxy was used to bond wires to the bonding pad, as seen in Figure 4.12.

4.4. Backside Etch

An important step in the fabrication of the photodiode array is the removal of the substrate wafer. There are two approaches proposed to remove the backside: chemical-mechanical planarization and chemical etch, page 178 of [40]. Chemical-mechanical planarization was attempted for this dissertation on a Logitech PM2A lapping and polishing machine. Instrumentation and Labview software were constructed to perform current-controlled chemical etching of the backside. Research is ongoing as part of a separate PhD program.

As seen in Figure 4.13, taken with an optical microscope, long but narrow etch marks exist on the surface of germanium after chemical-mechanical polishing. In a brittle material, several unintended cracks

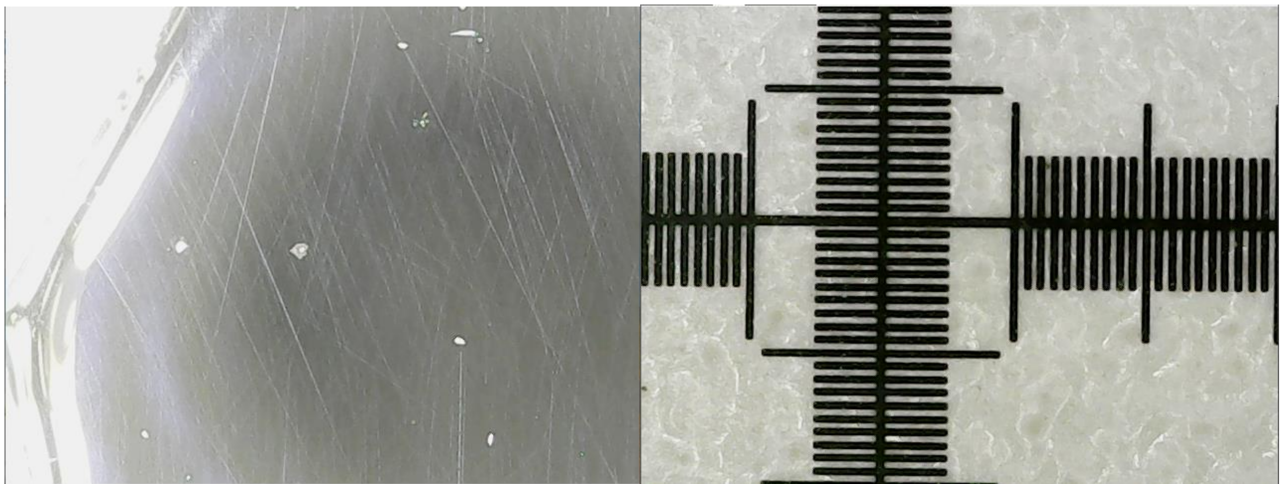

Figure 4.13 – lapping on the surface of a germanium chip surface post lapping and polishing. (Left) photo of chip, (right) 100µm spacing at same scale for comparison. Lapping and polishing produces very many surface defects that are less than 100µm in thickness but very many mm in length.

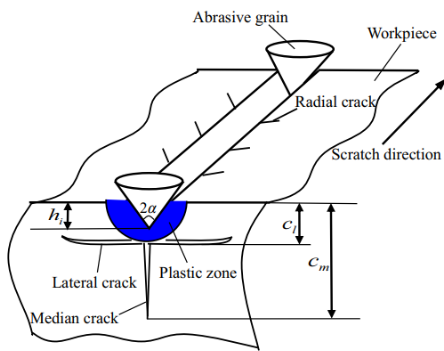

Figure 4.14 – cracks formed on a brittle material from an abrasive particle. Reproduced from [122].

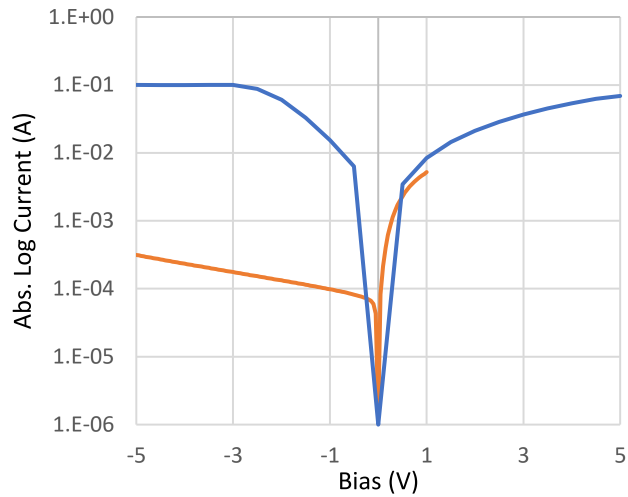

Figure 4.15 – Voltage-current characteristics (orange) before and (blue) after dicing and packaging.

propagate from an abrasive grain contacting the surface, including radial cracks, lateral cracks, and median cracks, as seen in Figure 4.14, pages 65-81 of [125]. Because of this, subsurface damage is likely to have been developed and contribute additional generation-recombination centers within the body of the photodiode, raising the dark current. Unfortunately, subsurface damage and roughness were not measured. Equally unfortunately, devices could not be fabricated with the resulting chips as the optical stepper used could not focus on such thin pieces. Contact lithography could not be used without risk of exacerbating damage. Thus, it is currently unknown if these etch marks make surface passivation or metallization more difficult, or how much dark current is raised by this method. Because chemical backside etch has so far been largely unsuccessful, this experiment will be revisited.

4.5. Post-Dicing and Packaging Voltage-Current Characteristics

While performing the temporal testing at the Advanced Light Source, described in Chapter 5, significant deviations from device IV characteristics were observed than those of pre-dicing and packaging. Furthermore, after the application of a bias for a sustained period, the breakdown voltage of devices decreased significantly, to the point of immediate breakdown. This has been observed to develop within the photodiode after a few seconds of applying biases below approximately -50V. Figure 4.15 demonstrates pre and post transformation currents for a 2mm ringed anode photodiode from Chapter 5. As can be seen,

the current limit of the SMU is reached in as little as -3V. If a compliance current was not set, it is likely that the current would climb past the 100mA mark.

It is likely that dicing is creating additional surface defects that are interacting with the device while biased, leading to a degradation of performance. [126] discusses various exotic defects that can occur while dicing, such as subsurface damage, bulk semiconductor fractures, and with metalization. Fortunately for the experiments in Chapter 5, devices were still able to function for temporal testing. The culprit behind this degradation in performance currently remains unknown however and will require further study. It is possible however that subsurface damage, bulk cracking, and exposed sides produce substantially larger defect densities, drastically increasing dark current.

Chapter 5 – Optoelectronic Measurements

Optoelectronic measurements consist of two phases: x-ray quantum efficiency measurements, and temporal response measurements, x-ray and optical. X-ray quantum efficiency measurements were performed partly at the Advanced Light Source (ALS) at Lawrence Berkeley National Laboratory (LBNL), and partly in the Manson Lab at Lawrence Livermore National Laboratory (LLNL). Temporal tests were done at the ALS. This chapter will discuss the data that demonstrates the methods that were used to acquire these data, presents the results of these measurements, and provides a brief discussion of what they mean.

5.1. X-Ray Quantum Efficiency Measurements

5.1.1. Methodology

5.1.1.1. General Procedure

Recall from Chapter 2 that the total current flowing from a photodiode is given by two components, the dark current and the x-ray current, Equation 2.28.

$$I = I_{Dark} + I_{x-ray} \tag{2.28}$$

Recall also that the x-ray current is a product of the power being irradiated onto the photodiode in Watts per unit area, the area of the irradiance, the material responsivity (a fixed value for each material), and the quantum efficiency, Equation 2.27.

$$I_{x-ray} = PAR\eta \tag{2.27}$$

By measuring the current of a photodiode that is being exposed to x-rays, and then the current of a diode not being exposed to x-rays, I_{x-ray} can be calculated. However, typically at least one of the variables in Equation 2.25 is unknown, making the direct calculation of the external quantum efficiency impossible. In

ALS, the area of the beam is difficult to find, and changes over time. In the Manson source, the power at any given time is unknown, as will be seen later. To rectify this, a second reference silicon photodiode with a well-known external quantum efficiency is tested alongside the germanium photodiodes. Using the x-ray and dark current of this additional photodiode, Equation 5.1 is then used to calculate the external quantum efficiency of the germanium photodiodes.

$$\eta_{Ge} = \frac{I_{Ge}}{I_{Si}} \frac{P_{Si} A_{Si} R_{Si}}{P_{Ge} A_{Ge} R_{Ge}} \eta_{Si} \tag{5.1}$$

With clever experimental design, the missing information can then cancel in Equation 5.1, allowing for the external quantum efficiency of the device under test to be solved for. In the ALS, even though the instantaneous beam area is unknown, the time average produces the same area of exposure for both. In this case we must simply record the power of the beam and the calculation can be made. In the Manson source, by having the photodiodes side by side and collecting current data simultaneously, the irradiances are close enough to perform the quantum efficiency measurement. All that must be done is measure the diode area under a microscope.

To eliminate multiplicative effects caused by impact ionization, photodiodes were left unbiased when being measured in the Manson lab and a bias of -240V applied in ALS, the minimum bias possible in the Keithley 2400 source measure unit.

Once external quantum efficiencies are calculated, they can be used to calculate the mass-attenuation coefficients of epitaxial germanium to be compared with those of elemental germanium in NIST. Recall from Chapter 2 that external quantum efficiency can be calculated with Equation 2.4b.

$$\eta = 1 - exp(-\mu_{\varepsilon} x) \tag{2.4b}$$

By manipulating this equation algebraically, we obtain Equation 5.2a. Because mass-attenuation coefficients do not take the density of the material into account, we arrive at Equation 5.2b as the final form.

$$\mu_\varepsilon = -\frac{\ln(1-\eta)}{x} \tag{5.2a}$$

$$\mu_\varepsilon/\rho = -\frac{\ln(1-\eta)}{\rho x} \tag{5.2b}$$

This is the central result of this experiment. It is imperative that the mass-attenuation coefficients of epitaxial germanium be equal to that of elemental germanium, which are seen in Figure 5.1. They can be inferred from external quantum efficiency measurements. If the coefficients are not the same, x-ray stopping power is stunted and the usefulness of the material and method must be reevaluated.

5.1.1.2. Devices Tested

In all, 32 devices of various epitaxial thicknesses and anode widths were fabricated for these quantum efficiency tests, and 29 survived the trip to ALS and instrumentation failure. Table 5.1 lists the various epitaxial thicknesses and anode diameters of the various fabricated devices. Third generation wafers were used for all devices to minimize the depletion bias. Optical microscope photographs of the diced and packaged devices can be seen in Figure 5.2. The fabrication mask and fully fabricated devices can be seen in Figure 5.3. Ringed anodes were chosen for optical light measurements and to minimize losses in low energy x-ray measurements (<6keV). All 28

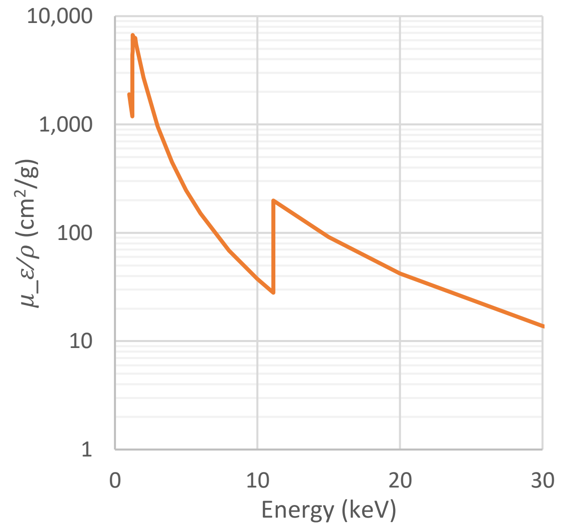

Figure 5.1 – Measured mass-attenuation coefficients for germanium from 1keV to 30 keV. Data obtained from [4].

Device Thickness	No. Devices	No. Large Ring Devices	No. Medium Ring Devices	Large Ring Etch ID (mm)	Medium Ring Etch ID (mm)
10µm	7	3	4	2.015	1.39
30µm	7	3	4	2.015	1.39
60µm	7	3	4	2.015	1.39
245µm	7	2	5	2.015	1.39

Table 5.1 – devices fabricated for optoelectronic testing of germanium.

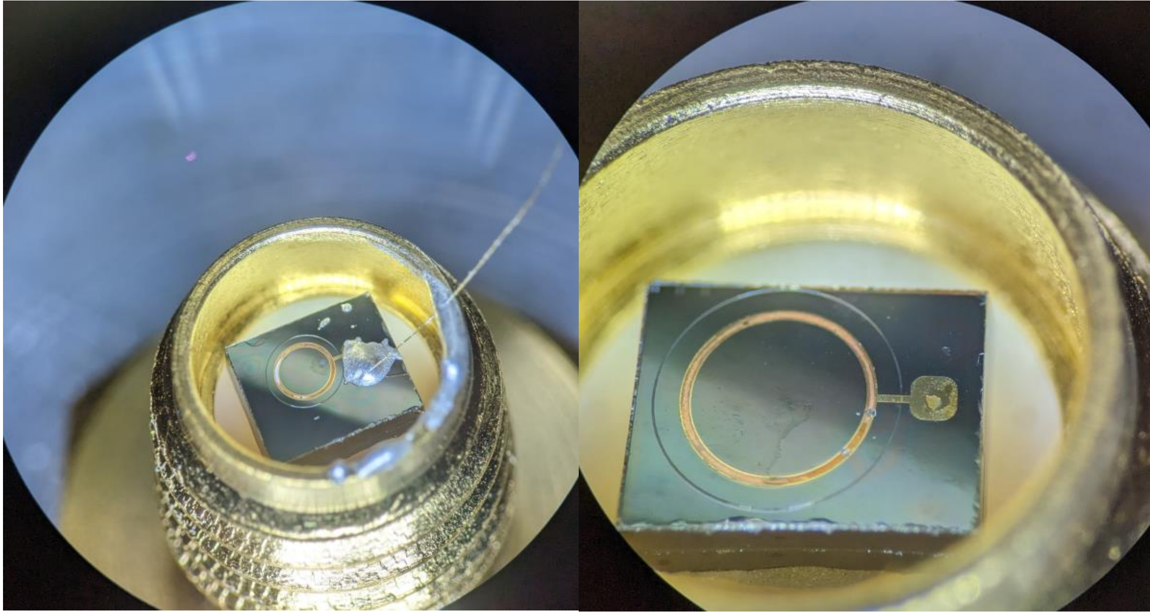
Figure 5.2 – Packaged (left) “medium” sized device with a 1.39mm diameter, and (right) “large” sized device with a 2.015mm diameter.

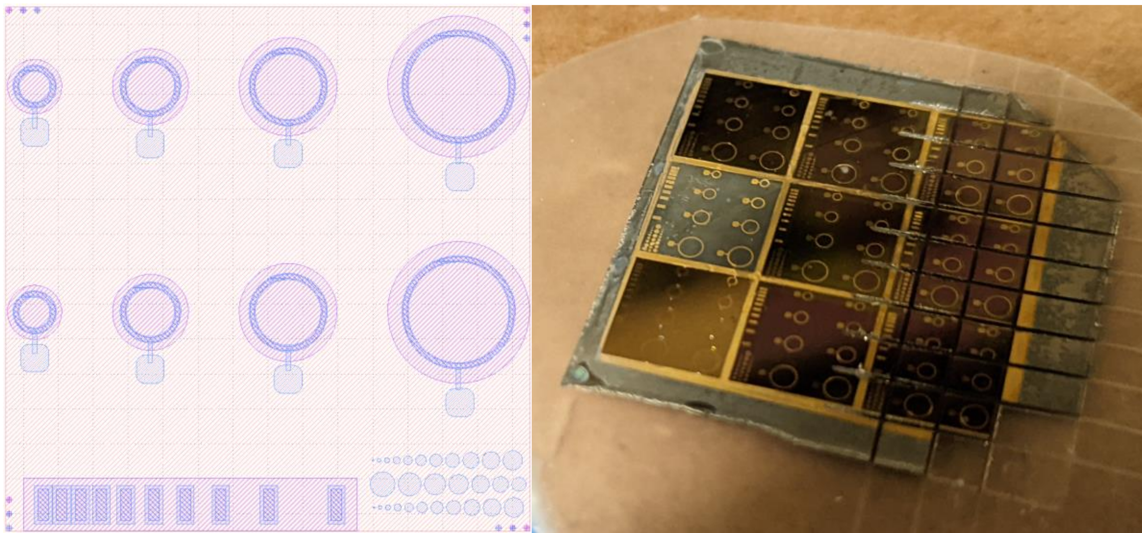
Figure 5.3 – (left) photomask of test devices, and (right) fully fabricated test devices.

tested devices were taken to the Manson lab following testing at ALS and were tested for their quantum efficiency with the Manson source as well.

5.1.2. Experimental Setup

The experimental setup consists of three main components: a tunable x-ray source, a photodiode pointed at the incoming x-ray photons, and a source measure unit (SMU) to bias the photodiode and record the outgoing current. A Manson x-ray source at LLNL was used for low energy x-ray generation and

measurement, 1-7 keV, while the ALS was used for higher energy x-rays, 6-28 keV. The following two sections will provide a brief overview the setup of each source separately, while section following will cover photodiode and SMU setup.

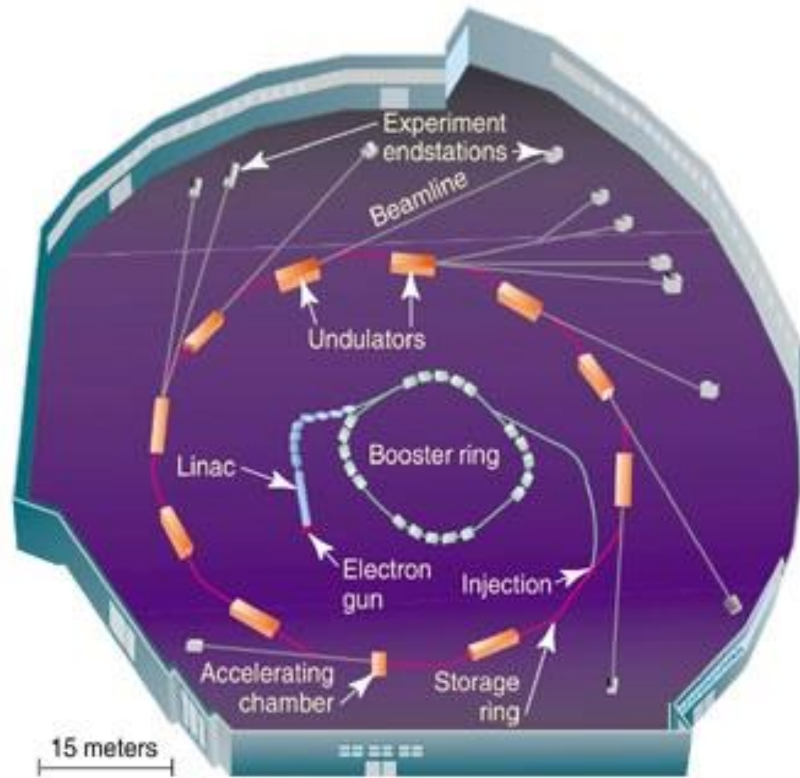

Figure 5.4 – The ALS layout. Image courtesy of LBNL.

5.1.2.1. ALS X-Ray Source

The ALS is a third-generation synchrotron at LBNL, whose general layout can be seen in Fig. 5.4. ALS operates in one of two modes: multi-bunch mode and two-bunch mode. In the primary mode of operation, multi-bunch mode, magneto-bremsstrahlung radiation, more commonly referred to as synchrotronic radiation, is generated when charged particles traveling at relativistic speeds are accelerated tangentially by magnetic fields. This acceleration produces magneto-bremsstrahlung radiation. In the case of ALS, electron pulses are first produced by an electron gun, consisting of thermionic emissions from a heated barium aluminate cathode, pulsed by a 125MHz applied to the gate of the cathode, producing 2.5ns pulses [127]. Electrons exiting the gun are then subjected to three RF bunchers within a LINAC that compress the electron pulses, compressing the pulse to 800ps, then 200ps, then 20ps [127]. The traveling wave accelerator then accelerates the electrons to 50 MeV before injecting the current into the booster ring [127, 128]. The electrons are then accelerated by approximately 150 keV per revolution in the booster ring until an energy of 1.5 GeV is reached [129], at which point they are injected into the 196.8m-circumference storage ring. The injection mechanism accelerates the electrons

with an RF cavity to a final energy of 1.9 GeV, decompressing the pulse to 60ps FWHM in the process. This energy produces an orbital period of 656ns, with a 2ns spacing between each pulse. Once the storage ring has 500mA of current, consisting of 256 to 320 electron pulses, scattering processes gradually reduce the current inside the storage ring. To compensate, electrons are added every 25 to 30 seconds to maintain the operational current in a process called "top off." In two-bunch mode, all operations are the same except for the beam consisting of two 17.5mA bunches. Each pulse has a duration of 60ps, as before, but are now separated by 328ns spacing. Table 5.2 summarizes these operational modes.

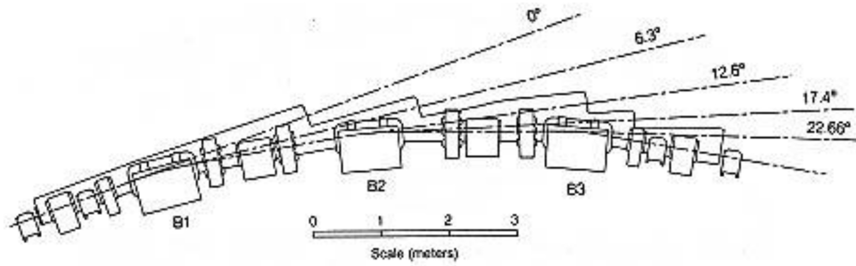

Figure 5.5 – An example of various insertion devices. Devices that do not affect beam directgion (0deg devices) are undulators, devices that bend the beam by 6.3deg are bending magnets exclusively, and the rest are either bending or superbending magnets. Image courtesy of LBNL.

Inside the storage ring, electrons are kept within the roughly circular ring consisting of 12 straight sections and 12 curves by a series of bending magnets. Each straight and curve pair has a designated number and services multiple end stations, with x-rays being generated with a combination of bend magnets, superbend magnets, or superconducting bend magnets, and undulators in a configuration seen in Fig. 5.5. The

Material	Energy (GeV)	Pulse Separation (ns)	Current per Pulse (mA)	Pulse Duration (ps)
Multi-Bunch	1.9	2	2	60
Two-Bunch	1.9	328	17.5	60

Table 5.2 – Operational modes of ALS and their parameters.

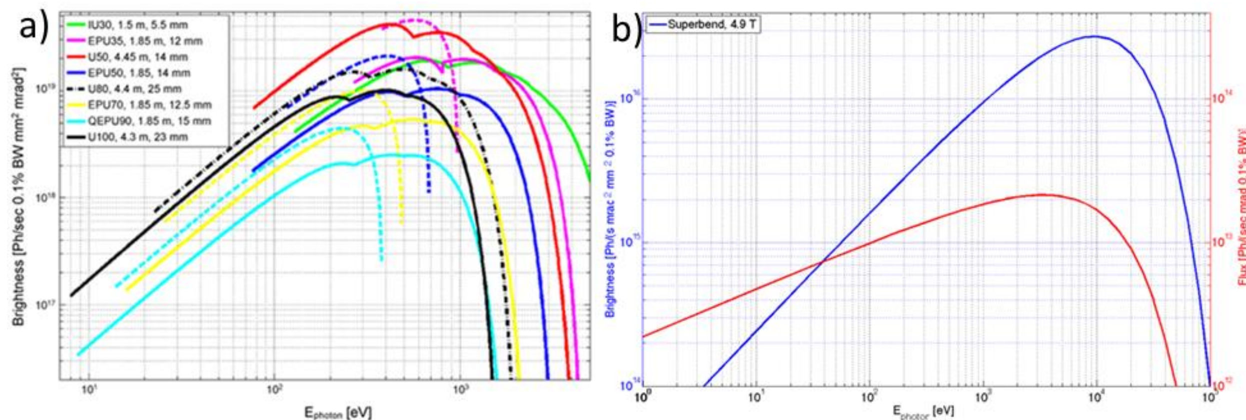

Figure 5.6 – (a) Brightness of various x-ray sources at the ALS, and (b) the brightness and flux of superbend x-ray sources. Images courtesy of LBNL.

type of magnet used depends on the needs of the end-station. Electrons that travel through undulators results in narrow spectral widths of the resultant x-rays due to the periodic nature of the magnetic field, which causes interference of the bremsstrahlung radiation emissions. Bend and superbend magnets accelerate the electrons tangentially to produce a smooth bremsstrahlung radiation curve and must thus pass the resultant x-rays though a monochromator before the destination. The spectra of the various beamlines are shown in Fig. 5.6.

For this dissertation, beamline 12.2.1 was used for testing the external quantum efficiency of germanium, consisting of a superbend magnet with a spectrum that is showing in Fig 5.6b. Once the x-ray beam is generated in the superbend, it is fed into a Kohzu double crystal monochromator, a CAD drawing, and photographs of which can be seen in Figure 5.7. Two Si <111> crystals are used for the monochromating operation. The first crystal is rotated to select the x-ray energy, the second is translated and rotated to optimize the x-ray intensity and direct the beam. The usable range of the monochromator is between 6keV and 28keV x-rays, controllable with LabView control software written specifically for this beamline, with an energy FWHM of 2eV. While the x-ray energy range is insufficient to test the entire x-ray range needed

at NIF, is enough to confirm the internal quantum efficiency curve and mass attenuation coefficients of epitaxial germanium.

Following the monochromator, the x-ray beam is fed into an ion chamber for intensity measurements, and then into a 0.8mm diameter stainless steel collimator. Figure 5.8 shows the shape of the x-ray beam, both collimated and uncollimated, as well as relatively short and long exposures of each. From a purely qualitative analysis of the saturated exposures, the x-ray beam has a shape not conducive to quantum efficiency testing. The beam is not stable with time. The collimation reduces this drastically. Should collimation not be used, measured currents of the silicon and germanium photodiodes would not be comparable. The photon fluence following the collimator is still sufficient to produce significant currents while measuring the quantum efficiency. The output of the collimator is directed at the photodiode under test.

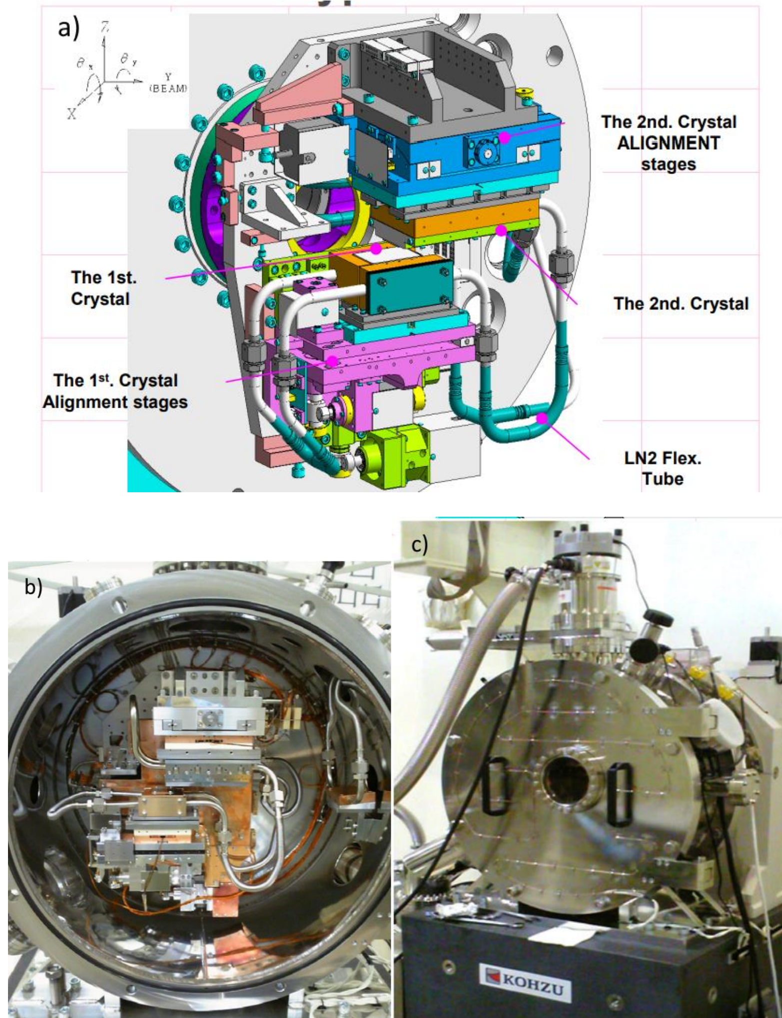

Figure 5.7 – (a) CAD drawing of Kohzu monochromator, (b) photograph of the internals, and (c) photograph of the external. Images courtesy of Kohzu.

Because the small size of the beam, only one photodiode could be tested at a time. X-ray intensity was recorded using the beamline controls to be able to calculate the external quantum efficiency. A schematic

representation of the experimental setup can be seen in Figure 5.9. Figure 5.10 demonstrates experimental setup at the end of the beam.

Once the photodiode is setup, the x-ray beam must be targeted onto the active area of the photodiode to maximize x-ray current. This is achieved with the following hill-climbing algorithm. A course alignment is done visually. Following this the x-direction is swept with roughly 100µm steps and the maximum is selected. The same is done in the y-direction. After this, the Y-axis is tuned more finely by jogging the y-axis motor. Unfortunately, no such motor was installed for the x-axis. Alignment is critical. An improper alignment produces large error in the acquired data.

One the photodiode being tested has been aligned, the x-ray beam was left on, and data was collected from the SMU remotely. To compensate for beam instability, bright current was collected for approximately 240 seconds, followed by approximately 60 seconds of dark current collection. Current integration time was set to 160µs, which was found by trial and error to produce the least amount of uncertainty in the measurements. Photon energy was swept from 6 keV to 28keV in steps of 2keV. Following the change of each energy, the angles of the second Si <111> mirror was swept to maximize the energy output from the monochromator. The ion chamber is filled with air at atmospheric pressure as the response medium, and so response to x-rays is non-linear, as seen in Figure 5.11. A small change in the photon count can produce

a large error in the results. Thus, photon counts must be kept as closely as possible for the same energy across all devices.

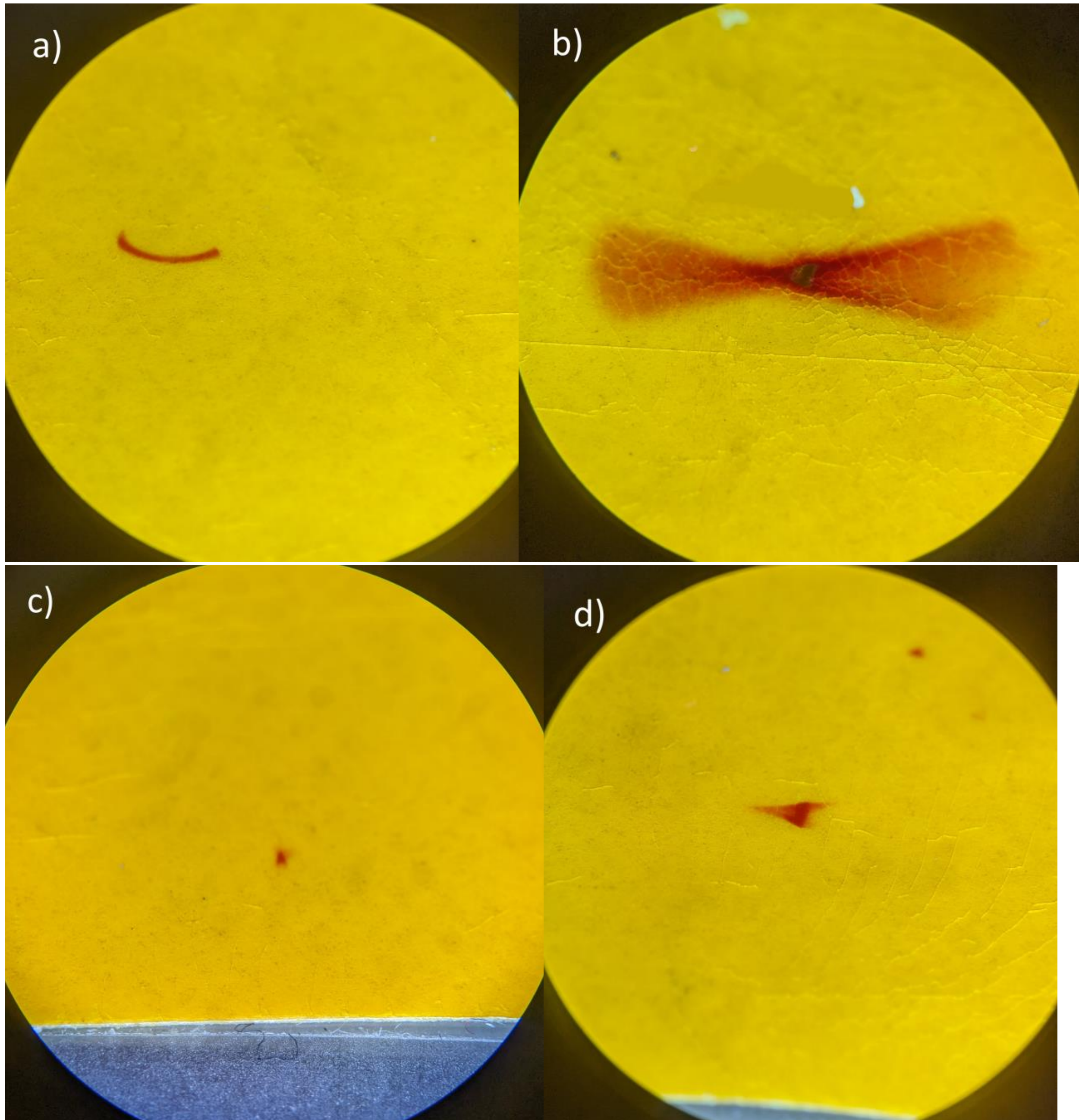

Figure 5.8 – X-ray burn paper exposed to (a) an uncollimated x-ray beam for roughly sixty seconds, (b) an uncollimated x-ray beam for roughly thirty minutes, (c) a collimated beam exposed for roughly sixty seconds, and (d) a collimated beam for roughly thirty minutes. Long tail in (d) is likely due to grazing reflections within the collimator.

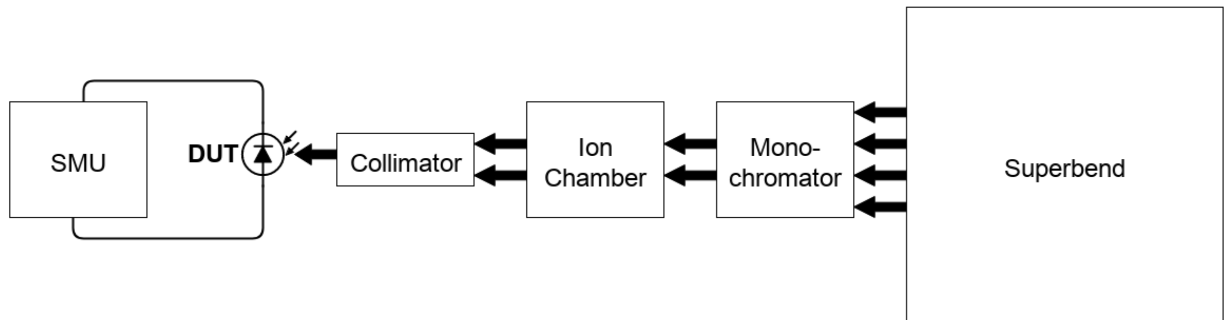

Figure 5.9 – Schematic representation of experimental setup.

Figure 5.10 – Experimental setup of photodiodes at end of beamline.

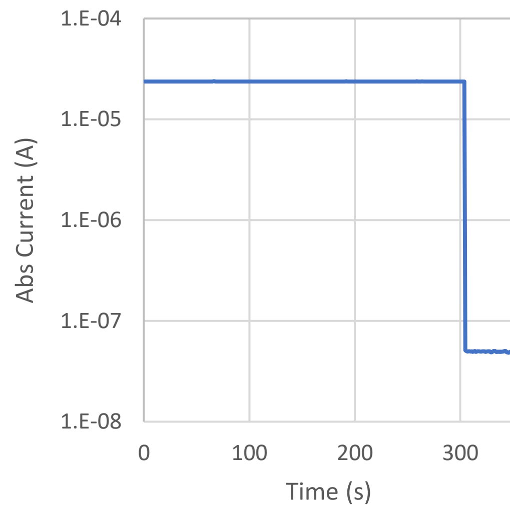

Figure 5.11 – Sample current data as collected by Keithley SMU.

5.1.3. Manson X-Ray Source

The Manson x-ray source is a multi-anode characteristic x-ray source, providing x-rays up to 10keV, depending on the anode selected. X-rays are generated by aiming an electron gun, shooting electrons accelerated by a 10kV voltage source, onto one of six installed anodes: copper, aluminum, zinc, magnesium, platinum, and iron. A general schematic of a Manson source and chamber can be seen in Figure 5.12.

Unlike ALS, where photons are generated by charges accelerated tangentially by a superconducting magnet, the Manson source generates x-rays by accelerating electrons into the anode and inelastically colliding with electrons in the orbitals of the material. If an electron strikes a bound electron, that electron is then ejected

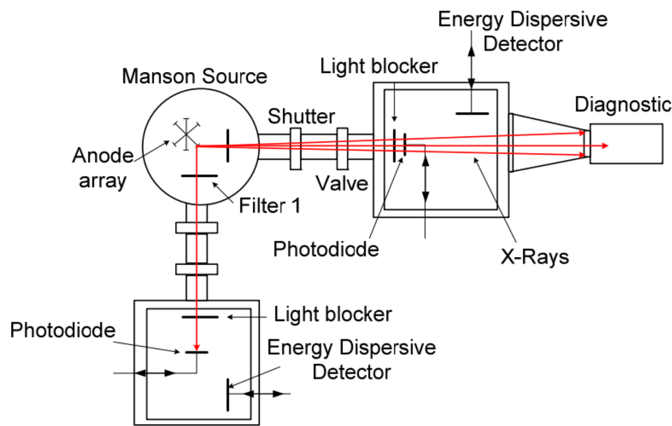

Figure 5.12 – A schematic representation of the Manson source from the rear of the reference box.

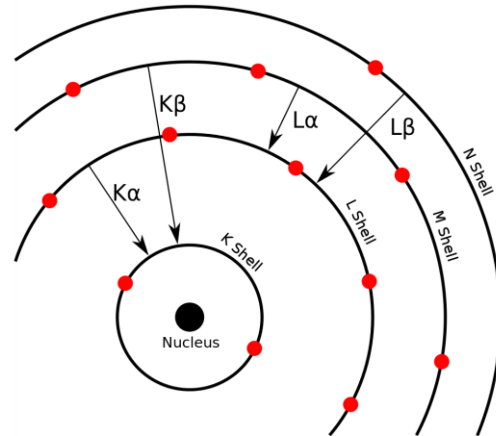

Figure 5.13 – Names of various characteristic x-rays using Siegbahn notation. Reproduced from the public domain [130].

and an electron from a higher orbital takes its place, emitting a photon in the process. The energy of the decaying photon can be calculated very approximately by Equation 5.3, page 2-11 of [135].

$$E = Z^2 \left(\frac{1}{{n_1}^2} - \frac{1}{{n_2}^2}\right) 13.6eV \tag{5.4}$$

Where Z is the atomic number of the element, n_1 is the initial orbital of the decaying electron, and n_2 is the final orbital of the decaying. The equation is only approximate because it does not take electromagnetic shielding of more tightly bound electrons into consideration, unlike more sophisticated models such as the DFT model. One of many electrons can decay into the lower orbital, governed by the time dependent Schrodinger equation, 298-301 of [16]. These can be calculated using time-dependent perturbation theory but derivation of their behavior is not needed for a simple conceptual understanding. The names of these x-rays can be seen in Figure 5.13. In addition to the ones shown there, each transition has further splitting of characteristic x-rays caused by the presence of sub-orbitals within each shell, and are simply denoted by a number. For example, Kα has two possible transitions, and are called Kα1 and Kα2.

Thus, the x-ray generation method of the Manson is significantly different than that of the ALS. Assuming all energy is converted to Kα1 characteristic x-rays, the following fluence can be achieved with the Manson source [131].

$$F = \omega_k \frac{IV_{E-Beam} \cdot 6.24x10^{18}}{E_C} \frac{A_{Shadow}}{A_T} photons/_s \tag{5.4}$$

Where ω_k is the quantum yield of x-rays, a material-specific parameter, I is the electron beam current, V is the accelerating potential of the electron beam, E_C is the critical excitation energy needed to eject a core electron of the material, and $^{A_{Shadow}}/_{A_T}$ is the solid angle of the detector. Figure 5.14 demonstrates the solid angle of a detector. Because characteristic x-rays are radiated with equal power in all directions, the shadow area of a square and circular detector will be different. For a circular detector, A_{Shadow} is given by Equation 5.5a and for a square detector, A_{Shadow} is given by Equation 5.5b.

$$A_{Shadow} = 2\pi\left({r_{Det}}^2 + d^2 - d\sqrt{{r_{Det}}^2 + d^2}\right) \tag{5.5a}$$

$$A_{Shadow} = 4\left(d^2 + \frac{{s_{Det}}^2}{2}\right)\int_0^{\pi/4} \left[tan^{-1}\left(\frac{s_{Det}}{2dcos\ \theta}\right)\right]^2 d\theta \tag{5.5b}$$

Table 5.4 displays expected fluences for all six anodes assuming Equation 5.4 holds. The assumption that all energy is converted to Kα1 x-rays is of course unrealistic, it is merely a practical starting point to understanding x-rays generated by the Manson source and predicting how much current will be produced

by the detector. In reality, additional characteristic x-ray lines from Figure 5.13 can be observed, the most prominent of which is Kα2, as well as bremsstrahlung radiation from electrons colliding with the anode. In theory, these additional x-rays can be used to calculate a range of quantum efficiency values with a single measurement. In practice, the algorithm for this calculation is time-consuming to set up, and is not yet a proven method, rendering these other x-rays undesirable. Thus, a filter is inserted in between the beam path and photodiode to mitigate the presence of these other x-rays made up of the same material as the anode [132]. This mostly eliminates braking radiation and decreases Kα2 more significantly than Kα1, leaving a quasi-monochromatic energy source.

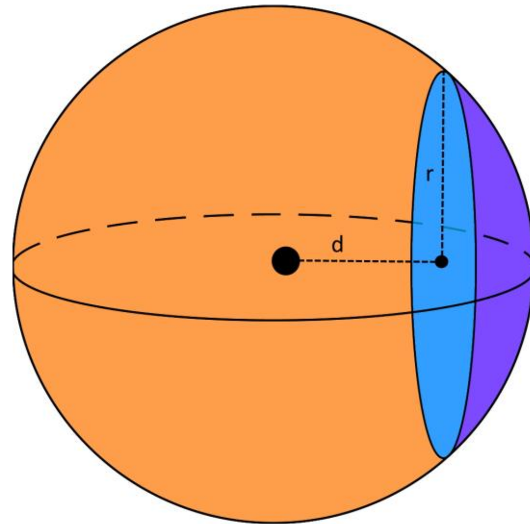

Figure 5.14 – The solid angle of a circular detector, or, given a detector radius r and a distance from the anode d, the proportion of photons captured by the detector to all photons released by the source.

When operating the Manson source, first the desired anode is selected by rotating a bracket. Following this, the electron gun is powered on with a current of 1mA and an accelerating voltage of 10kV. After the x-rays are generated at the anode, they pass through a selectable 25μm thick filter. Following this, the x-rays pass through a beryllium window. Outside the beryllium window two photodiodes were setup side by side, a reference silicon photodiode and the germanium photodiode under test. Because the photodiodes sit

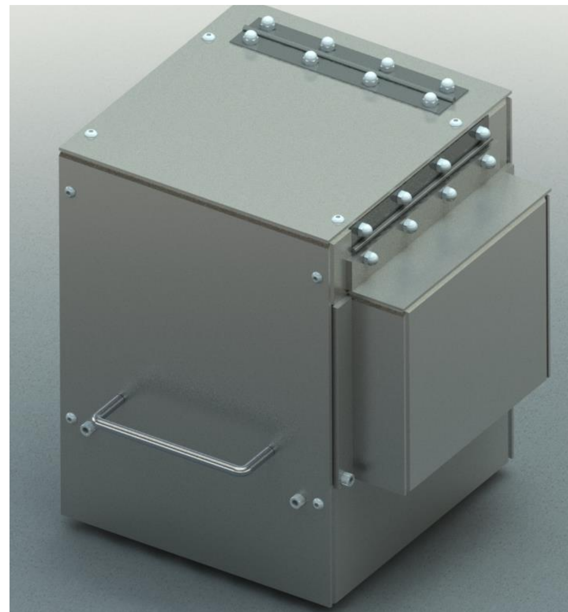

Figure 5.15 – Solidworks render of the safety enclosure fabricated for this experiment.

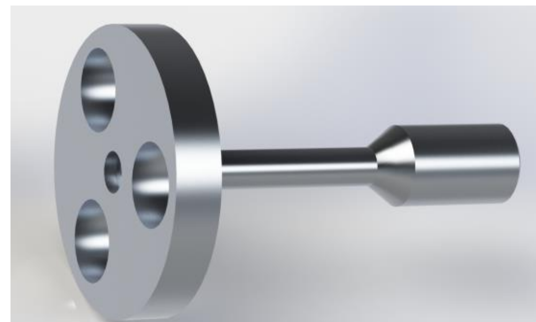

Figure 5.16 – Solidworks render of the SMA diode mount fabricated for this experiment.

outside a beryllium window and in open atmosphere, the user can be exposed to hazardous radiation without the proper safety instrumentation. To mitigate this exposure, a stainless-steel enclosure to house all instrumentation was designed in SolidWorks and fabricated in a machine shop. Machine safety was verified by testing leakage radiation with a Geiger-Muller detector. A SolidWorks render of this chassis can be seen in Figure 5.15. The entire chassis was then grounded to minimize measurement noise.

In addition, a ThorLabs SMA mount and adapter were designed and fabricated using the same tools, as seen in Figure 5.16. Because data acquisition must be synchronized as closely as possible, a LabView program was constructed with sub microsecond instrument synchronization by dedicating a separate thread to communication with each instrument, and threads were synchronized using the Rendezvous data structure. Wireshark was used to verify that software trigger signals were sent to instrumentation no more than a

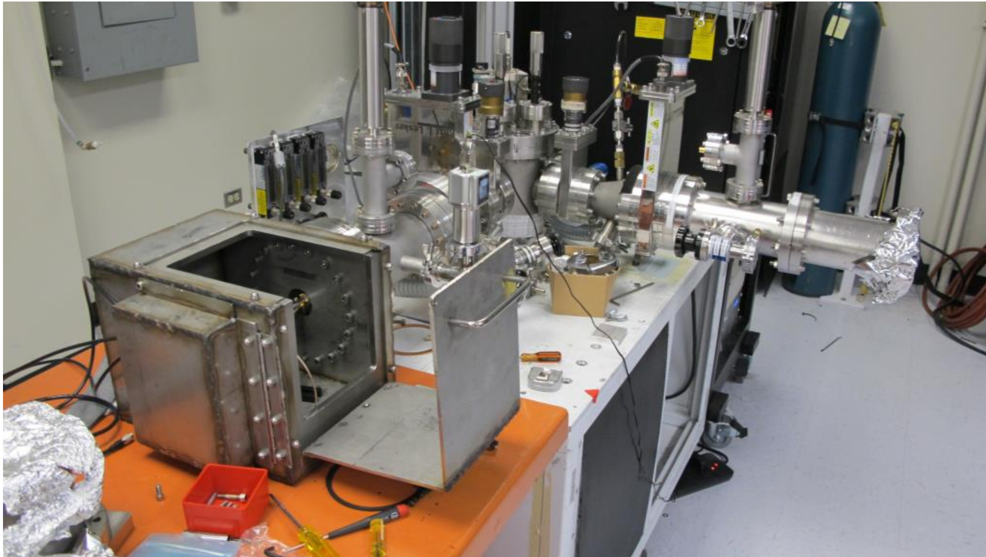

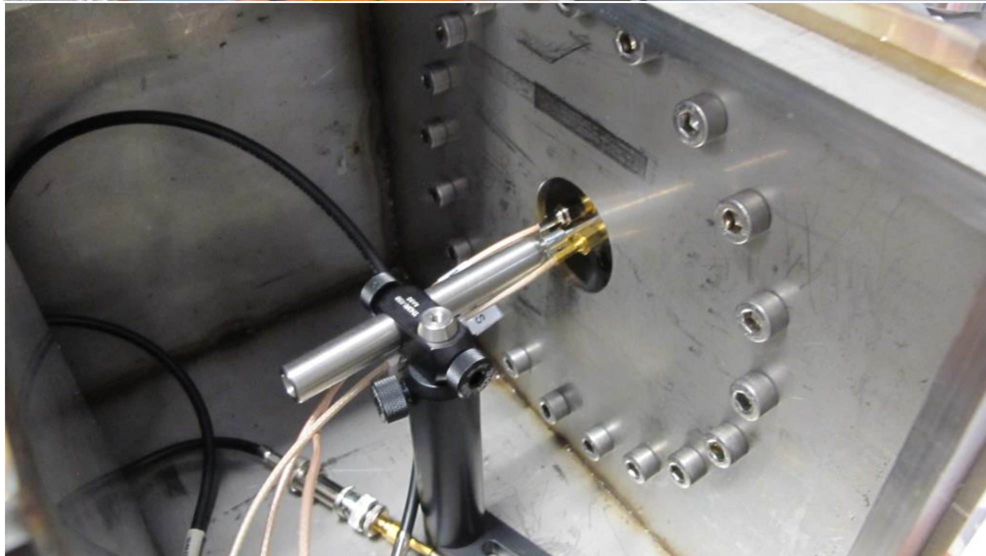

Figure 5.17 – Photos of the experimental setup. (Top) overall view of the experiment with the chassis open, (b) an inside view of the chassis, and (c) a view of the chassis once closed.

photodiode, while a Keithley 6485 electrometer was used to collect current data from the silicon reference photodiode. By trial and error, a 16µs current integration time was found to produce the least amount of uncertainty in the measurements, which is the manufacturer-recommended current integration time. Figure 5.18 shows the schematic display of the final experimental setup, and Figure 5.17 shows photos of the final display.

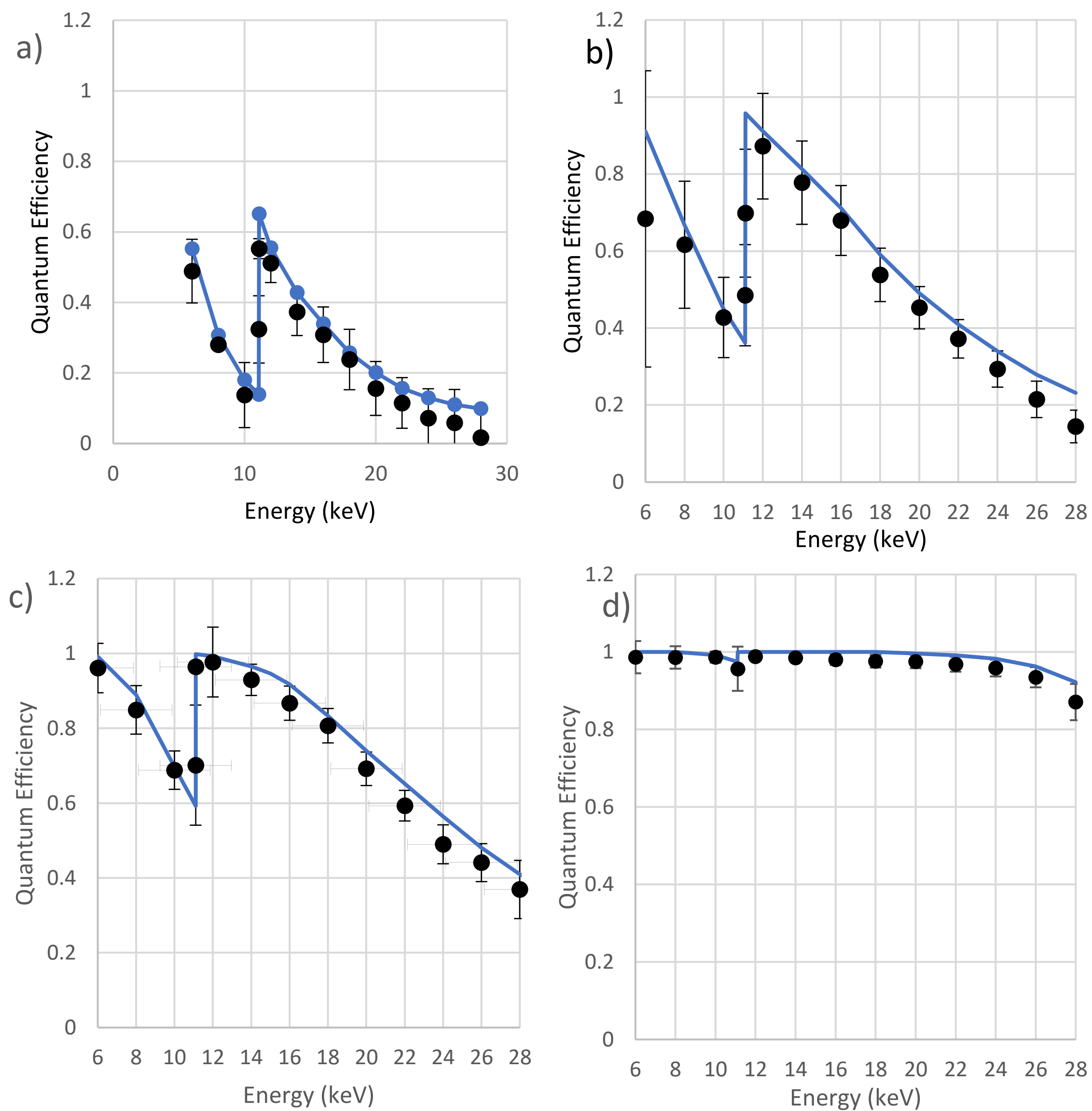

Figure 5.19 – Processed and adjusted germanium quantum efficiency from ALS of (a) 10µm diodes, (b) 30µm diodes, (c) 60µm diodes, and (d) 245µm diodes.

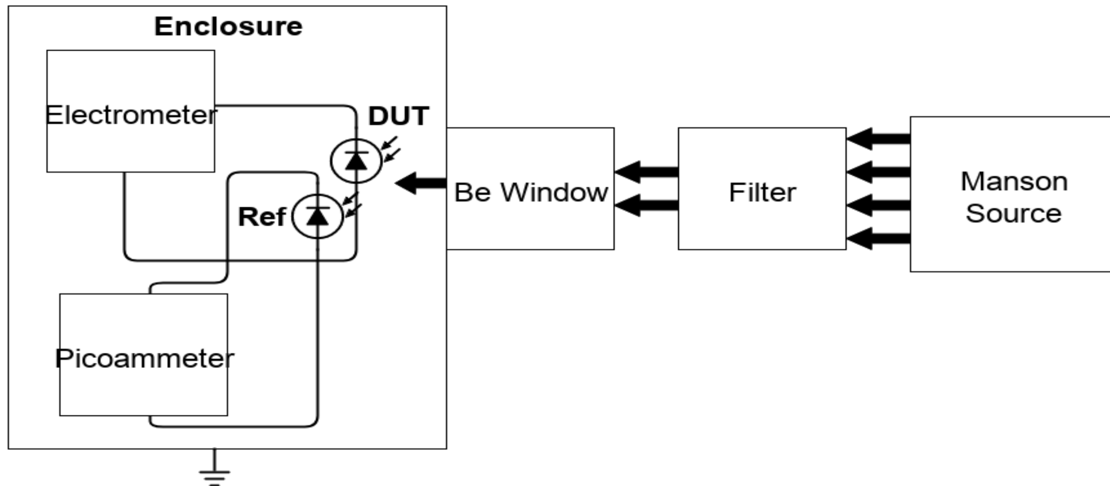

Figure 5.18 – Schematic display of experiment.

5.1.4. Results

Once data is acquired, the calculations begin. Bright and dark currents for each energy collected with each photodiode are individually averaged together. For the ALS source, total power is calculated with Equation 5.5.

$$P = nh\nu \tag{5.5}$$

Where n is the number of photons per second, h is Planck's constant, and ν is photon energy. Because the relationship between photon count and total power is linear, the photon count reported by the ion chamber was used directly in the calculation. Results of measured external quantum efficiencies can Figure 5.19 for the ALS and 5.20 for the Manson. Figure 5.21 displays the reference silicon diode external quantum efficiency.

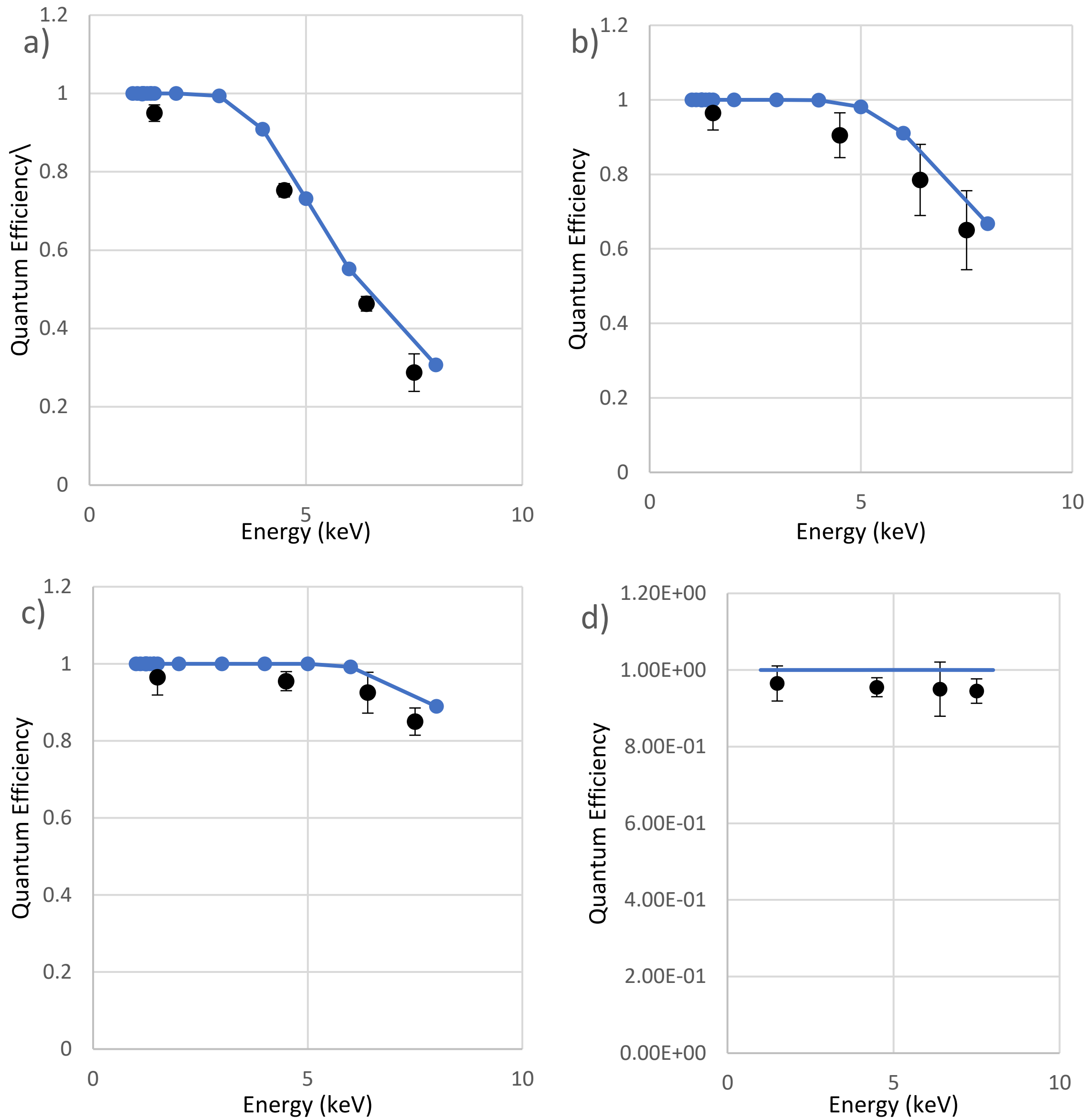

Figure 5.20 – Processed and adjusted germanium quantum efficiency from Manson of (a) 10µm diodes, (b) 30µm diodes, (c) 60µm diodes, and (d) 245µm diodes.

5.2. Temporal Measurements

5.2.1. Methodology

5.2.1.1. General Considerations

Temporal measurements are far easier to perform than quantum efficiency measurements. While they require more hardware and more care in signal detection, the theory is far simpler. Key metrics of temporal

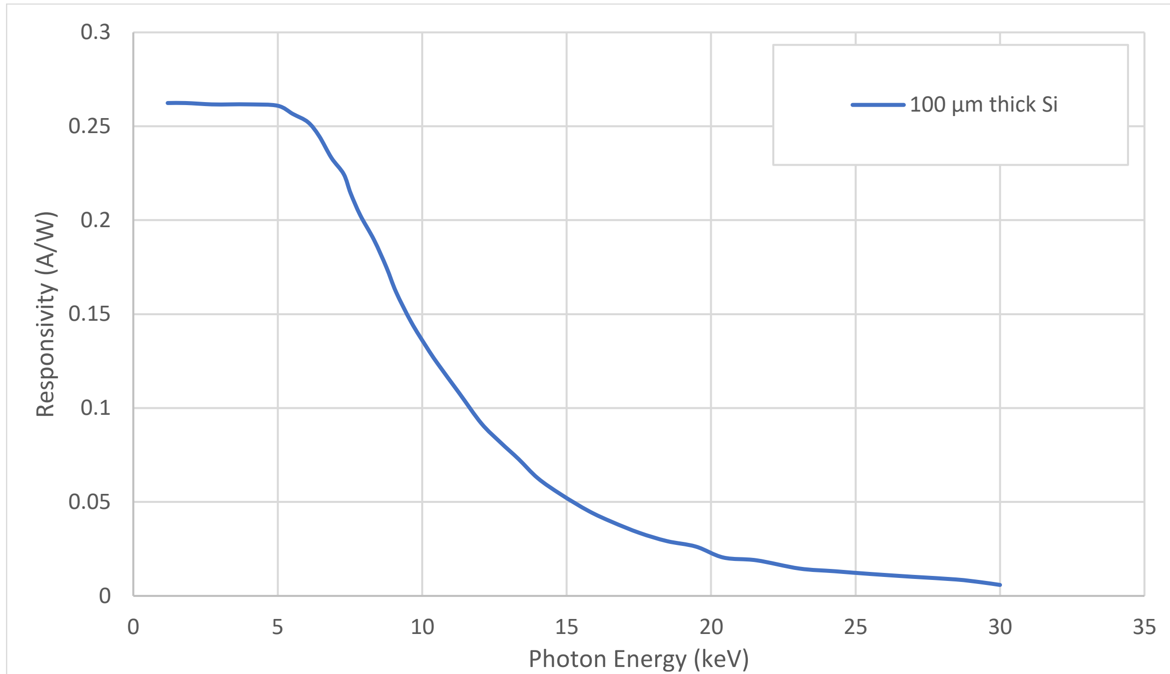

Figure 5.21 – x-ray external quantum efficiency of reference silicon photodiode.

testing are the rise time and the full width at half max (FWHM). The smallest rise time that can be measured is instrument dependent on the bandwidth of the instrument. Equation 5.3 displays this relationship [133].

$$Bt_r = k \tag{5.3}$$

Where B is the bandwidth, t_r is the minimum rise time, and k is a constant dependant on the instrument. In the case of the Tektronix 694C, which was used for this experiment, B=3GHz and k=0.4 [134]. These leads of a minimum oscilloscope rise time of:

$$t_r = \frac{k}{B} = 133ps \tag{5.4}$$

When the measured rise time is much greater than 133ps, we can take the measured value at face value. However, as the rise time approaches the scope, the signal rise time must be calculated in quadrature, as seen in Equation 5.5 [134].

$$t_r{}^2 = t_{signal}{}^2 + t_{scope}{}^2 \tag{5.5}$$

Uncertainty unfortunately grows as the signal rise time approaches the scope rise time, and if the two are equal it is impossible to know the actual rise time of the signal. This is called a bandwidth limited measurement. Unfortunately, the highest bias that could be reached was 50V, the bias tee being the limiting factor. A 200V bias tee was present but broken due to experimenter error. Furthermore, although it was planned to test these photodiodes at multiple energies, the monochromator was broken on the day of the scheduled testing, allowing only for a fixed 17keV to be tested. Temporal and quantum efficiency testing were performed on different days.

5.1.2.1. Devices Tested

Initially, the goal was to test all fabricated photodiodes, but due to experimental error the low noise amplifier used for this testing was broken. Thus only a few 10μm germanium and the reference silicon photodiodes were tested. While it remains unknown whether 30um and 60um photodiodes could be fully evacuated in the target 2ns time, the 10ns devices can be used as a reference to predict their behavior.

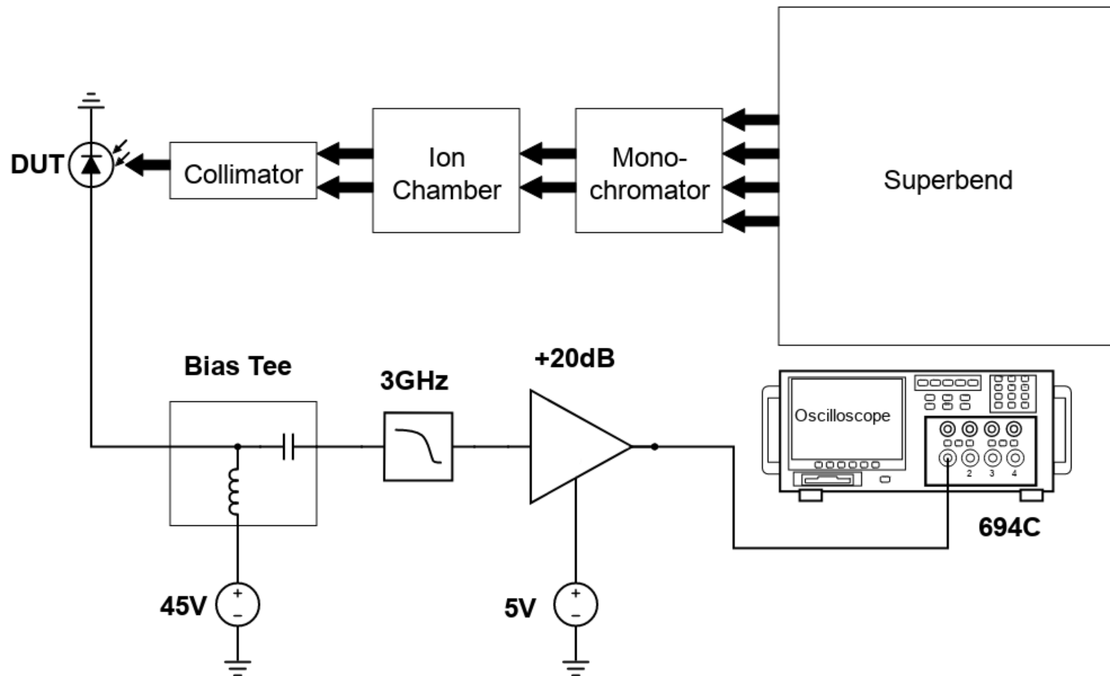

Figure 5.21 – Experimental setup for temporal testing.

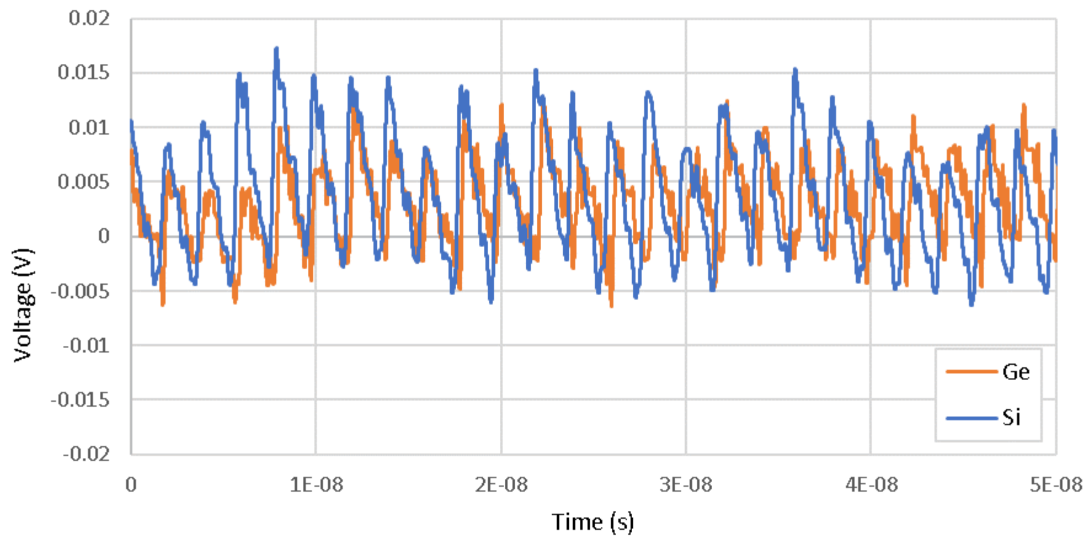

Figure 5.22 – Unprocessed experimental data.

5.2.2. Experimental Setup

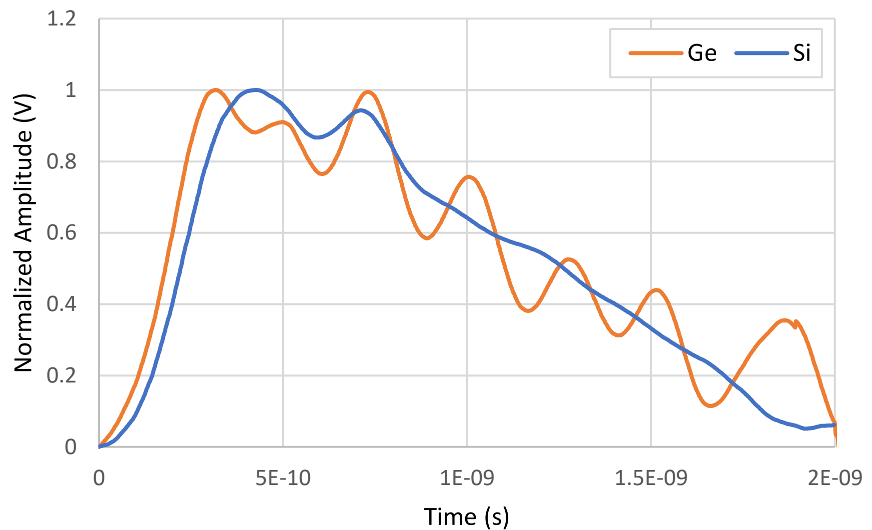

Figure 5.23 – Averaged and normalized oscilloscope traces.

The experimental setup of the ALS source was kept unchanged for this measurement. Beam energy was selected with the monochromator, measured with the ion chamber, and collimated for meaningful comparisons of the output current of the photodiodes. However, the SMU was replaced by a more complicated experimental setup. The photodiode under test was connected to a bias tee, with the inductively coupled port connected to the Keithley SMU as a power supply and the capacitively coupled port connected to a low-pass filter, a +20dB low noise amplifier, and a Tektronix 694C oscilloscope. A

schematic setup of the experiment can be seen in Figure 5.24. Figure 5.25 displays unprocessed sample pulse data.

5.2.3. Results

Figure 5.26 shows a total 5 traces from the various germanium photodiodes and the reference silicon photodiodes averaged and normalized to 1V. As can be seen, average rise time is ~140ps and the silicon rise time is ~180ps. Both photodiodes have a FWHM of ~1.09ns. Because both signals are so close to the minimum rise time of the instrument, a higher bandwidth oscilloscope would be needed for a more accurate measurement. Overall, as can be seen from the traces, the temporal response of the photodiodes is excellent.

Chapter 6 – Conclusions

6.1. Summary and Significance of Work

In this work a foundation was established for the usage of germanium imaging arrays at the National Ignition Facility (NIF) in the Lawrence Livermore National Laboratory (LLNL). Using the Daedalus readout integrated circuit (ROIC) specifications, imaging array requirements were determined to be a 1024x512 pixel array with a pitch of 25µm. Mesa devices were constructed using epitaxial wafers fabricated at the Lawrence Semiconductor Research Laboratory with an intrinsic impurity concentration of 4×10^{15} cm^{-3}, an anode impurity concentration of 5×10^{16} cm^{-3}, and a cathode impurity concentration of 2×10^{18} cm^{-3} and were compared with identical devices simulated in the Silvaco Atlas semiconductor device

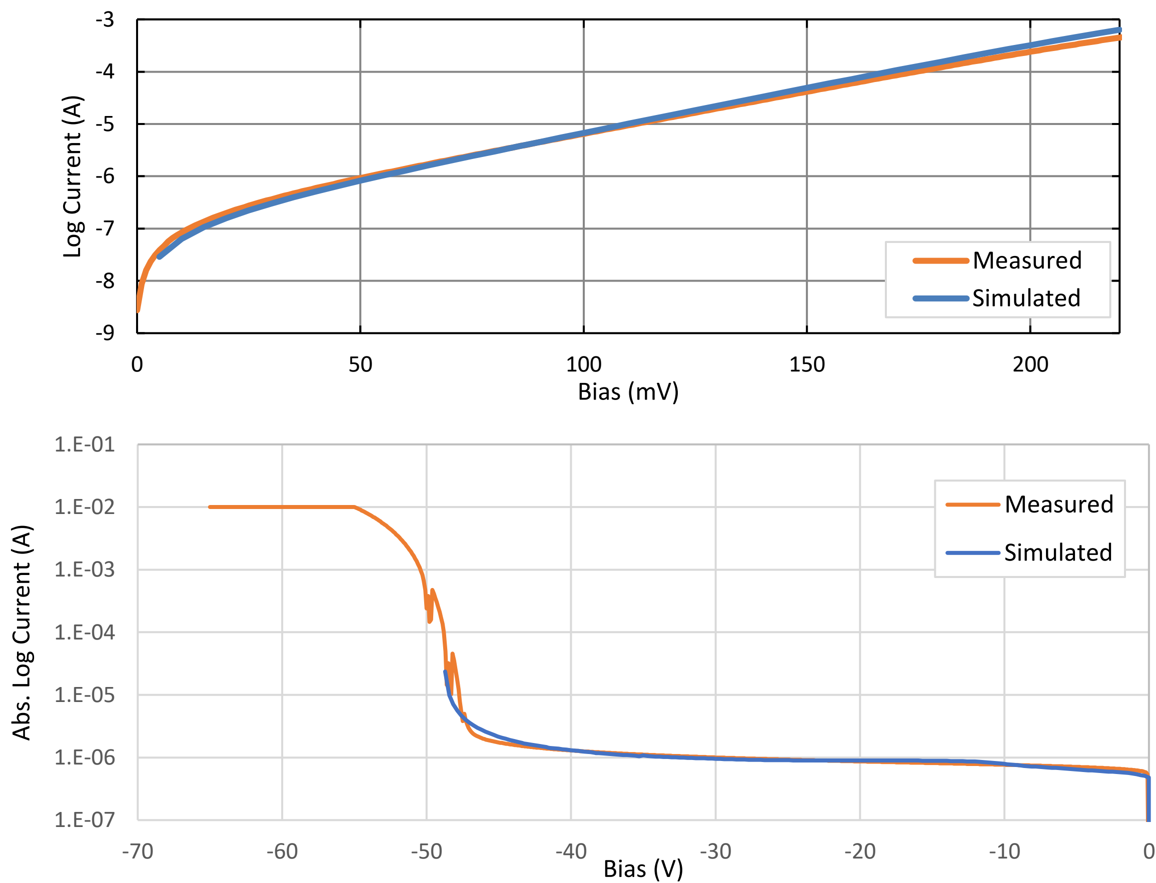

Figure 6.1 – Comparison of (top) IV characteristics and (bottom) reverse IV characteristics of real and simulated germanium diodes.

simulation platform. Current vs voltage characteristics of the devices were shown to have good agreement, as seen in Figure 3.6, reproduced below as Figure 6.1.

Device model was first used to demonstrate the inability of devices made with first generation wafers, consisting of a 60µm-thick intrinsic region impurity concentration of the $2x10^{15}$ cm^{-3}, to be able to reach full depletion before avalanching was triggered. Simulation results predicted full depletion could only be achieved when the impurity concentration is reduced by an order of magnitude. These results were used to guide further epitaxial wafer development, which ultimately achieved an intrinsic region impurity concentration of $1x10^{14}$ cm^{-3}.

Using this platform, it was found that to reach full carrier velocity saturation within germanium photodiodes, a -250V bias would have to be applied to the anode with respect to the cathode. The largest voltage that the Daedalus ROIC could produce, however, is 50V. The device model was then used as a platform for testing photodiode architectures to reduce the depletion bias without sacrificing temporal performance or external quantum efficiency of x-rays in the regions of interest for germanium. The most notable structures are the deep-pit structure, the gaussian planar superjunction (GPSJ) structure, and the deep-pit-GPSJ-hybrid structure. The depletion bias of GPSJ structures was found to strongly be a function

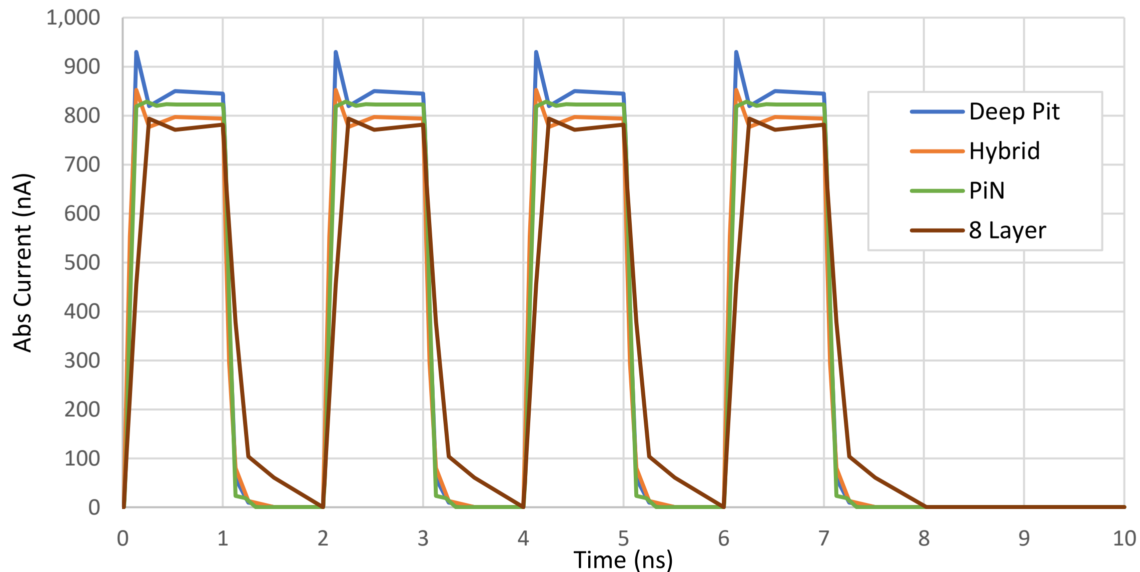

Figure 6.3 – Photodiode response to x-ray pulses of various designs. Hybrid structure capacitance comparable to that of planar PiN and deep pit structgures.

of the number of layers, asymptotically approaching a minimum depletion bias of 10V as the number of layers is increased. However, capacitance of devices was found to increase, slowing temporal response of photodiodes, as seen in Figure 3.26, reproduced in part here as Figure 6.2. Hybrid structures were found to both reduce the capacitive effects of the layers and further reduce the depletion bias of photodiodes. The velocity saturation bias of 4-layer-deep-pit hybrids was found to be 60V, a bias that is closer to the maximum 50V bias of the Daedalus ROIC, without sacrificing the temporal performance of PiN photodiodes, as seen in Figure 3.42, reproduced here as Figure 6.3. These results guide future development of germanium photodiode fabrication, and subsequently high-speed hard x-ray imaging instrumentation at NIF, opening the door for a deeper understanding of plasma instabilities within NIF at peak compression.

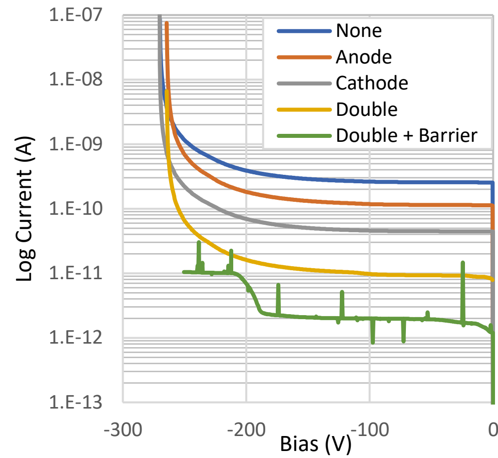

Figure 6.4 – Dark current as a function of bias with various $Ge_{0.9}Si_{0.1}$ heterojunction structures. Having a double heterojunction in combination with a p barrier structure drastically decreases the device dark current.

The device model was simultaneously used to develop a method of reducing photodiode dark current. It was found that barrier structures when used in conjunction with traditional heterojunctions could reduce dark current from 2x10-10 A at a bias of -100V to 2x10-12 A at a bias of -100V, a two order of magnitude reduction. These results can be seen in Figure 3.13, reproduced here as Figure 6.4. These results likewise guide future development of germanium photodiodes, allowing for a longer exposure of the imaging array without saturation of the ROIC imaging capacitance due to pixel dark current.

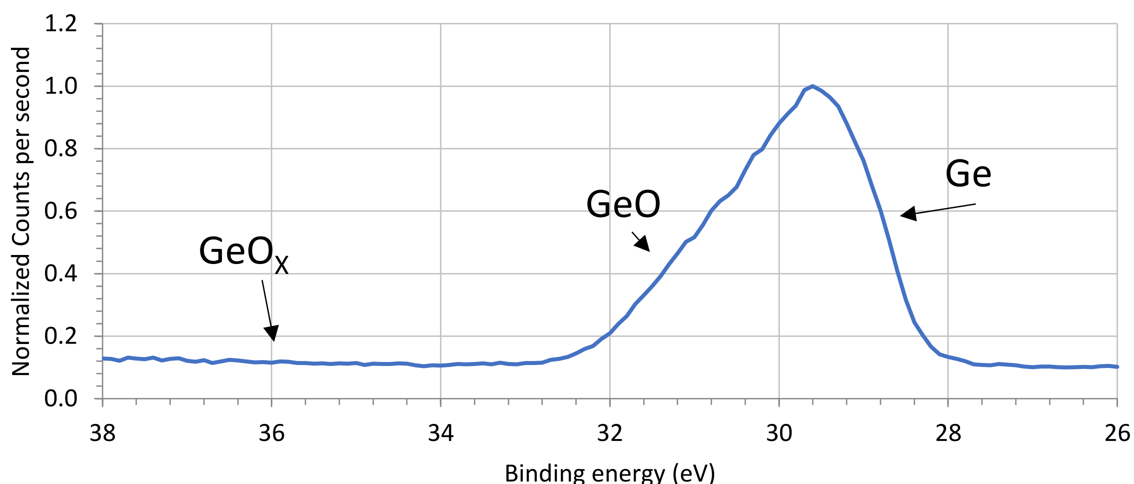

Figure 6.5 – average count of samples that are S terminated. All binding energies unadjusted relative to C footprint. GeOx levels are below the background noise. GeO drops off rapidly.

Simultaneously efforts were made to address the various fabrication challenges of germanium, including the high suboxide presence on the surface, leading to a high trap density, and fermi level pinning phenomenon in the cathodes, leading to rectifying contacts regardless of material selection. Several combinations were tried surface oxides were measured using x-ray photoelectron spectroscopy (XPS). It was found that using a sulfur as a surface termination material produced a nearly non-exist amount of germanium suboxides on the surface. This yields a promising surface passivation method for germanium, potentially decreasing device dark current further and yielding a higher signal to noise ratio. These results can be seen in Figure 4.4, reproduced here as Figure 6.5. Fermi level pinning experiments were found to be not possible with deposition technologies available to the writer of this dissertation.

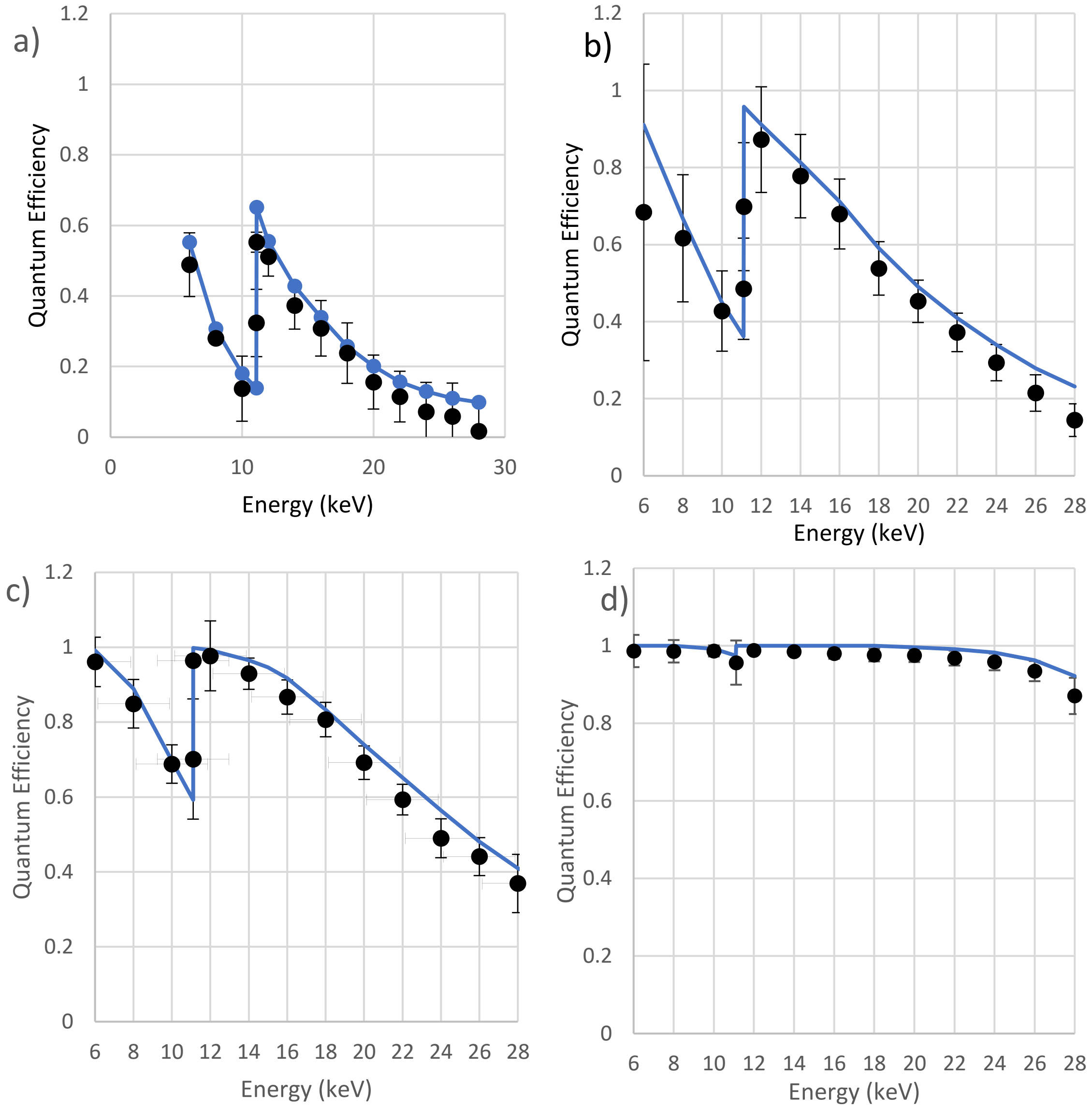

Figure 6.6 – Processed and adjusted germanium quantum efficiency from ALS of (a) 10µm diodes, (b) 30µm diodes, (c) 60µm diodes, and (d) 245µm diodes.

Finally, and possibly most importantly, devices of various epitaxial thickness (10µm, 30µm, 60µm, and 245µm) were fabricated using third generation epitaxial wafers, packaged into SMA connectors, and were taken to the Advanced Light Source (ALS) at the Lawrence Berkeley National Laboratory (LBNL), as well as the Manson Laboratory at LLNL, for x-ray external quantum efficiency and temporal response testing. Internal quantum efficiency was found to be within error bars at both ALS and the Manson Laboratory, providing strong evidence that the internal quantum efficiency, and thus mass-attenuation coefficients, of epitaxial germanium at all tested energy levels are the same as bulk germanium growth through other

methods. The ALS results can be seen in Figure 5.25 and is reproduced here as Figure 6.6. Temporal response with 60ps x-ray pulses arriving in intervals of 2ns showed that all generated charge was evacuated from the germanium photodiodes within the allotted 2ns period, as seen in Figure 5.29 and reproduced here as Figure 6.7. This provides evidence that the final imaging array will perform as intended when bonded to the Daedalus ROIC.

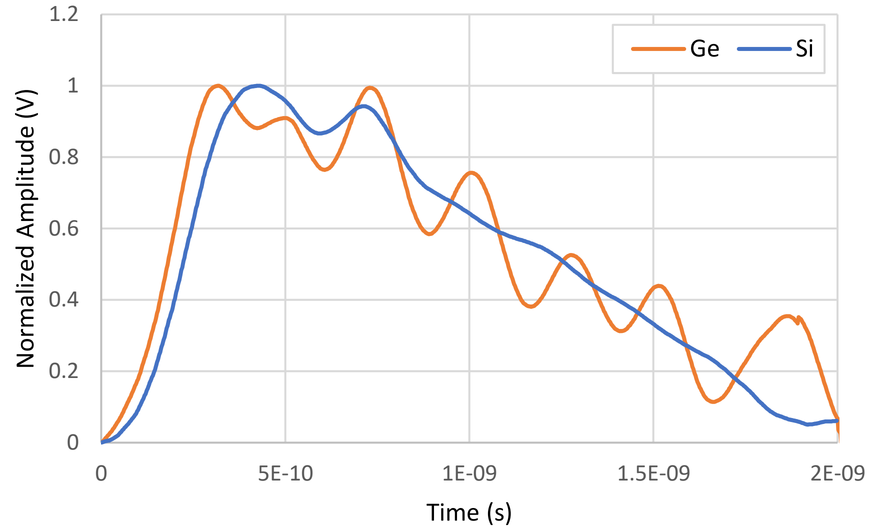

Figure 6.7 – Averaged and normalized oscilloscope traces.

6.2. Future Work

The work in Section 6.1 suggests a natural sequence for future work. Additional epitaxial wafers with the hybrid structure must be grown at LSRL and photodiodes must be fabricated. Individual photodiodes must then be diced and packaged in SMA connectors and likewise be taken to the ALS and the Manson Laboratory for the same quantum efficiency and temporal response testing described in Chapter 5.

Simultaneously, the unresolved fabrication challenges presented in Chapter 4 must be completed, including the testing of the dark current produced by sulfur terminated photodiodes, various metals as cathode materials, anode stability over time, and the degradation of IV characteristics seen after dicing of photodiodes.

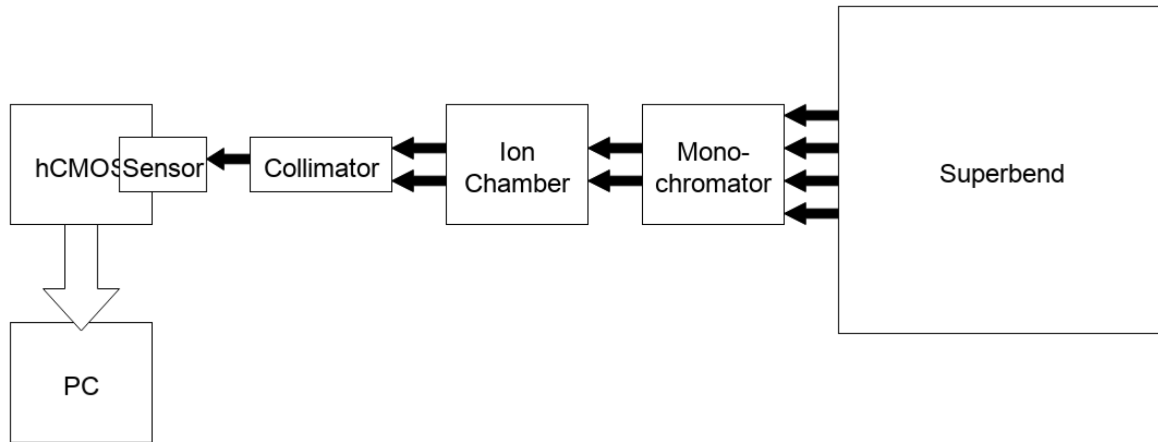

Figure 6.9 – hCMOS camera test setup at the ALS.

Following this, compatibility with the Daedalus ROIC must be tested. To perform this test, a photomask was developed with a full 1024x512 array, as seen in Figure 6.8. Once the process is optimized to produce the arrays, photodiodes must be bonded to the Daedalus ROIC using indium bump bonding. Finally, the fully connected sensor and ROIC package must be connected to an hCMOS camera board developed at Sandia National Laboratories and taken to ALS for the collection of data. The experimental setup needed for this test is shown in Figure 6.9. If all these tests are successful, the imaging array is ready for usage at the NIF for data acquisition.

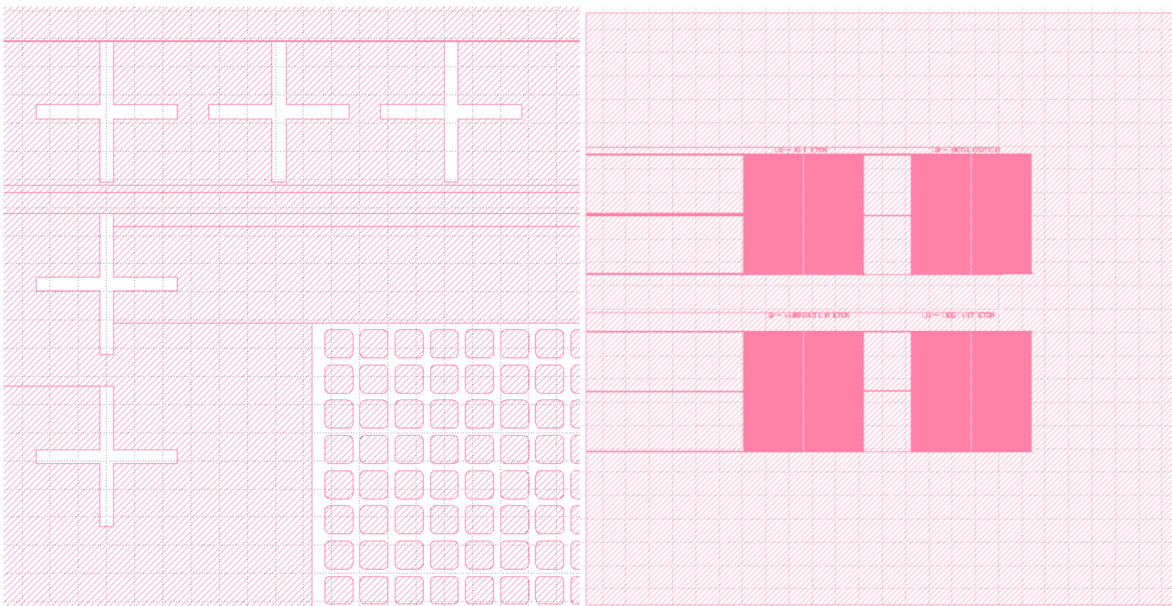
Figure 6.8 – Dual array fabrication mask.

References

1. V. A. Smalyuk et al, “Review of hydrodynamic instability experiments in inertially confined fusion implosions on National Ignition Facility,” 2020 Plasma Phys. Control. Fusion 62 014007
2. J. Badziak, “Laser nuclear fusion: current status, challenges and prospect,” Bulletin of the Polish Academy of Technical Sciences, Vol. 60, No. 4, 2012
3. L. Guo et al, “Uranium hohlraum with an ultrathin uranium–nitride coating layer for low hard x-ray emission and high radiation temperature,” 2015 New J. Phys. 17 113004
4. J.H. Hubbell, S.M. Seltzer, “X-Ray Mass Attenuation Coefficients”. NIST Standard Reference Database 126, 1994.
5. C. E. Hunt, S. Mistyuk, et. al., “Design and characterization of a novel, 1 ns, multi-frame imager for the Ultra-Fast X-ray Imager (UXI) program at Sandia National Laboratories,” SPIE Proceedings Volume 10763, Radiation Detectors in Medicine, Industry, and National Security XIX; 107630M (2018)
6. [136] G. H. Miller, E. I. Moses, C. R. Wuest, “The National Ignition Facility: enabling fusion ignition for the 21st century,” Nuclear Fusion, 44, S228 (2004)
7. L. Claus et al, “Design and characterization of a novel, 1 ns, multi-frame imager for the Ultra-Fast X-ray Imager (UXI) program at Sandia National Laboratories,” Proceedings Volume 10763, Radiation Detectors in Medicine, Industry, and National Security XIX; 107630M (2018)
8. [70] L. Claus et. al., “An overview of the Ultrafast X-ray Imager (UXI) program at Sandia Labs,” Proceedings Volume 9591, Target Diagnostics Physics and Engineering for Inertial Confinement Fusion IV; 95910P (2015)
9. [71] L. Claus et. al., “Design and characterization of an improved, 2 ns, multi-frame imager for the Ultra-Fast X-ray Imager (UXI) program at Sandia National Laboratories,” Proceedings Volume 10390, Target Diagnostics Physics and Engineering for Inertial Confinement Fusion VI; 103900A (2017)
10. [9] C. Jacoboni et al, "Electron drift velocity and diffusivity in germanium," Physical Review B, vol. 24, no. 2, pp. 1014-1026, 1981.
11. [8] J. Stöhr, “NEXAFS Spectroscopy,” Springer Science+Business Media, New York, 1992
12. [10] A. Thakkar, “Quantum Chemistry, 2nd Edition,” Morgan & Claypool Publishers, Kentfield, California, 2017
13. [6] S. Sze, K. K. NG, “Phsyics of Semiconductor Devices, 2nd Edition,” John Wiley and Sons, Hoboken, New Jersey
14. [139] S. Sze, K. K. NG, “Phsyics of Semiconductor Devices, 3nd Edition,” John Wiley and Sons, Hoboken, New Jersey
15. [11] R. Hummel, “Electronic Properties of Materials 4th Edition,” Springer Science+Business Media, New York, 2011
16. [12] D. Griffiths, “Introduction to Quantum Mechanics 2nd Edition,” Prentice Hall, 2017
17. F. Herman, “The Electronic Energy Band Structure of Silicon and Germanium,” Proc. IRE, 43, 1703 (1955)

18. J. S. Blackmore, "Carrier Concentrations and Fermi Levels in Semiconductors," Electron Commun., 29, 13 1 (1952).

19. C. Thurmond, "The Standard Thermodynamic Function of the Formation of Electrons and Holes in Ge, Si, GaAs and GaP,"J. Electrochemical Society, 122, 1133 (1975)

20. J. Hermanson and J. C. Phillips, "Pseudopotential Theory of Exciton and Impurity States," Physical Review, 150, 652 (1966)

21. C. Jacoboni et. al., "A Review of Some Charge Transport Properties of Silicon," Solid-state Electronics, 20,77 (1977)

22. E. Conwell et. al., "Theory of Impurity Scattering in Semiconductors," Physical Review, 77, 388 (1950)

23. E. Paige, "The drift mobility of electrons and holes in germanium at low temperatures," Journal of Physics and Chemistry of Solids, Volume 16, Issues 3–4, 1960

24. E. J. Ryder, "Mobility of Holes and Electrons in High Electric Fields," Physical Review 90, 766, 1953

25. D. Schroder, "Semiconductor Material and Device Characterization 3rd Edition," John Wiley and Sons, Hoboken, New Jersey, 2005

26. R. N. Hall, "Electron-Hole Recombination in Germanium," Phys. Rev., 87,387 (1952)

27. D. T. Stevenson and R. J. Keyes, "Measurement of Carrier Lifetime in Germanium and Silicon," Journal of Applied Physics, 26, 190 (1955)

28. M. Ghosh et. al., "Impurity concentration dependent electrical conduction in germanium crystals at low temperatures," Bulletin of Materials Science volume 42, Article number: 264 (2019)

29. S. Sankarasubramanian, "Study on the Effect of Texture Additives on Silicon Solar Cells and Benchmarking their Electrical Performance," Thesis for Bachelor of Engineering, University of Texas at San Antonio (2012)

30. W. Shockley et. al., "Statistics of the Recombination of Holes and Electrons," Physical Review, 87, 835 (1952)

31. S. Carturan, G. Maggioni, S. Rezvani, R. Gunnella, N. Pinto, M. Gelain and D. Napoli, "Wet chemical treatments of high purity Ge crystals for gamma-ray detectors: Surface structure, passivation capabilities and air stability," MATERIALS CHEMISTRY AND PHYSICS, vol. 161, pp. 116-122 (2015)

32. G. Knoll, "Radiation Detection and Measurement 3rd Edition," John Wiley and Sons, Hoboken, New Jersey, 1999

33. L. Cerrito, "Radiation and Detectors," Springer Nature, Switzerland, 2017

34. Q. Looker et. al., "GaAs x-ray detectors with sub-nanosecond temporal response," Review of Scientific Instrumentation, 90, 113505 (2019)

35. W. Shockley, "The Theory of p-n Junctions in Semiconductors and p-n Junction Transistors," Bell Syst. Tech. J., 28,435 (1949)

36. D. Ye et. al., "A three-terminal ultraviolet photodetector constructed on a barrier-modulated triple-layer architecture," Scientific Reports, volume 6, 26169 (2016)

37. R. Cooper et. al., "Effect of a surface channel on the performance of a P-type Point Contact HPGe detector," Nuclear Instruments and Methods in Physics Research A, vol. 680, pp. 48-55, 2012

38. J. Llacer, “Planar and coaxial high purity germanium radiation detectors,” Nuclear Instruments and Methods Volume 98, Issue 2 (1972)

39. Q. Looker, “Fabrication Process Development for High-Purity Germanium Radiation Detectors with Amorphous Semiconductor Contacts,” Doctoral Dissertation, University of California, Berkeley, 2014

40. Jaeger, R. C., “Introduction to Microelectronic Fabrication: Volume 5 of Modular Series on Solid State Devices 2nd Edition,” Prentice Hall, Upper Saddle River, New Jersey

41. D. L. Greenaway, G. Harbere, “Band Structure of Bismuth Telluride, Bismuth Selenide, and their Respective Allows,” J. Phys. Chem. Solids Pergamon Press 1965. Vol. 26, pp. 1585-1604

42. Shigenobu Shigetomi, Sigeyasu Mori, “Electrical Properties of Bi2Te3,” J. Phys. Soc. Jpn. 11, pp. 915-919 (1956)

43. Z. Ju, Y. Hou, A. Bernard, V. Taufour, D. Yu, S. M. Kauzlarich, "Ambipolar Topological Insulator and High Carrier Mobility in Solution Grown Ultrathin Nanoplates of Sb-Doped Bi2Se3," ACS Appl. Electron. Mater. 2019, 1, 9, 1917–1923, 2019

44. A. M. Conte, O. Pulci, F. Bechstedt, “Electronic and optical properties of topological semimetal Cd3As2,” Sci Rep. 2017; 7: 45500, Published online 2017 Apr 6

45. A. J. Rosenherg, T. C. Harman, “A Noncubic Semiconductor with Unusually High Electron Mobility,” Journal of Applied Physics 30, 1621 (1959)

46. O. F. Shoron, T. Schumann, M. Goyal, D. A. Kealhofer, S. Stemmer, “Field-effect transistors with the three-dimensional Dirac semimetal cadmium arsenide,” Appl. Phys. Lett. 115, 062101 (2019)

47. M. Neupane, S. Y. Xu, R. Sankar, N. Alidoust, G. Bian, C. Liu, I. Belopolski, T. R. Chang, H. T. Jeng, H. Lin, A. Bansil, F. Chou, and M. Z. Hasan, “Observation of a three-dimensional topological Dirac semimetal phase in high-mobility Cd3As2,” Nat. Commun. 5, 3786 (2014)

48. G. Ottaviani, “Charge Carriers Transport Properties in CdTe Measured with Time of Flight Technique,” Rev. Phys. Appl. (Paris) 12, 249-254 (1977)

49. D. Ji, B. Ercan, S. Chowdhury, “Experimental Determination of Velocity-Field Characteristic of Holes in GaN, IEEE Electron Device Letters (Volume: 41, Issue: 1, Jan. 2020)

50. S. Adachi, “Optical Constants of Crystalline and Amorphous Semiconductors,” Springer Science+Business Media, New York

51. Z. Dziuba, K. Szlenk, “Hole mobility in p-type HgTe,” Journal of Physics and Chemistry of Solids, Volume 45, Issue 1, 1984, Pages 97-103

52. J. C. Ugucioni, M. Ferreira, F. Fajardo, M. Mulato, “Growth of mercuric iodide crystals,” Braz. J. Phys. 36 (2a), June 2006

53. Kusmiss, J. H., Iwanczyk, J. S., Barton, J. B., Dabrowski, A. J., Seibt, W., “Mobility and trapping time measurements in HgI2,” Jordan Intern. Elec. And Electron. Engr. Conf., Amman, Jordan, 25 Apr. 1983

54. W. Dietze, E. Doering, et al., “Numerical Data and Functional Relationships in Science and Technology - New Series, 17c,” Springer, 1984

55. R. Quaya, C. Moglestue, V. Palankovski, S. Selberherr, “A temperature dependent model for the saturation velocity in semiconductor materials,” Materials Science in Semiconductor Processing 3 (2000) 149-155

56. B. Monemar, P.P. Paskov, A. Kasic, "Optical properties of InN—the bandgap question," Superlattices and Microstructures, Vol 38, Iss 1, 2005
57. N. Ma, X. Q. Wang, S. T. Liu, G. Chen, J. H. Pan, L. Feng, F. J. Xu, N. Tang, and B. Shen, "Hole mobility in wurtzite InN," Appl. Phys. Lett. 98, 192114 (2011)
58. Stephen K. O'Leary, "Electron transport in wurtzite indium nitride," Journal of Applied Physics 83, 826 (1998)
59. O.P. Gandhi; K. Verma, High-electric-field electron velocity in InSb in transverse and parallel magnetic fields, Proceedings of the IEEE, Vol. 59, Iss. 5, May 1971
60. Y. Guo, J. Robertson, "Band structure, band offsets, substitutional doping, and Schottky barriers of bulk and monolayer InSe," Phys. Rev. Materials 1, 044004 – Published 11 September 2017
61. H. Arora,A. Erbe, "Recent progress in contact, mobility, and encapsulation engineering of InSe and GaSe," InfoMat, Vol. 3, Iss. 6, June 2021, 662-693
62. R. Ahuja, H. Arwin, Ferreira da Silva, et. al., "Electronic and optical properties of lead iodide," Journal of Applied Physics, Volume 92, Number 12, 2002
63. B. Maynard, Q. Long, E. A. Schiff, et. al., "Electron and hole drift mobility measurements on methylammonium lead iodide perovskite solar cells," Appl. Phys. Lett. 108, 173505 (2016)
64. B. Cho, W. K. Peters, R. J. Hill, T. L. Courtney, D. M. Jonas, "Bulklike Hot Carrier Dynamics in Lead Sulfide Quantum Dots," Nano Lett. 2010, 10, 7, 2498–2505, 2010
65. R. S. Allgaier, W. W. Scanlon, "Mobility of Electrons and Holes in PbS, PbSe, and PbTe between Room Temperature and 4.2°K," Phys. Rev. 111, 1029, August 1958
66. Adachi S. (1999) Zinc Telluride (ZnTe). In: Optical Constants of Crystalline and Amorphous Semiconductors. Springer, Boston, MA.
67. M. Aven, "Mobility of Holes and Interaction between Acceptor Defects in ZnTe," Journal of Applied Physics 38, 4421 (1967), June 2004
68. S. Khedim, N. Sari, B. Benyoucef and B. Bouazza, "Electronic Transport Study of ZnTe and ZnSe," Materials Sciences and Applications, Vol. 2 No. 5, 2011, pp. 364-369
69. A Rogalski, "HgCdTe infrared detector material: history, status and outlook," Institute of Applied Physics, Military University of Technology, August 2005
70. J. Taborda et. al., "Coatings and Thin-Film Technologies," Open access peer-reviewed online textbook
71. S. Lee et. al., "Direct Thermal Growth of Large Scale Cl-doped CdTe Film for Low Voltage High Resolution X-ray Image Sensor," Scientific Reports volume 8, Article number: 14810 (2018)
72. C. Fabjan et. al., "Particle Physics Reference Library, Volume 2," Springer Nature, Switzerland, 2020
73. Hamamatsu Corp., "Opto-semiconductor Handbook," online manual
74. C. Eijk, "Fast lanthanide-doped inorganic scintillators," Proceedings Volume 2706, Tenth Feofilov Symposium on Spectroscopy of Crystals Activated by Rare-Earth and Transitional-Metal Ions; (1996)
75. C. Hu et. al., "BaF2:Y and ZnO:Ga crystal scintillators for GHz hard X-ray imaging," Nuclear Instruments and Methods in Physics Research Section A: Accelerators, Spectrometers, Detectors and Associated Equipment, Vol. 950, January 2020

76. R. Binder et. al., “Thin Films of Barium Flouride Scintillator Deposited by Chemical Vapor Deposition,” Nuclear Instruments and Methods in Physics Research, A289, 261-264 (1990)

77. K. Iwahori et. al., "Optical properties of fluoride thin films deposited by RF magnetron sputtering," Appl. Opt. 45, 4598-4602 (2006)

78. S. Sokovnin et. al., “Physical properties of fluorides barium and calcium nanopowders produced by the pulsed electron beam evaporation method,” J. Phys.: Conf. Ser. 1115, 032092, 2018

79. V. Bora, “Photon Statistics in Scintillator Crystals,” Doctoral Dissertation, University of Arizona, 2015

80. M. L'Annunziata, “Handbook of radioactivity analysis 2nd Edition,” Academic Press, San Diego, 2003

81. M. Keidar et. al., “Plasma Engineering 2nd Edition,” O’Reilly Academic Press, 2013

82. S. Glenn et. al., “Advanced gated x-ray imagers for experiments at the National Ignition Facility,” Proceedings Volume 8144, Penetrating Radiation Systems and Applications XII; 814409 (2011)

83. A. Gilmour, “Klystrons, Traveling Wave Tubes, Magnetrons, Crossed-Field Amplifiers, and Gyrotrons,” Artech House, Boston, 2011

84. G. Hellings et. al., “Electrical TCAD Simulations and Modeling in Germanium,” Springer Dordrecht, Heidelberg, New York, 2013

85. V. Fistul et. al., “Mobility of electrons in germanium strongly doped with arsenic,” Sov. Phys., Solid State 4(4), 784–785 (1962)

86. O. Golikova et. al., “Hole mobility of germanium as a function of concentration and temperature,” Sov. Phys., Solid State 3(10), 2259–2265 (1962)

87. G. Masetti et. al., “Modeling of carrier mobility against carrier concentration in arsenic-, phosphorus-, and boron-doped silicon,” IEEE Trans. Electron Devices 30(7), 764–769 (1983)

88. D. Caughey et. al., “Carrier mobilities in silicon empirically related to doping and field,” Proc. IEEE 55(12), 2192–2193 (1967)

89. J.G. Fossum et. al., “A physical model for the dependence of carrier lifetime on doping density in nondegenerate silicon,” Solid-State Electron. 25, 741–747 (1982)

90. A. Schenk, “Rigorous theory and simplified model of the band-to-band tunneling in silicon,” Solid-State Electron. 36(1), 19–34 (1993)

91. G.A.M. Hurkx et. al., “A new recombination model for device simulation including tunneling,” IEEE Trans. Electron Devices 39(2), 331–338 (1992)

92. A. Dimoulas et. al., “Fermi-level pinning and charge neutrality level in germanium,” Appl. Phys. Lett. 89, 252110 (2006)

93. K. Kasahara et. al., “Mechanism of Fermi level pinning at metal/germanium interfaces,” Phys. Rev. B 84, 205301 (2011)

94. X. Lou et. al., “Understanding of Fermi level pinning at metal/germanium interface based on semiconductor structure,” Appl. Phys. Express 13 031003 (2020)

95. D. Wu et. al., “Mid-wavelength infrared high operating temperature pBn photodetectors based on type-II InAs/InAsSb superlattice,” AIP Advances 10, 025018 (2020)

96. R. Williams et. al., “The Trench Power MOSFET: Part I—History, Technology, and Prospects,” IEEE Transactions on Electron Devices, Volume: 64, Issue: 3, (2017)

97. B. Zhang et. al., “Concept and design of super junction devices,” Journal of Semiconductors, Volume 39, Number 2 (2018)

98. F. Undrea et. al., “Superjunction Power Devices, History, Development, and Future Prospects,” IEEE Transactions on Electron Devices, Volume: 64, Issue: 3 (2017)

99. Kumar, Ankit. “Ohmic Contacts to Homoepitaxially Grown p-Type and n-Type Germanium.” University of California, Davis, 2020. Print.

100. Garafalo, Anne. “The Cleaning and Passivation of Germanium X-Ray Photodiodes.” University of California, Davis, 2020. Print.

101. S. W. Glunz, F. Feldmann, "SiO2 surface passivation layers – a key technology for silicon solar cells," Solar Energy Materials and Solar Cells, Volume 185 (2018)

102. S. Carturan, G. Maggioni, S. Rezvani, R. Gunnella, N. Pinto, M. Gelain and D. Napoli, "Wet chemical treatments of high purity Ge crystals for gamma-ray detectors: Surface structure, passivation capabilities and air stability," MATERIALS CHEMISTRY AND PHYSICS, vol. 161, pp. 116-122 (2015)

103. M. M. Frank, S. J. Koester, M. Copel, J. A. Ott, V. K. Paruchuri, H. Shang and R. Loesing, "Hafnium oxide gate dielectrics on sulfur-passivated germanium," Applied Physics Letters, vol. 89, no. 11 (2006)

104. Berghuis, W.J.H., Melskens, J., Macco, B. et al. Surface passivation of germanium by atomic layer deposited Al2O3 nanolayers. Journal of Materials Research 36, 571–581 (2021)

105. Wilhelmus J. H. (Willem-Jan) Berghuis, Jimmy Melskens, Bart Macco, Roel J. Theeuwes, Lachlan E. Black, Marcel A. Verheijen, Wilhelmus M. M. (Erwin) Kessels, “Excellent surface passivation of germanium by a-Si:H/Al2O3 stacks,” Journal of Applied Physics, 130, 13 (2021)

106. J. Isometsä et. al., “Surface Passivation of Germanium with ALD Al2O3: Impact of Composition and Crystallinity of GeOx Interlayer,” Crystals, 13(4), 667 (2023)

107. N.E. Posthuma, G. Flamand, W. Geens, J. Poortmans, “Surface passivation for germanium photovoltaic cells,” Solar Energy Materials and Solar Cells, Volume 88, Issue 1 (2005)

108. Liu, H., Pasanen, T.P., Fung, T.H., Isometsä, J., Leiviskä, O., Vähänissi, V. and Savin, H., “Comparison of SiNx-Based Surface Passivation Between Germanium and Silicon,” Phys. Status Solidi A, 220: 2200690 (2023)

109. L. P. Etcheverry et. al, “Combining GeO2 passivation strategies aiming at dielectric layers with superior properties on germanium substrates,” J. Mater. Chem. C, 7, 8465 (2019)

110. M. Nowakowski, J. Bandaru, L. Bell and S. Nikzad, "Preparation of Ge (100) Substrates for High-Quality Epitaxial Growth of Group IV Materials," Self-Organized Processes in Semiconductor Heteroepitaxy, vol. 794, pp. 71-76 (2004)

111. P. Ponath, A. B. Posadas and A. A. Demkov, "Ge(011) Surface Cleaning Methods for Device Integration," Appl. Phys. Rev. , vol. 4, no. 2, pp. 324-328 (2017)

112. M. M. Frank et. al., “Hafnium oxide gate dielectrics on sulfur-passivated germanium,” Appl. Phys. Lett. 89, 112905 (2006)

113. W. P. Bai et. al., “Si interlayer passivation on germanium MOS capacitors with high-/spl kappa/ dielectric and metal gate,” IEEE Electron Device Letters, Volume 26, Issue 6 (2005)

114. D. R. Baer et. al., “Practical Guides for X-Ray Photoelectron Spectroscopy (XPS): First Steps in planning, conducting and reporting XPS measurements,” J Vac Sci Technol A., 37 (2019)

115. I. Park “Improvement of Fermi-Level Pinning and Contact Resistivity in Ti/Ge Contact Using Carbon Implantation,” Micromachines, 13(1), 108, (2022)

116. A. L. Stepanov et. al., “Porous germanium formed by low energy high dose Ag+-ion implantation,” Vacuum, Volume 152, Pages 200-204 (2018)

117. Y. Zhou, M. Ogawa, X. Han, K. L. Wang, “Alleviation of Fermi-level pinning effect on metal/germanium interface by insertion of an ultrathin aluminum oxide,” Applied Physics Letters, 93(20), 202105 (2008)

118. M. Iyota et. al., “Ohmic contact formation on n-type Ge by direct deposition of TiN,” Applied Physics Letters, 98(19), 192108 (2011)

119. Y. Zhang et. al., “Reduced Contact Resistance Between Metal and n-Ge by Insertion of ZnO with Argon Plasma Treatment,” Nanoscale Research Letters, 13(1) (2018)

120. S. Dev, N. Remesh, Y. Rawal, P. P. Manik, B. Wood, S. Lodha, “Low resistivity contact on n-type Ge using low work-function Yb with a thin TiO2 interfacial layer,” Applied Physics Letters, 108(10), 103507 (2016)

121. G. Borghs et. al., “Ohmic contact formation on n-type Ge,” Applied Physics Letters, 92(2), 022106 (2008)

122. S. Pitale, M. Ghosh, S.G. Singh, H. Manasawala, G.D. Patra, S. Sen, “Characteristics of Al/Ge Schottkey and ohmic contacts at low temperatures,” Materials Science in Semiconductor Processing, Vol 130, 105820 (2021)

123. Yit-Ping Kok and A. Abdul Aziz, "Effect of germanium cap layer on indium ohmic contacts for n-type GaAs," 2004 IEEE International Conference on Semiconductor Electronics, Kuala Lumpur, Malaysia, 2004

124. L. Lewis, D. P. Casey, A. V. Jeyaseelan, J. F. Rohan, P. P. Maaskant, “Electroless nickel/gold Ohmic contacts to p-type GaN,” Appl. Phys. Lett. 11 February 2008; 92 (6): 062113.

125. P. L. Menezes, S. P. Ingole, M. Nosonovsky, S. V. Kailas, M. R. Lovell, “Tribology for Scientists and Engineers,” Springer Science+Business Media, New York (2013)

126. P. Jacob, “Unusual defects, generated by wafer sawing: An update, including pick&place processing,” Microelectronics Reliability, 2015

127. C. C. Low, B. Taylor, H. Lancaster, “Low Power RF System for the ALS Linac,” IEEE Particle Accelerator Conference, San Francisco, CA, USA, 1991, pp. 807-809 vol. 2

128. J. Bengtsson, W. Leemans, T. Byrne, “Emittance measurement and modeling of the ALS 50MeV linac to booster line,” Proceedings of International Conference on Particle Accelerators, Washington, DC, USA, 1993, pp. 567-569 vol. 1

129. C. H. Kim, “Modeling of the ALS Linac,” OSTI Web Repository (1996)

130. “Characteristic X-ray,” Wikipedia Foundation (2023); https://en.wikipedia.org/wiki/Characteristic_X-ray

131. . Hu, C.Y. Zhang, “Simple and Accurate Quantification of Quantum Yield at the Single-Molecule/Particle Level,” Anal. Chem. 2013, 85, 4, 2000–2004 (2013)

132. M. J. Haugh, M. B. Schneider, “Flat Field Anomalies In An X-Ray CCD Camera Measured Using A Manson X-Ray Source,” OSTI Web Repository (2008)

133. “Typical Oscilloscope Circuitry,” Tektronix, 1967

134. “TDS694C User Manual,” Tektronix, 1999

135. B. C. Reed, “The Bohr Atom,” IOP Publishing, 2020